The Dissertation Committee for Kevin Andrew Bokelmann
certifies that this is the approved version of the following dissertation:

Exploration and Optimization of Low-Energy Capture Options at Jovian Moons

Committee:

Ryan P. Russell, Supervisor

Srinivas V. Bettadpur

Maruthi R. Akella

Brandon Jones

Anastassios E. Petropoulos

Exploration and Optimization of Low-Energy Capture Options at Jovian Moons

by

Kevin Andrew Bokelmann

DISSERTATION

Presented to the Faculty of the Graduate School of

The University of Texas at Austin

in Partial Fulfillment

of the Requirements

for the Degree of

DOCTOR OF PHILOSOPHY

The University of Texas at Austin

August 2018

Acknowledgments

Many people were involved in the development and writing of this dissertation, more than I can properly thank. I would like to start by thanking my very first supporters, my family. My parents always enabled an early interest in science and space, to the point that they happily sent me to Space Camp three times. They listened to me whenever I felt stuck in my research, and encouraged me to continue to the end. My brother always helped keep my spirits up, usually by making me laugh with his outlandish antics. The entirety of my (rather large) extended family, grandparent, aunts, uncles, and cousins, have similarly spurred me on with their love and support.

I would especially like to thank my academic advisor, Dr. Russell. The nine years I've spent working with him have given me confidence and skills I would not have otherwise, through both his technical expertise and obvious care for my well-being as his student. Dr. Russell has been instrumental throughout the course of my research, often by identifying what I considered to be minor ideas, and helping develop them into major contributions of the dissertation. Thanks largely to him, the time and effort spent getting my doctorate has been incredibly enjoyable.

Much of the early groundwork for this dissertation was supported by funding through NASA and the Jet Propulsion Laboratory via the Graduate

Student Research Program. I would like to thank Dr. Petropoulous for his role in helping to promote my proposal and secure this funding. His shared expertise and mentorship led to many of the key developments that laid the foundation and ultimate direction of my research in low-energy dynamics. I would also like to thank Dr. Gregory Lantoine for recruiting me to work on his proposal for the NASA Innovative Advanced Concepts program, providing additional funding and leading to the work with electrodynamic tethers that would become a part of this dissertation.

Typically dissertation committees are formed early on, so that the members can follow the work and provide input along the way. Due to some atypical faculty shifting in the form of retirements, departures, and transfers, my final committee was formed nearly at the end of my research. To that end, I would like to thank Dr. Bettadpur, Dr. Akella, and Dr. Jones for joining my committee so late in the process, taking the time to read through and critique my work, and for their insightful questions during the defense that led to further improvement of the final dissertation.

Lastly, I would like to thank all of the graduate ASE friends I made over the course of my time here at the University of Texas. The trials of going through written, then oral examinations were made easier knowing I had company to study with. While we were working on different projects, the process felt very much like a team effort. I look forward to working with you all again in the future.

Exploration and Optimization of Low-Energy Capture Options at Jovian Moons

by

Kevin Andrew Bokelmann, Ph.D.
The University of Texas at Austin, 2018

SUPERVISOR: Ryan P. Russell

A key trade-off for planetary system exploration is the fuel cost required versus science data obtained. Historically, planetary systems have been explored utilizing multiple flybys, such as Galileo, Cassini's complex Saturnian tour, as well as the trajectory for the proposed Europa Clipper mission. While this approach eliminates the need for expensive capture maneuvers, it can require days to weeks between observations, limiting available science data. An alternative that seeks to maximize science return is to capture about each moon of interest. Investigations of low-energy dynamics have shown the existence of relatively inexpensive transfers between halo orbits at different moons. Chaining these transfers in a moon-hopping tour allows one spacecraft to visit multiple moons. The next step for a multi-moon mission is to connect the inter-moon transfers to science orbits at specific moons. Two capture orbit scenarios are considered for comparison: 1) traditional, tightly captured low-altitude orbits and 2) low-energy, loosely captured high-altitude orbits.

Near-global grid search methods are developed to generate initial capture trajectories from staging halo orbits. To help determine which solutions are near optimal, an analytical expression for the predicted floor cost is derived. Low cost captures are identified and optimized using impulsive primer vector theory to determine the ideal number and location of impulses. The trajectory is then extended to include the last resonant-orbit of the inter-moon transfer, using the halo orbit as a patch point to connect the phases. A new three-dimensional periodic orbit that naturally transfers between the resonant and halo orbits is generated to facilitate the connection. The resulting resonant-to-capture transfers are again optimized with primer vector theory, resulting in several optimized options for comparison. As an additional mission design option, the possibilities of advanced exploration using an electrodynamic tether are investigated. An approximation to the tether-perturbed dynamics is derived that allows for an integral of motion, enabling useful analytical techniques. New periodic orbit families are generated as a function of tether length, using continuation from non-perturbed Lyapunov orbits. The new orbits are analyzed in terms of stability and utility for future use in mission design.

Table of Contents

List of Tables

List of Figures

Chapter 1

Introduction

1.1 Motivation

The design of planetary system exploration missions is a challenging balance of science return versus propulsive cost. A critical component of dedicated orbiter missions is the endgame problem: the final sequence of trajectories leading to capture. High-value science orbits tend to be low-altitude, high-inclination trajectories that can provide global mapping, whereas the capture maneuvers required for such orbits may be prohibitively expensive, particularly for large planetary moons of interest such as Europa or Titan. To date there have been no dedicated orbiters about any planetary moon other than our own. Science returns have historically been limited to observations performed over the course of multiple flybys. The most famous example of this approach is the Cassini-Huygens mission which performed 162 flybys of Saturn's moons, and landed a probe on the surface of Titan [47]. The proposed Europa Clipper mission will similarly map out Jupiter's moons with a series of close Europa approaches [8].

While the science returns from flyby-based missions have been exceptional, there are limitations. Notably, the time gap of days to months between

close approaches limits in-depth study of short-term phenomena. A dedicated orbiter remains as an appealing option that enables continuous observation. Dedicated orbits at multiple moons is especially desirable to maximize the science gain for planetary system exploration. The options to achieve a multi-moon tour are effectively limited to either a complex architecture of multiple orbiters, or a single orbiter that targets several moons. The need for expensive capture and departures maneuvers, along with inter-moon transfers, makes the single orbiter mission approach propulsively infeasible for designs based on standard two-body orbital dynamics.

Fortunately, the compact Jupiter and Saturn systems are ideal for taking advantage of third-body perturbations to achieve otherwise infeasible trajectories. Recent and ongoing research has already shown that near-ballistic transfers between libration points at Jupiter's moons exist, eliminating one major cost of a multi-moon tour. Related works have found highly-perturbed capture orbits that can be used to observe and map out moons at a fraction of the cost of traditional science orbits. A survey of these studies is explored in the next section. The combination of these two key developments significantly reduces the prohibitive propulsive costs. However, the methods used for these studies decouple the transfer and capture problems, i.e there are no complete trajectories from the inter-moon phase through to the capture orbit. What remains then is the need for an investigation into connecting the two phases into a full trajectory to enable a true single orbiter, multi-moon mission.

The succeeding sections of this chapter discuss the background of the

ideas and techniques used within this dissertation, followed by a layout of the dissertation structure and a summary of the contributions from this work. The background sections are intended to be a concise overview of past and recent works to aid the reader's understanding of the relevant material, rather than a comprehensive literature review of all mission design and optimization. The first section provides an overview of the history of low-energy trajectory design, as well as recent developments focused on the Jupiter system. Next is a discussion about impulsive primer vector theory in the context of trajectory design. The last background section provides motivation and information for a potential advanced, mission enabling technology: electrodynamic tethers.

1.2 Trajectory Design utilizing Low-Energy Dynamics

The analysis of chaotic dynamical systems begins with Henri Poincaré's research in the late 19th century [78]. His work is the foundation for the theory of dynamical systems, deriving many of the techniques still used to study trajectories in the three-body problem. Key developments include proof of the existence of libration point orbits and periodic solutions, the concept of using repeat trajectory crossings of a surface to map phase space (now fittingly referred to as Poincaré maps), and the existence of asymptotic approach and departure trajectories of libration points, known as invariant manifolds. Over 70 years later advances in computational power enabled numerical techniques to thoroughly investigate the dynamics, primarily through the generation and analysis of periodic orbits about libration points [14, 36–39, 44, 63, 66]. Con-

currently, the advent of lunar spacecraft led to interest in the application of these orbits to trajectory design. One of the first methodologies to generate low-energy transfers was developed by Conley for Earth-Moon transit orbits (using the equivalent of invariant manifolds) [23]. Further development of these low-energy techniques culminated in practical application to multiple mission designs [17, 30, 103]. A relatively recent example is the GRAIL mission to map the Moon's gravitational field, which utilized the dynamics of the Earth-Sun system to significantly reduce the cost of lunar orbit insertion [21]. In the near future, NASA's planned Lunar Orbital Platform - Gateway intends to place a manned station in a lunar halo orbit [15, 16].

The complex dynamics of the Jupiter and Saturn systems make them well-suited for low-energy trajectories as part of the mission endgame. As mentioned in the previous section, a common strategy to simplify the endgame problem is to decouple it into two main phases:

1) The final trajectories leading to approach of the moon's sphere of influence

2) Capture into a dedicated science orbit

An unstable periodic orbit, such as a halo orbit, is typically used as a boundary condition to decouple the endgame phases, turning each phase into two-point boundary value problems. The approach phase primarily focuses on the final sequence of orbits that lead to favorable capture conditions. Given that the Jovian system consists of several gravitationally significant moons, multiple

studies have utilized flybys to sequentially reduce the energy of the spacecraft relative to Europa. A useful starting point for approach trajectory design is to approximate the system with patched two-body dynamics when far from the planetary moon, as it allows fast, analytical approaches [4, 5, 31]. The resulting trajectories can then be used as initial guesses for refinement in higher fidelity dynamical models. As a practical example of this approach, Campagnola and Russell used V-infinity leveraging to design multi-moon tours [18]. These authors then extended leveraging to the multi-body realm using the Tisserand parameter, creating a graphical tool for preliminary studies [19]. This tool was effectively used to design low-energy transfers with timespans comparable to high-energy options [20].

Rather than start with two-body approximations, the natural dynamics of the multi-body system can also be expressed via invariant manifolds. Initial work by Koon et. al showed that intersections of these manifolds form near-ballistic transfers between periodic orbits at similar energy levels [46]. Connections within the same periodic orbit are referred to as homoclinic, whereas heteroclinc connections exist between different periodic orbits. In general, invariant manifolds can be used to generate transfers between any periodic orbits at different energies [28]. Vaquero and Howell utilized this approach to connect unstable resonant orbits in the Earth-Moon system [101]. Related work by Lantoine et al. investigated connecting two moons using a combination of multi-body and patched three-body dynamics, with halo orbits as boundary conditions [54]. Their results, as well as work by Grover and Ross, show that

such transfers can be completed with relatively low ΔV (on the order of tens of meters per second) [35]. Restrepo and Russell showed that similar transfers can be simply constructed by patching together periodic orbits with natural transfers between different families, avoiding the complexity of generating and connecting unstable manifolds [81]. The selection of patching orbits requires searching a large database of previously generated periodic orbit families [80].

The final phase of the endgame problem consists of the transfer to a capture orbit, as well as design of the capture orbit itself. Moons such as Europa have strongly perturbed orbits due to non-spherical gravitational fields and close proximity to Jupiter, significantly reducing capture orbit lifespans. Paskowitz and Scheeres sought the conditions needed for long lifetime orbits on the order of 150 days via averaging techniques [72]. Lara and Russell found similar long lifetime science orbits at Europa using highly resonant periodic orbits [56]. Alternatives to orbits deep in the gravity well of moons have been proposed as descope options to reduce propulsive cost. Russell and Brinckerhoff investigated the use of circulating eccentric orbits that provide near-global coverage while avoiding tight capture [86]. These high-altitude orbits take advantage of the third-body perturbations from Jupiter, leading to close approaches distributed above the moon's surface. However, the orbits can be difficult to classify due to their chaotic nature. Davis and Howell sought to identify the short and long-term behavior of similar chaotic orbits using periapse Poincaré maps [25]. At the lowest propulsive cost, capture can be avoided altogether by chaining transfers between periodic orbits using un-

stable manifolds [6, 71]. In certain cases these transfers are effectively free, allowing multiple viewing angles and close approaches for minimal cost.

The existence of a broad range of capture orbit options leads to the development of different techniques to generate approach to capture transfers. Baoyin and McInnes looked into transfers from the Lagrange points and Lyapunov orbits that provide whole-surface coverage of both primaries using numerical integration and invariant manifolds of the three-body dynamics [7]. Work by Russell and Lam used stable manifolds of unstable periodic orbits to generate ballistic capture trajectories to highly-inclined Europa science orbits, before transitioning to a low-thrust ephemeris model [87]. Anderson classified the required final approach resonances when using invariant manifolds of Lyapunov orbits, and showed that the costs to capture from either resonant or Lyaponuv orbits can be equivalent [4]. The reverse problem of escape from low-altitude circular orbits was investigated by Villac and Scheeres for multiple Jovian and Saturnian moons through the use of Poincaré maps [102]. Purely ballistic captures in the n-body ephemeris model were investigated by Luo et al. via a grid of osculating orbital elements, with classification of the captures based on a stability index [62].

The chaotic nature of the dynamics makes it difficult to readily compare the different mission architectures proposed. Transfer trajectories are strongly dependent on specific boundary conditions and are generally expensive to compute and optimize. The ability to rapidly predict the optimal cost without finding physical transfers (i.e. numerically propagated trajectories)

is desirable for quick evaluation of mission design options. Sweetser showed that an optimal maneuver is tangential to the rotating velocity and related to the change in Jacobi constant [96]. Davis further showed that finding the minimum ΔV requires maximizing the rotating velocity, although no explicit minimizing location was given due to minimal variations when close to the capture body [26]. Mengali and Quarta derived an expression for approximating the minimum ΔV for planar, bi-impulsive transfers between tight captures at the Earth and Moon, again assuming close proximity to the capture body [65].

1.3 Primer Vector Theory

Optimization of spacecraft trajectories is a historic problem with multiple approaches, broadly categorized as direct gradient methods, indirect methods, and hybrids. For details on the general optimization problem, the interested reader is referred to several resources; the focus of this dissertation is on the hybrid use of impulsive primer vector theory [24, 50, 51, 100]. This theory was introduced by Lawden, who utilized calculus of variations to derive conditions for the optimality of a time-fixed, impulsive spacecraft trajectory subject to an inverse-square gravity field [60]. Lion and Handelsman extended the theory to non-optimal trajectories, deriving the conditions for the locations and times where additional impulses will improve the cost of the trajectory [61]. These equations were used by Jezewski and Rozendaal to develop an algorithm for iteratively adding impulses to the trajectory, including a first-order

prediction for the magnitude of the interior impulse that leads to the greatest cost reduction [43]. Finding these additional maneuvers is a key advantage of primer vector theory over direct optimization methods [49].

Primer vector theory was extended to the Elliptical-Restricted Three-Body Problem by Hiday, who optimized transfers between libration point orbits [41]. Davis later noted that the primer vector equations and optimality conditions in the Circular-Restricted Thee-Body Problem (CRTBP) are essentially identical to those derived by Hiday [26]. A notable problem for primer vector theory when applied to low-energy dynamics is that it traditionally requires at least two impulses to generate the primer vector history. However, the use of invariant manifolds often results in transfers with a single impulse, such as ballistic capture trajectories. Davis avoided this complication by creating two-impulse bridging transfers between manifolds [27]. An alternative approach by Griesemer derived new necessary conditions on the primer vector at the time that the spacecraft is considered ballistically captured [34].

1.4 Electrodynamic Tethers

Among many unique challenges of outer planet missions, the extreme distances from the sun lead to restrictive power constraints. In particular, the use of solar arrays is limited due to solar radiation decreasing as an inverse square law. While the ongoing Juno mission to Jupiter is able to make use of solar cells, its power is less than 500 W, limiting its science capabilities [68]. The common alternative to solar power is the use of radioisotope thermal

generators (RTGs) such as those used for the Cassini and Galileo missions. RTGs come with their own set of design challenges.

A developing alternative is making use of electrodynamic tethers and their interaction with the rotating magnetic fields of planets. Jupiter is of greatest interest due its strong magnetic field, but magnetic fields also exist at the other gas giants and at the Earth. The premise of using a tether to provide power relies on basic principles of electromagnetism, namely, that current is induced when a conductor moves through a magnetic field in the presence of a plasma ambient. This current generation makes for an attractive alternative power source for spacecraft [89, 91]. Power scarcity is a common limiting factor in spacecraft design, making any additional power of much practical interest. Research has explored power generation in different motion regimes including system satellite tours and orbiters that are stationary relative to a secondary body [10, 12, 94].

The second capability of electrodynamic tethers is as a force generator. Charged particles (such as current in a tether) moving through a magnetic field generate the so-called Lorentz force. The force naturally occurs during power generation from an induced current, but it can also be created by providing artificial current from an on-board power source, resulting in controllable thrusting. This nonconservative force is a function of position, velocity, tether orientation, the characteristics of the tether material, and the plasma ambient. Given that this force can be generated with negligible propellant necessary for attitude control and the tether hollow cathode, there is potential for sig-

nificant mass savings. Applications with the largest potential for propellant mass reduction include departure and capture for interplanetary trajectories, as these typically require large fractions of propellant budgets. Ongoing research shows that capture from hyperbolic orbits can be greatly assisted, if not completely performed by, electrodynamic tethers [32, 90, 93]. Additional work by Tragesser and San shows how tethers can be used for orbital transfers about a single body [98]. Also of interest is the mass efficiency of tethers for these transfers relative to electric thrusters, noting research has shown that tether systems can allow mass savings over long-term applications [92].

The addition of the Lorentz force also alters the equilibrium points in unperturbed systems such as the CRTBP. Research has been done on the stability and dynamics for tethers operating at these modified equilibrium points, typically in the interest of power generation with the tether without altering the orbit of the spacecraft. Various analyses have shown that these equilibrium points are stable or can be made stable through the use of control laws [11, 74, 75, 104]. A natural next step is to expand these perturbed equilibrium points into periodic orbits in the Lorentz force-perturbed CRTBP. Periodic orbits are useful for a variety of applications including parking orbits and intermoon transfers and as descope alternatives to science orbits [48, 53, 86]. The addition of a tether can make spacecraft self-powered but introduces Lorentz forces that will alter the orbits. Knowledge of the effects of these forces on orbit orientation and stability is needed for a full end-to-end mission design with tethers.

1.5 Outline of Dissertation

The dissertation is structured with the intent to follow the logical progression of the work presented. Chapter 2 is a non-contribution chapter where the models and methods common to multiple chapters are discussed. This centralized approach eliminates repetition while keeping specific techniques in their respective chapters for ease of reference. Chapter 3 and Chapter 4 follow the natural progression of finding resonant to capture orbit transfers using a halo orbit for patching. Chapter 3 discusses the methods developed to generate halo to capture transfers, with emphasis on the need for different approaches based on the type of capture. These trajectories then serve as initial guesses for optimization in Chapter 4, which builds off the optimized trajectories to construct full resonant to capture transfers. Chapter 5 investigates the dynamics with perturbations from an electrodynamic tether, which enables unique families of periodic orbits. The concept is approached with the overarching motivation of reducing the costs of planetary system exploration using low-energy dynamics. Lastly, Chapter 6 provides concluding remarks for the contributions of the work, and discusses possible future extensions.

1.6 Summary of Contributions

1.6.1 Chapter 3

- A new general analytical expression is derived for the minimum ΔV required to transfer between bounding energy levels in both the CRTBP and Hill's models.

- Finds the first known survey of transfers from halo orbits targeting specific low-altitude Europa science orbits, as well as transfers to chaotic loose capture orbits.

1.6.2 Chapter 4

- First known case in the literature of the application of primer vector theory to optimize n-impulse, highly-sensitive, multi-revolution trajectories in the CRTBP.
- Derivation of new equations using the primer vector to remove small impulses from the trajectory, eliminating singularities from the optimization problem.
- Development of a hybrid optimization algorithm, including numerical methods to mitigate the sensitivities of the transfers and meet the strict optimality conditions required by impulsive primer vector theory.

1.6.3 Chapter 5

- A conservative approximation for the Lorentz force from a radial electrodynamic tether is derived, facilitating the application of analytical and numerical techniques that require an integral of motion.
- Generation of the first known tether-perturbed periodic orbit families, with orbits characterized by tether length and motion integral.

Chapter 2

Models and Methods

In this chapter the non-contribution methods common throughout the dissertation are presented. The majority of the chapter is devoted to the dynamics of the CRTBP, including periodic orbit generation. Concise summaries of the state transition matrix and complex step differentiation are also provided. For details on primer vector theory, see Chapter 4. The equations relevant to electrodynamic tethers are presented in Chapter 5.

2.1 The Circular-Restricted Three-Body Problem

The framework used for the dynamics is the barycentric form of the CRTBP [45, 97]. Figure 2.1 depicts the xy-plane of the rotating frame, with the z-axis completing the right-handed coordinate system. The system is normalized to derived length and time units (LU and TU), where 1 LU is the mean distance between the primaries and TU is set such that the system angular velocity is one radian per time unit. The normalized equations of motion for a spacecraft in the CRTBP are expressed as:

$$\ddot{\mathbf{r}} + 2\mathbf{\Omega} \times \dot{\mathbf{r}} = \nabla J \tag{2.1}$$

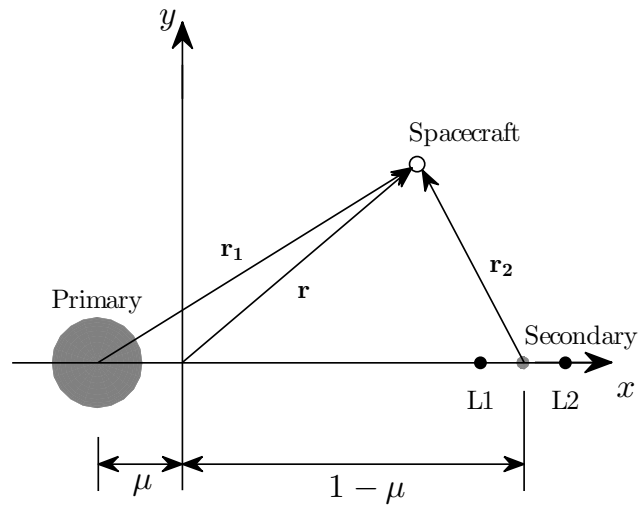

Figure 2.1: The xy-plane of CRTBP rotating frame and coordinate system, including the locations of the primaries, spacecraft position vectors, and first two Lagrange points

$$J = \frac{(x^2 + y^2)}{2} + \frac{1-\mu}{r_1} + \frac{\mu}{r_2} \tag{2.2}$$

where μ is defined as the mass ratio of the secondary to the total system mass, $\mathbf{r}(x, y, z)$ is the spacecraft position vector, $\dot{\mathbf{r}}(u, v, w)$ is the spacecraft velocity relative to the rotating frame, $\mathbf{\Omega} = [0\ 0\ 1]^{\mathrm{T}}$ is the normalized frame rotation rate, and J is the pseudo-potential given by Equation (2.2).

The full spacecraft state is denoted as $\mathbf{x} = [x, y, z, u, v, w]^{\mathrm{T}}$. The spacecraft distances to the primary and secondary are r_1 and r_2, respectively. There is one energy-like integral of motion known as the Jacobi constant, defined as $C = 2J - V^2$, where $V = ||\dot{\mathbf{r}}||$. An approximation of the region where the secondary dominates the dynamics of the system is given by the Hill radius:

$R_{\text{Hill}} = \sqrt[3]{\mu/3(1-\mu)}$. In this work, the Hill radius is used to define a region where the spacecraft is considered to be within the influence of the secondary.

Five equilibrium points exist in the equations of motion, known as the Lagrange points L_i. Only the first two points, depicted in Figure 2.1, are relevant in this work due to their proximity to the secondary. Simple three-dimensional periodic orbits about these points exist, known as halo orbits. These orbits are commonly used to decouple the capture problem from the approach problem, as in Reference [54] where the halo orbits are used as boundary conditions.

2.1.1 Periodic Orbit Generation

The equations of motion of the CRTBP are known to exhibit symmetries due to invariance to specific variable transformations; this symmetry is useful to search for periodic orbits [42, 85]. The first invariance occurs under the transformation $\{y = -y,\ t = -t\}$, such that a forward-time trajectory has a corresponding reverse-time trajectory mirrored through the xz-plane. Accordingly, if the initial state of the forward trajectory is a perpendicular crossing of the xz-plane, the mirrored, reverse-time trajectory is as well, resulting in a single, continuous trajectory. The second invariant transformation is $\{y = -y,\ z = -z,\ t = -t\}$. The resulting forward-backward symmetry is a 180° rotation about the x-axis. A forward trajectory that starts on and perpendicular to the x-axis will be continuous with its reverse-time counterpart. By targeting a combination of xz-plane and x-axis crossings for both

initial and final states, the combined symmetric trajectories will be a fully continuous periodic orbit. Different targeting algorithms exist, however the general approach is to use differential correction to target $\mathbf{k}(\boldsymbol{\xi}) = \mathbf{0}$, where $\mathbf{k}$ is the difference vector between actual and target states at the end of the trajectory, and $\boldsymbol{\xi}$ is the vector of free state variables [88]. Symmetry-based targeting algorithms are discussed in Chapter 4. Periodic orbits can also be generated by targeting the full initial state after one orbital period, which is discussed in Chapter 5.

Once a periodic orbit has been identified it can be numerically continued into a full family of periodic orbits, characterized by their initial state $\mathbf{x}_0$ and periodic time, T [3, 33]. Continuation is initialized by selecting an independent variable referred to as the generating parameter, and treating the remaining states as functions of this parameter. The independent variable is typically chosen based upon the periodic orbit generating method, as it is held constant during targeting. Common parameter selections are one of the orbit initial position variables or the Jacobi constant. A family is followed by perturbing the generating parameter and differentially correcting the remaining initial states to a new periodic orbit. The size of the first perturbation is generally small such that the differential corrector can successfully converge. Larger step sizes are enabled by using extrapolation to guess the initial state and period of the next orbit in the family as a function of the generating parameter.

Occasionally one or more variables of the family may go through "re-

flections", where the direction of the generating parameter must reverse in order to further continue the family. A simple solution is to switch to a different generating parameter whenever a reflection is encountered. However, reflections can be avoided entirely by using the pseudo-arc-length continuation method. A new variable, ρ is defined to be approximately equal to the arc-length traveled along the family curves. This definition makes ρ a strictly monotonic variable, preventing reflections. The pseudo-arc-length is initialized by starting continuation with a different generating parameter. After at least two periodic orbits have converged a guess length, $\rho^* = \rho_i + \Delta\rho$, is used to extrapolate the initial state of the next periodic orbit, where $\Delta\rho$ is a freely chosen step size. Once a new periodic orbit is found, the actual pseudo-arc-length is updated such that $\rho_{i+1} = \rho_i + ||\mathbf{x}_{0,i+1} - \mathbf{x}_{0,i}||$, where $\rho_0 = 0$ and $\mathbf{x}_{0,i}$ is the initial state of the ith converged periodic orbit.

2.1.2 Invariant Manifolds

Periodic orbits are often unstable, such that a small perturbation leads to rapid departure from the orbit. The family of ballistic transfers that asymptotically depart in this manner are called the unstable manifolds of the orbit. Propagating the perturbation in reverse-time generates stable manifolds that asymptotically approach the orbit in forward-time. These trajectories serve as a natural first guess for efficient transfers to or from periodic orbits. In-depth discussions of generating manifolds are found in References [87] and [45], a brief summary is presented here. Evaluating the state transition matrix (STM) over

one full period gives the monodromy matrix $\mathbf{\Phi}(T, t_0)$ (see Section 2.2). The eigenvector of this matrix with the maximum real eigenvalue is the unstable perturbation direction at the initial time, $\boldsymbol{\xi}(t_0)$. This direction can be mapped to any other time through the STM: $\boldsymbol{\xi}(t) = \mathbf{\Phi}(t, t_0)\,\boldsymbol{\xi}(t_0)$. The initial state for the manifold that leaves the periodic orbit at time t, $\mathbf{x}_\epsilon(t)$, is found by adding a small perturbation to the full state in the unstable direction with magnitude ϵ:

$$\mathbf{x}_\epsilon(t) = \mathbf{x}(t) \pm \epsilon \frac{\boldsymbol{\xi}(t)}{||\boldsymbol{\xi}(t)||} \tag{2.3}$$

The alternating sign addresses that the perturbation can be made in either direction along the perturbation vector. The choice of sign generally determines if the manifold departs towards or away from the secondary. Both directions are used in this dissertation.

2.1.3 Europa-Jupiter System

Table 2.1: Jupiter-Europa system CRTBP parameters

Parameter	**Value**
Europa Semi-major Axis; LU, km	6.711×10^5
Europa Mean Radius, km	1560.70
Jupiter Mean Radius, km	71,942.0
Europa GM, km^3/s^2	3,202.73879
Jupiter GM, km^3/s^2	1.26686535×10^8
Mass Ratio; μ	2.5280175×10^{-5}
TU, s	48,843.88

The Jupiter-Europa system is selected for in-depth analysis due to significant scientific interest; the Decadal Survey named Europa as the top outer-planet destination, leading to numerous mission design studies [22, 77]. Recall

from Chapter 1, the Europa Clipper is a planned mission in development by NASA's Jet Propulsion Laboratory to perform science at Europa via multiple flybys [1, 8]. A summary of the parameters used to model the CRTBP of the Jupiter-Europa system is given in Table 2.1 [2]. When calculating two-body orbital elements for capture at Europa, a non-rotating frame centered at Europa is used, with the axis aligned with the CRTBP frame at the start of the integration.

2.2 The State Transition Matrix

Small perturbations to a trajectory are linearly mapped to a later time using the STM, $\mathbf{\Phi}(t, t_0)$, where t_0 is the time at the initial state [99]. The matrix is generated by integrating the variational equations alongside the equations of motion:

$$\dot{\mathbf{\Phi}}(t) = \frac{\partial \dot{\mathbf{x}}}{\partial \mathbf{x}}(t)\mathbf{\Phi}(t, t_0), \qquad \mathbf{\Phi}(t_0, t_0) = \mathbf{I}_6 \tag{2.4}$$

$$\mathbf{\Phi}(t, t_0) = \begin{bmatrix} \mathbf{A} & \mathbf{B} \\ \mathbf{C} & \mathbf{D} \end{bmatrix} \tag{2.5}$$

where $\mathbf{I}_6$ is the 6×6 identity matrix. The full perturbation state mapping is evaluated as $\delta\mathbf{x} = \mathbf{\Phi}(t, t_0)\delta\mathbf{x}_0$. Often only part of the STM is required, such as when mapping velocity-only perturbations to position differences. For ease of reference in these partial cases, the STM is partitioned into four 3×3

submatrices, shown in Equation (2.5). Two important properties of a general STM are that:

1) They can be chained together in sequence: $\mathbf{\Phi}(t_2, t_0) = \mathbf{\Phi}(t_2, t_1)\mathbf{\Phi}(t_1, t_0)$

2) The inverse of the matrix is identical to the reverse time STM: $\mathbf{\Phi}(t_1, t_0)^{-1} = \mathbf{\Phi}(t_0, t_1)$.

2.3 Complex Step Finite Differentiation

A critical necessity in optimization problems is obtaining accurate derivatives. Assuming analytical equations are unavailable, there are multiple well-known numerical methods that use finite differences to approximate derivatives. A key driver for the accuracy of these methods is the step size, h, with the exact derivative occurring in the limit as h goes to zero. However, the use of subtraction leads to machine precision errors that place a lower limit on useful step size (on the order of 10^{-8} for double precision).

In order to obtain high accuracy derivatives, this dissertation takes advantage of the relatively simple complex step method [64]. The derivative is approximated as:

$$f^{'}(x) \approx \frac{\mathrm{Im}\left[f(x + ih)\right]}{h} \tag{2.6}$$

Essentially, complex arithmetic is utilized to obtain the finite difference as the imaginary part of the function, avoiding subtractions. This approach allows h

to be sufficiently small (i.e. on the order of 10^{-50} or smaller) that the derivatives can be considered exact to working precision.

Chapter 3

Generating Halo to Capture Transfers[1]

In this chapter, the problem of generating feasible transfers from halo orbits to different capture orbit options is investigated. The chapter begins by deriving an energetic equation for the floor transfer ΔV in both the CRTBP and Hill's models. The development of analytical expressions for a lower ΔV bound as a function of boundary conditions leads to a simple and rapid tool for preliminary mission design. Extending the expressions to the Hill's model makes it possible to scale the results to any body of interest. A provided application is an archived table giving estimated capture costs for a broad survey of planet-moon systems from the L2 halo family. Next, applied grid searches for transfers are developed based on capture type (tight or loose). Comparison of the actual propulsive costs shows the energetic minimum is likely a true lower bound. The resulting loose captures provide a broad selection for mission design trade studies, such as mapping coverage versus predictable, quasi-periodic orbits.

[1]Bokelmann, K.A., Russell, R.P., "Halo Orbit to Science Orbit Captures at Planetary Moons," Acta Asronautica, Vol. 134, May 2017, pp. 141-151, https://doi.org/10.1016/j.actaastro.2017.01.035
Technical work and writing by Bokelmann, with guidance and edits by Russell

3.1 Lower Bound Transfer Delta-V

When constructing transfers between orbits at different energy levels, it is useful to know the expected minimum ΔV for comparison. Given that the bounding orbits have distinct Jacobi constants, an energy-like approach based on the fixed ΔC is employed to derive an analytical expression for the minimum. It is shown in References [102] and [96] that the energy change is optimally achieved with a single impulsive maneuver tangential to the velocity in the rotating frame. A theoretical ideal transfer with this property would be one that ballistically departs the initial orbit via unstable manifolds, and then intersects the capture orbit such that a single tangential maneuver is sufficient for capture. Note that this ideal transfer ignores the constraints of a physical transfer; feasible transfers may require multiple impulses or non-tangential directions to be optimal.

The assumed single impulse leads to the bounded problem of finding the minimum ΔV to achieve a given ΔC. Differentiating the Jacobi constant shows $dC = -2V dV$, as an impulse can only change velocity. It is apparent that maneuvers become more efficient at higher velocities, analogous to the two-body problem. Finding the minimum ΔV therefore requires first finding the position location of maximum velocity. The derivation is initially developed in the CRTBP model. While this derivation is system specific it allows the equation to be applied far from the secondary, such as during the resonant transfer phase connecting two moons. A second derivation in the Hill's model removes dependency on a specific three-body system, enabling a rapid survey

over numerous bodies of interest, but limits the equation accuracy to orbits near the secondary.

3.1.1 Derivation in the CRTBP

The position location of the minimum ΔV is first formulated in the CRTBP. To initially reduce the problem to two variables, the location is limited to a sphere of constant radius. Spherical coordinates relative to the secondary are used to represent the location:

$$\begin{aligned} x &= -r_2 \cos\phi \cos\lambda + 1 - \mu \\ y &= -r_2 \cos\phi \sin\lambda \\ z &= -r_2 \sin\phi \end{aligned} \tag{3.1}$$

where r_2 is the distance from the center of the secondary, ϕ is the angle above the xy-plane, and λ is the angle in the xy-plane measured counterclockwise from the negative x direction. For synchronous, tidally-locked moons, the angular coordinates are in agreement with IAU planetocentric conventions of latitude and longitude. Terminology of "interior" and "exterior" sides of the secondary is introduced to refer to $\lambda = 0$ and π, respectively.

The Jacobi integral is rearranged to solve for V^2, expressed in terms of the spherical coordinates:

$$
\begin{aligned}
V^2 &= -r_2^2 \cos^2\phi - 2r_2\left(1-\mu\right)\cos\phi\cos\lambda + \left(1-\mu\right)^2 + \frac{2\left(1-\mu\right)}{r_1} + \frac{2\mu}{r_2} - C \\
r_1 &= \left(r_2^2 - 2r_2\cos\phi\cos\lambda + 1\right)^{1/2}
\end{aligned}
\tag{3.2}
$$

where r_1 is the distance between the spacecraft and the primary. The square of the velocity is used to simplify the equations and derivatives. Derivatives with respect to the angles are taken to find locations of extrema:

$$
\begin{aligned}
\frac{\partial\left(V^2\right)}{\partial\phi} &= 2r_2\kappa\sin\phi \\
\kappa &= \cos(\lambda)\left(1-\mu\right)\left(1-\frac{1}{r_1^3}\right) - r_2\cos\phi
\end{aligned}
\tag{3.3}
$$

$$
\frac{\partial\left(V^2\right)}{\partial\lambda} = 2r_2\left(1-\mu\right)\left(1-\frac{1}{r_1^3}\right)\cos\phi\sin\lambda \tag{3.4}
$$

where κ is introduced to simplify Equation (3.3). Note that the derivatives are independent of Jacobi constant. The Hessian matrix, $\mathbf{H}$, is also derived and its eigenvalues are computed to characterize each extrema. All positive eigenvalues indicate a minimum, all negative eigenvalues indicate a maximum, and a combination of both indicates a saddle point.

$$
\begin{aligned}
\mathbf{H} &= \begin{bmatrix} \frac{\partial^2 V^2}{\partial \lambda^2} & \frac{\partial^2 V^2}{\partial \lambda \partial \phi} \\ \frac{\partial^2 V^2}{\partial \lambda \partial \phi} & \frac{\partial^2 V^2}{\partial \phi^2} \end{bmatrix} \\
\frac{\partial^2 V^2}{\partial \lambda^2} &= 2r_2 \left(1-\mu\right) \cos\phi \cos\lambda \left[\frac{3r_2 \cos\phi \sin\lambda \tan\lambda}{r_1^5} + \left(1 - \frac{1}{r_1^3}\right) \right] \\
\frac{\partial^2 V^2}{\partial \phi^2} &= 2r_2 \left(1-\mu\right) \cos\phi \cos\lambda \left[\frac{3r_2 \sin\phi \cos\lambda \tan\phi}{r_1^5} + \left(1 - \frac{1}{r_1^3}\right) \right] + 2r_2^2 \left(\sin^2\phi - \cos^2\phi\right) \\
\frac{\partial^2 V^2}{\partial \lambda \partial \phi} &= 2r_2 \left(1-\mu\right) \sin\phi \sin\lambda \left[\frac{3r_2 \cos\phi \cos\lambda}{r_1^5} + \left(1 - \frac{1}{r_1^3}\right) \right]
\end{aligned}
\tag{3.5}
$$

Root-solving Equations (3.3) and (3.4), then evaluating the eigenvalues at the roots shows that the velocity maxima occur on the x-axis (i.e. $\phi = 0$, $\lambda = 0, \pi$). Comparing velocities at the interior versus exterior of the secondary shows that the interior is the global maximum when the distance from the secondary, r_2, is less than unity. Radii larger than that value are well beyond a feasible capture; therefore in this work the global velocity maximum occurs on the interior x-axis in-between the primary and secondary.

The minimum ΔV for a specified capture radius r_2 is found by evaluating the maximum velocities for values of Jacobi constant before and after the maneuver, C_- and C_+. Substituting the location of the global maximum into Equation (3.2) and taking the difference in velocities leads to a simple analytical expression for the theoretical minimum impulse magnitude:

$$
\begin{aligned}
\Delta V &= \left| \sqrt{A - C_+} - \sqrt{A - C_-} \right| \\
A &= \left(1 - \mu - r_2\right)^2 + \frac{2\left(1-\mu\right)}{1 - r_2} + \frac{2\mu}{r_2}
\end{aligned}
\tag{3.6}
$$

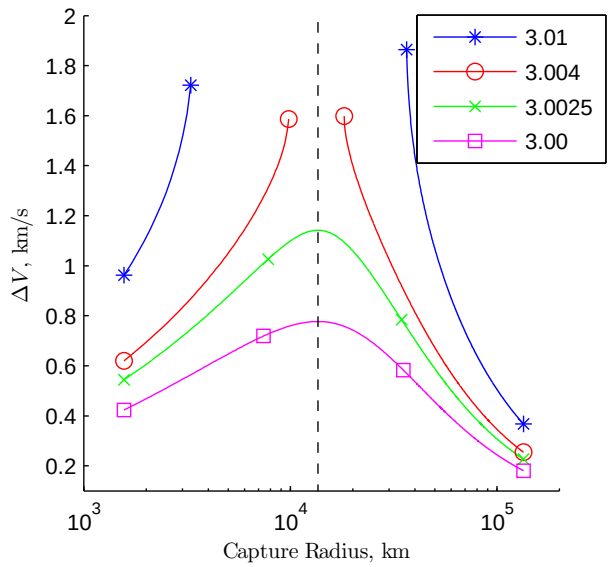

Figure 3.1: Analytical minimum ΔV for capture from $C_- = 2.990$ LU^2/TU^2 to several C_+ values, as capture radius r_2 is varied. Dashed line indicates L1 point

The analytical minimum ΔV is plotted in Figure 3.1 for several energetic arrival conditions. Note that discontinuities in the lines occur due to that range of r_2 being inaccessible for the given value of capture Jacobi constant. The plot shows that ΔV increases with distance from the secondary up to the L1 point, indicated by the vertical dashed line. Typical science orbits require altitudes closer than L1, indicating that efficient capture maneuvers should occur at the smallest feasible radius relative to the secondary.

3.1.2 Application to a Range of Departure and Capture Orbits

Equation (3.6) can be rapidly applied over a broad survey of arrival and capture conditions. This capability for fast preliminary mission design is

demonstrated by comparing two capture options at Europa. First is a 200 km altitude, 95° inclination circular orbit representative of tight capture planetary moon science orbit designs [55, 72]. The remaining osculating Keplerian orbital elements of longitude of the ascending node, Ω, and the argument of latitude at epoch, $\omega + \nu$, are considered free variables. This freedom results in a variable final Jacobi constant. Considering all possible phasing pairs of $(\Omega, \omega + \nu)$ shows a small range of $3.0094828 \leq C_+ \leq 3.0095035$ for the capture. In order to calculate the minimum impulse for tight capture, the capture radius, r_2, is required. As the average semi-major axis of a tightly captured orbit will remain constant, the capture radius in Equation (3.6) is set to the target orbit's semi-major axis of 1760 km.

The second capture option is a loosely captured orbit. Reference [85] reveals an approximate limiting case of a maximum radius at 7000 km with inclinations near 70° for stable near-circular orbits at Europa; this capture option has a calculated Jacobi constant range of $3.0027272 \leq C_+ \leq 3.0030558$. The perturbed nature of the loose capture leads to rapidly varying radii relative to Europa, complicating the choice of capture radius. Utilizing the physical limit of Europa's mean radius for r_2 in Equation (3.6) ensures the analytical propulsive costs are indeed a lower bound for capture at Europa.

To consider a broad range of possible arrival conditions the initial values are from a high-energy arrival of $C_- = 2.990$ up to an effectively free arrival of $C_- = C_+$. Cases where $C_+ < C_-$ are not considered for this analysis, as the condition implies the initial orbit is already more tightly captured than the

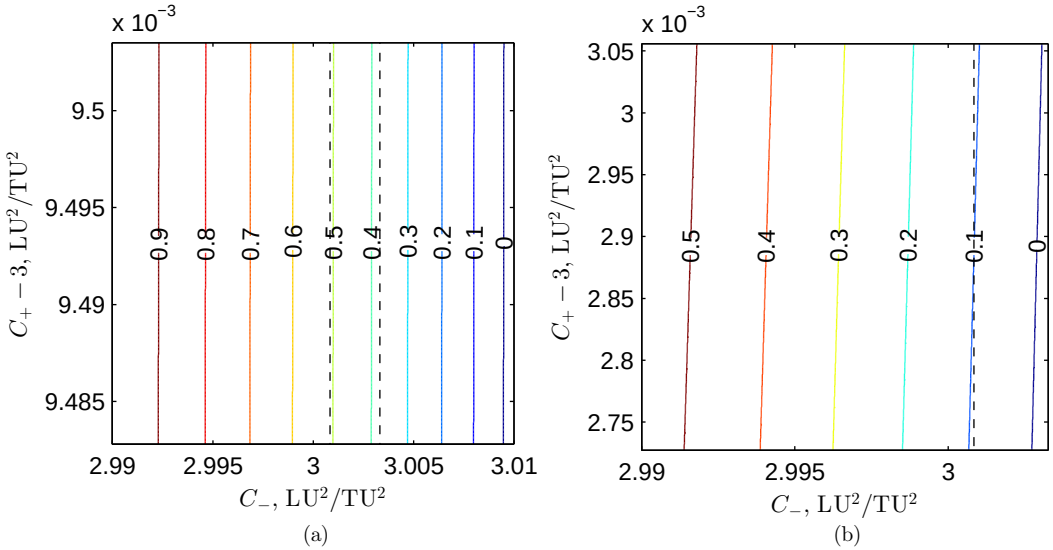

Figure 3.2: Contours of analytical minimum ΔV (km/s) over a range of energy levels for (a) Tight capture (b) Loose capture

final orbit. The range of C_- includes the L2 halo orbit family, which is between 3.0008370 and 3.0033259 at Europa [59]. Gridding over the boundary values for both capture cases results in the contours shown in Figure 3.2. Dashed lines show the Jacobi constant bounds of the L2 halo orbits, as that family is a likely candidate for the initial boundary orbit. Looking at tight capture, transfers within the L2 halo family bounds have floor ΔVs between 400 m/s and 500 m/s. Larger values of ΔC result in maneuvers up to 1 km/s for the considered range of Jacobi constants, although this maximum represents a high-energy arrival orbit prior to capture. In plot (b) of Figure 3.2 it is seen that loose captures have potentially free transfers from L2 halo orbits when $C_- = C_+$, although the existence of such transfers is not guaranteed. Comparing the

tight and loose capture options it is apparent that loose capture requires less ΔV for all arrival conditions, as expected.

3.1.3 Derivation in the Hill's Model

While Equation (3.6) can be rapidly evaluated, the results are system specific. In particular, the energy bounds of a given family of orbits vary between systems. This variation requires finding and continuing L2 halo orbit families for every system before the energetic minimum can be evaluated. To allow scaling both the bounds and the propulsive costs between three-body systems, the analysis is re-derived in the Hill's model. This model is the limiting case of the CRTBP as μ goes to zero, eliminating the body-specific mass ratio from the equations of motion while preserving the essential dynamics near the secondary [97]. Note that the model uses a rotating frame centered at the secondary, rather than the system barycenter. Normalized length units are defined such that LU $= (GM_2/N^2)^{1/3}$, where N is the dimensional angular velocity of the secondary. The normalized time remains unchanged from the CRTBP. As the minimum ΔV equations do not require physical orbits, the Hill's model equations of motion can be ignored for this work; the pertinent development is a modification in the motion integral from C to Γ [86]:

$$\Gamma = 3x^2 - z^2 + \frac{2}{r_2} - V^2 \tag{3.7}$$

Table 3.1: Hill's model analytical floor ΔV range for tight and loose capture orbits from the L2 halo orbit family at moons of interest

Secondary	$\boldsymbol{R_m}$, **km**	**Length Unit, km**	**Time Unit, s**	**Tight Capture** $\boldsymbol{r_2}$, **LU**	$\boldsymbol{h}$, **km**	$\boldsymbol{\Delta V}$, **m/s**	**Loose Capture Max** $\boldsymbol{\Delta V}$, **m/s**
Moon	1738	88,454.7	104.36	0.022	200.0	609–642	27.8
Phobos	11	23.1	1.22	0.693	—	—	4.13
Deimos	6	33.8	4.82	0.325	—	—	0.77
Io	1815	15,196.3	6.76	0.133	200.0	353–597	194
Europa	1561	19,696.11	13.57	0.089	200.0	378–501	99.3
Ganymede	2631	45,733.4	27.33	0.062	200.0	602–717	96.1
Callisto	2400	72,283.6	63.75	0.036	200.0	601–659	48.7
Amalthea	98	282.7	1.90	0.391	—	—	25.8
Himalia	93	19,592.3	957.09	0.005	11.9	31.6–32.0	0.33
Elara	38	8645.0	991.80	0.005	5.00	14.0–14.1	0.13
Pasiphae	25	10,897.8	2807.49	0.003	5.00	8.43–8.49	0.04
Sinope	18	8196.2	2895.35	0.003	5.00	6.12–6.16	0.03
Lysithea	81	4,008.2	990.15	0.023	10.4	2.85–3.02	0.13
Carme	20	8308.9	2643.25	0.003	5.00	6.53–6.58	0.04
Ananke	15	5,756.7	2,410.24	0.003	5.00	4.62–4.66	0.03
Leda	8	1,600.0	911.84	0.008	5.00	2.18–2.22	0.03
Thebe	50	163.4	2.58	0.345	—	—	10.0
Adrastea	10	27.7	1.14	0.542	—	—	4.34
Metis	20	47.0	1.13	0.532	—	—	8.38
Mimas	196	798.8	3.60	0.277	—	—	30.1
Enceladus	250	1205.2	5.23	0.234	32.0	2.01–39.7	28.0
Tehtys	530	3215.0	7.21	0.186	67.9	31.4–92.6	46.7
Dione	560	4632.3	10.45	0.136	71.8	66.6–116	38.6
Rhea	765	8636.0	17.26	0.100	98.0	115–160	36.4
Titan	2575	75,714.8	60.91	0.047	1000.0	548–622	64.2
Hyperion	148	4601.2	81.27	0.036	19.0	29.8–32.8	2.39
Lapetus	730	53,010.4	303.02	0.016	93.5	153–159	4.78
Phoebe	110	11,501.6	2102.68	0.011	14.1	5.83–5.99	0.12
Ariel	579	4766.7	9.63	0.137	74.2	73.5–128	43.2
Umbriel	586	6328.1	15.83	0.104	75.1	87.2–125	29.8
Titania	790	14,982.5	33.25	0.059	101.2	167–198	24.7
Oberon	762	19,014.2	51.43	0.045	97.6	168–189	17.5
Miranda	240	1204.4	5.40	0.225	30.8	4.33–39.7	26.3
Triton	1353	21,075.1	22.45	0.072	173.4	296–367	57.2
Nereid	170	32,280.8	1375.62	0.006	21.8	34.3–34.8	0.39
Charon	593	11,931.7	24.40	0.056	76.0	190–222	26.0

By simple inspection it is apparent that Γ has the same sensitivity to velocity as the Jacobi constant, and so the floor ΔV remains dependent on the location of maximum velocity.

As the dynamics of the three-body system are preserved near the secondary in the Hill's model, the location of the maximum velocity remains along the x-axis. Equation (3.7) is solved for velocity and evaluated at this

maximum location. Taking the difference in the velocities at both boundary conditions gives the analytical minimum ΔV in the Hill's model. The results can be scaled to any three-body system using the discussed scaling parameters, included in Table 3.1 for multiple planetary moons [95]:

$$\begin{aligned} \Delta V &= \left| \sqrt{B - \Gamma_+} - \sqrt{B - \Gamma_-} \right| \\ B &= 3r_2^2 + 2/r_2 \end{aligned} \tag{3.8}$$

Calculating the floor ΔV for the two capture options requires converting the boundary conditions to the Hill's model. For loose capture the Γ_+ values remain between $3.2835761 \leq \Gamma_+ \leq 3.6625036$ for all planet-moon systems. However, the minimum capture radius in Equation (3.8) varies as $r_2 = R_\mathrm{m}$, where R_m is the mean radius of the planetary moon. Conversely, the tight capture orbits are completely defined relative to the secondary, making both r_2 and the range of Γ_+ system specific. For this work, tight captures are defined to have altitude $h = \max\left(5, \min\left(0.1281 R_\mathrm{m}, 200\right)\right)$ km. The capture radius then is defined as $r_2 = R_\mathrm{m} + h$. This definition is a heuristic based on the 200 km tight capture at Europa used in this dissertation; it scales the altitude for bodies smaller than Europa, while maintaining a maximum limit of 200 km altitude. An absolute minimum altitude of 5 km is enforced. Titan is an exception, which uses a 1000 km altitude for both capture options to account for the moon's thick atmosphere. Tight capture orbits with r_2 greater than 0.2667 LU in the Hills' model are considered to be dynamically at loose capture, hence no tight capture ΔVs are calculated. The motion integral for

L2 halo orbits ranges from $\Gamma_- = 1.3130857$ to 4.0053035 for all bodies.

The analytical floor capture costs are calculated for numerous moons of interest, shown in Table 3.1. Note that the minimum for loose capture is always zero as the motion integral ranges for the L2 family and capture orbits overlap. Comparing the ΔVs at Europa to the results in Figure 3.2 shows reasonable agreement between the CRTBP and Hill's model approaches, verifying the scalability of the results. The Hill's approach shows a range of 378–501 m/s, while Figure 3.2 from the CRTBP approach shows values of approximately 390–500 m/s between the L2 halo bounds indicated by dashed lines. A majority of the large moons of interest, such as the Galilean moons or Titan, all require tight captures on the order of hundreds of meters per second. Smaller moons such as Enceladus require tens of meters per second, while the smallest bodies require as little as 3 m/s for tight capture. Note that tight captures at several small moons near their primary, such as Enceladus or Miranda, have significant variation in the theoretical floor ΔV. This variation is due to the normalized capture radii approaching the defined dynamical limit of tight capture. Near this limit the phasing at capture significantly alters Γ_+, and thus the maneuver cost. For these bodies, capturing at the optimal phase angle saves on the order of tens of meters per second.

For all moons, loose capture enables a reduction in ΔV, up to the extreme case of free transfers from the L2 halo orbit family. Reductions on the order of a magnitude over tight capture are typical for large moons such as Ganymede and Europa, as well as for small bodies far from their primary such

as Pasiphae. Relatively small moons near their primary show the smallest reduction, with several bodies having tight captures cheaper than the most expensive loose captures. As discussed, tight captures at these moons approach the defined radius limit where the orbit transitions to loose capture, resulting in dynamically similar orbits with overlapping energy levels.

3.2 Generating Feasible Bi-Impulsive Capture Trajectories

The work now proceeds to search for physical capture trajectories with ΔV costs in the vicinity of the energetic lower bound. The focus remains on transfers from the L2 halo family to both tight and loose captures at Europa. Two systematic near-global grid search methods are utilized to find impulsive transfers. The searches are developed specifically for each capture option due to their differing dynamical behaviors and boundary constraints. The resulting propulsive costs are compared to the analytical minimum to verify the analytical equations and assess the idealness of the captures.

3.2.1 Tight Capture

For tight capture, the grid search is developed using a two-impulse assumption: an initial impulse to depart the boundary halo orbit, with the terminal capture impulse applied at an apse relative to the secondary. Note that this approach does not use the assumed ideal of an unstable manifold departure from the halo orbit. While the departure impulse was not included in

the single-impulse assumption, the maneuver allows an extra degree of freedom in the search and is relatively small for near-ideal transfers. In ideal cases the maneuver is trivially small, representing catalysts to precipitate a transfer along an unstable manifold.

The assumptions on the transfer reduce the problem to two variables: the location of the departure impulse on the halo, τ, and the magnitude of the departure impulse, ΔV_{D}. The impulse is defined with positive and negative values to indicate maneuvers in the same or opposite direction of the orbit velocity, respectively. The parameter τ is defined as the normalized arclength distance along the initial orbit. This parameter is calculated by integrating a new equation along with the CRTBP equations of motion to get the total distance traveled over one period, $\tilde{\tau}_{\mathrm{P}}$:

$$\dot{\tilde{\tau}} = \left(u^2 + v^2 + w^2\right)^{1/2} \tag{3.9}$$

The total length is then normalized to $\tau = \tilde{\tau}/\tilde{\tau}_{\mathrm{P}}$ such that $0 \leq \tau \leq 1$. The equations of motion become a function of τ using a variable transformation:

$$\frac{d\mathbf{X}}{d\tau} = \frac{\tilde{\tau}_{\mathrm{P}}}{\dot{\tilde{\tau}}}\dot{\mathbf{X}} \tag{3.10}$$

Note that the non-normalized total arc length must be calculated before using Equation (3.10) for the periodic orbit to have a period of $\tau = 1$. The equation results in the three-body equivalent of a Sundman transformation. Due to this

transformation, constant step sizes in τ guarantee equally spaced points along any orbit.

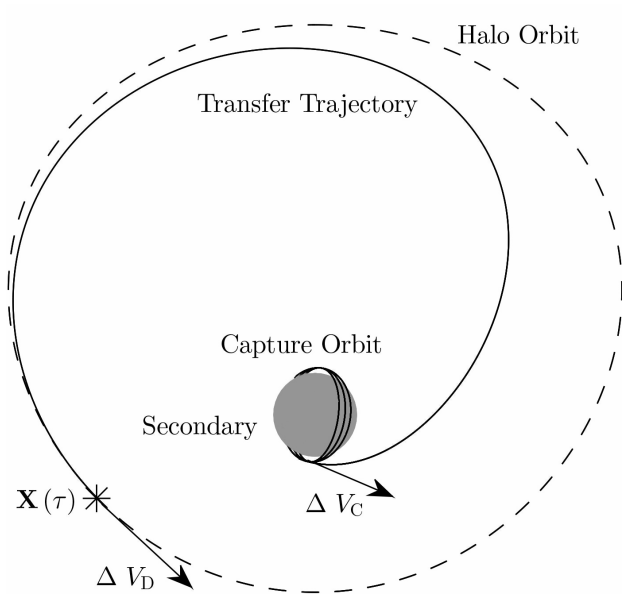

Figure 3.3: Diagram of nominal transfer trajectory, showing the departure location $\mathbf{X}(\tau)$, departure impulse ΔV_{D}, and orbit capture impulse ΔV_{C} applied at an apse relative to the secondary

The grid of τ and ΔV_{D} leads to unique pairs of departure conditions. The corresponding initial states are propagated forward in time using a variable step Runge-Kutta 7(8) integration scheme. As the flight time to capture is unknown, the propagation ends with either impact or departure from the planetary moon. For this work departure is defined as r_2 exceeding five times the Hill radius, defined in Chapter 2. Each trajectory has several apsides relative to the secondary determined by $\dot{r}_2 = 0$. The capture is applied at the apse closest to the target capture orbit altitude. At this location, the two-body os-

culating orbital elements are calculated, along with the capture impulse ΔV_{C} required to match the target eccentricity. Figure 3.3 shows an example transfer trajectory using the developed approach, including the departure location as a function of τ.

The grid search results in near-global knowledge of feasible two-impulse transfer trajectories, as well as their resultant capture cost and initial osculating orbital elements. A combined objective function of semi-major axis and inclination quantifies how well the transfers meet the target conditions (recalling that the eccentricity is already explicitly enforced):

$$F = \left(\frac{a^* - a}{a_{\mathrm{scale}}}\right)^2 + \left(\frac{i^* - i}{i_{\mathrm{scale}}}\right)^2 \tag{3.11}$$

The star superscript indicates the target values, and the scaling parameters are used to weight the two elements. Choice of the scales is based on making F equally sensitive to changes in semi-major axis and inclination; values of 100 km and 1.4 degrees were used in this work. The minimum values of F are used to identify grid points where the transfers closely approach the desired science orbit, with an optimal value of zero.

The n best points are chosen for further improvement via differential correction. A Newton corrector iterates τ and ΔV_{D} using a step direction calculated as:

$$\begin{bmatrix} \Delta\tau \\ \Delta\left(\Delta V_{\mathrm{D}}\right) \end{bmatrix} = -\begin{bmatrix} \partial a/\partial\tau & \partial a/\partial\Delta V_{\mathrm{D}} \\ \partial i/\partial\tau & \partial i/\partial\Delta V_{\mathrm{D}} \end{bmatrix}^{-1} \begin{bmatrix} a^* - a \\ i^* - i \end{bmatrix} \tag{3.12}$$

The partial derivatives are approximated using the complex step finite difference method [64]. Solutions are considered converged if the semi-major axis and inclination are met to within 100 m and 0.5 degrees, respectively. Figure 3.4 summarizes the algorithm used to find tight capture solutions.

```
FOR τ = 0 to 1 by dτ
   Propagate halo orbit forward in τ to X(τ)
      FOR ΔV_D = ΔV_D,min to ΔV_D,max by dΔV_D
         Apply ΔV_D to X(τ), store updated initial transfer state X_T,0
         Propagate X_T,0 forward in t until impact or departure
         Interpolate and store time and state of apsides along trajectory
         Set X_C,0 and T_T to state and transfer time at apse closest to target capture radius
         Evaluate osculating orbital elements of X_C,0 relative to Europa
         Calculate ΔV_C to target capture orbit eccentricity
         Store τ, ΔV_D, ΔV_C, T_T, and capture orbit osculating orbital elements
      END ΔV_1 loop
END τ loop
Evaluate F for all grid points, identify n lowest captures
FOR i = 1 to n
   Differentially correct τ, ΔV_D to reduce F
   IF [improved solution meets tolerances]
      Record τ, ΔV_D, ΔV_C, T_T, and capture orbit osculating orbital elements as solutions
END i loop
```

Figure 3.4: Tight capture grid search algorithm

Transfers to the target 200 km altitude, 95° inclination tight capture orbit are found through the full range of the L2 halo family. To avoid multiple runs of the time-consuming grid search (using the algorithm in Figure 3.4), new transfers from neighboring halo orbits are found using continuation methods, leading to families of transfer trajectories. To start the continuation, the initial orbit Jacobi constant is varied by a small perturbation to a different, precomputed L2 halo orbit. The differential corrector in Equation (3.12) then searches for a transfer from this halo orbit using solutions from the previous halo orbit as initial guesses. Once transfers are found for two halo orbits,

further initial guesses of τ and ΔV_{D} are found by polynomial extrapolation as a function of C_{-}. Occasionally the full grid search is repeated to reinitialize the continuation and find additional transfer orbits.

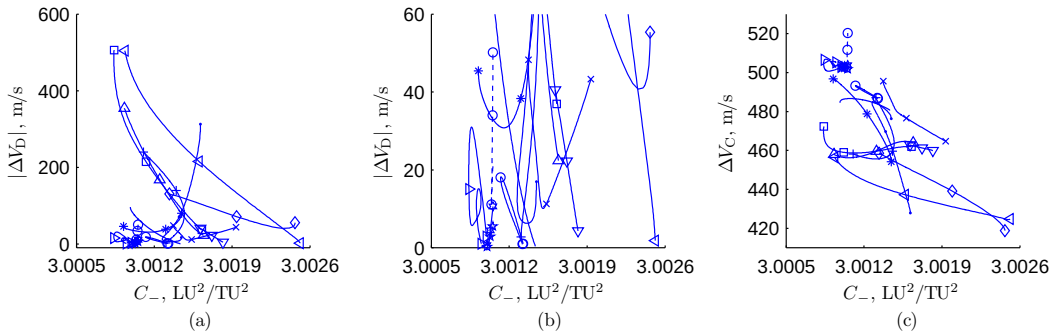

Figure 3.5: Tight capture costs for: a) Depart impulse b) Zoom view of departure c) Capture impulse

For this initial study, 16 unique transfer families are identified consisting of 3821 transfers. The evolution of the transfer ΔVs are shown in Figure 3.5. From plots (a) and (b) it is seen that in general there is no overall trend for the departure maneuver, indicating it has little correlation with C_{-}. Conversely, the capture impulse in Figure 3.5(c) shows an apparent correlation to C_{-}: as the Jacobi constant increases, the majority of the families decrease in ΔV_{C}, consistent with the analytical results. Also of note is the limited range in the values of ΔV_{C}, all the families remain within 420–520 m/s, with most families varying by less than 50 m/s throughout the entire range of Jacobi constant. This consistency indicates that even large differences in departure maneuver can have little impact on the required capture cost.

The total ΔV for the transfers are given in Figure 3.6, with lines of

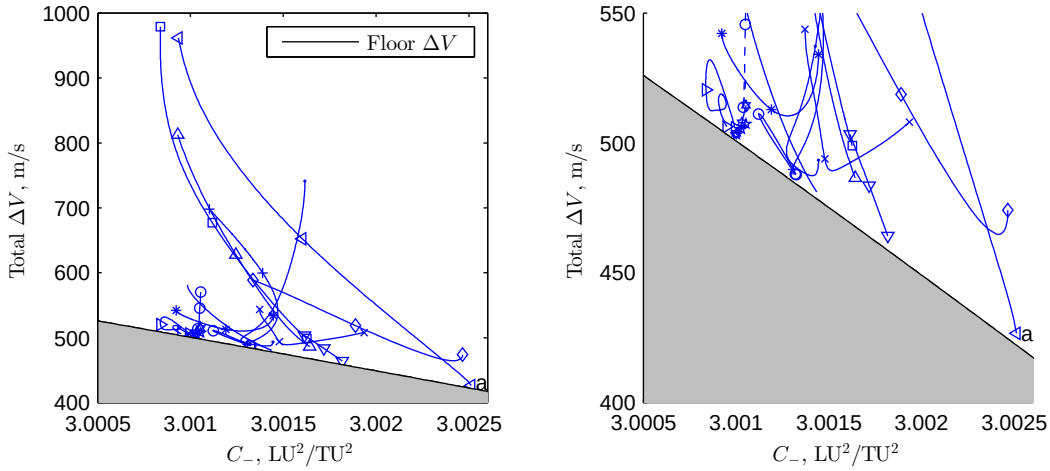

Figure 3.6: Total ΔV for tight capture transfer families, including detail view near analytical floor. Shading indicates region below minimum

maximum and minimum floor cost (corresponding to the minimum and maximum C_+) included for comparison. As the range of $C+$ is small there is negligible difference between the two floor values, resulting in an apparent single line. The area below the lines is grayed out as it is inaccessible based on the analytical theory. It is clear from the plots that there are no computed solutions below the floor, although several families closely approach the limit. As discussed, the use of the unstable L2 halo orbit family permits effectively free departure on manifold-like trajectories, some of which are likely to intersect the desired science orbit tangentially with near-ideal capture cost. In general, the near-minimum solutions found can be replaced with these manifold transfers at the expense of additional flight time.

The lowest total ΔV solution from the search occurs at $\tau = 0.3999$, $\Delta V_{\mathrm{D}} = -1.85$ m/s with a total velocity change of 426.7 m/s. Plots of the

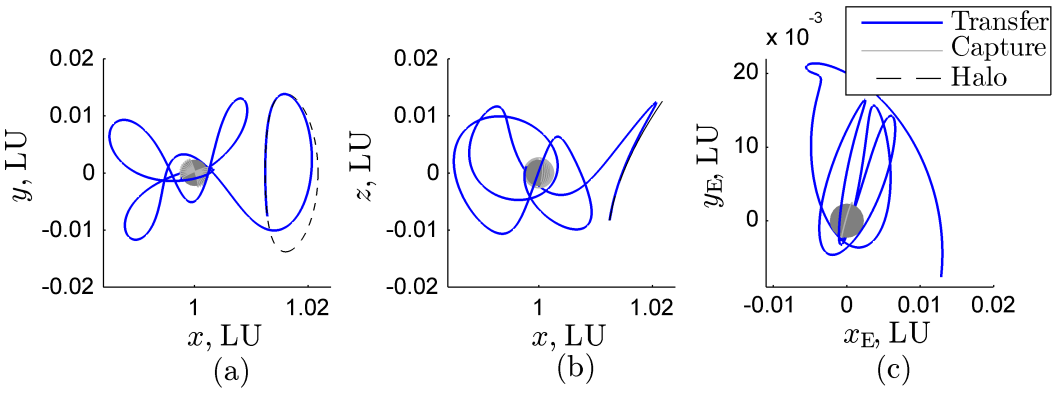

Figure 3.7: Minimum ΔV transfer trajectory (point a in Figure 3.6) and tight capture orbit in (a,b) The rotating frame (c) The Europa-centered inertial frame

transfer and capture are given in Figure 3.7. A relatively small magnitude departure impulse results in a manifold-like transfer that follows the initial halo orbit before falling off towards Europa. The non-rotating plot shows how the three-body dynamics "twist" the transfer trajectory such that the spacecraft arrives at Europa with the desired target inclination at the correct capture altitude.

3.2.2 Loose Capture

Loose capture orbits are strongly perturbed by Jupiter, resulting in rapid variation of the osculating orbital elements. Targeting specific orbital elements is therefore not useful, and a different approach is required. The constraint of targeting a specific orbit is reduced to simply matching the expected range of Jacobi constant for loose captures. To fully survey this range the

capture maneuver ΔV_{C} becomes a grid variable, with the bounds calculated from the loose capture range of C_{+}:

$$\Delta V_{\mathrm{C}} = \left(V_{-}^{2} + C_{-} - C_{+}\right)^{1/2} - V_{-} \tag{3.13}$$

The departure impulse grid is eliminated and replaced with unstable manifold transfers, generated over the grid of departure location τ. To expand the amount of solutions found, all apsides along the transfer are considered for capture (equivalent to an apse Poincaré map) leading to a third grid over each apse. A summary of the grid search is given in Figure 3.8.

```
FOR τ = 0 to 1 by dτ
   Propagate halo orbit forward in τ to X(τ)
   FOR s = −1,1 (sign of perturbation)
      Perturb X(τ) to get manifold transfer initial state X_T,0
      Propagate manifold forward in t until impact or departure
      Interpolate and store time t_i and state X_T(t_i) at all N apsides along manifold
      FOR i = 1 to N
         Set capture initial state X_C,0 to X_T(t_i)
         Evaluate ΔV_C,min and ΔV_C,max from C_+,min and C_+,max
         FOR ΔV_C = ΔV_C,min to ΔV_C,max by dΔv
            Apply ΔV_C to X_C,0
            Propagate X_C,0 forward in t by 90 days
            IF [no impact or departure within 45 days]
               Store τ, s, transfer time T_T = t_i, ΔV_C, and X_C,0 as solutions
               Return to i loop
         END ΔV loop
      END i loop
   END s loop
END τ loop
```

Figure 3.8: Loose capture grid search algorithm

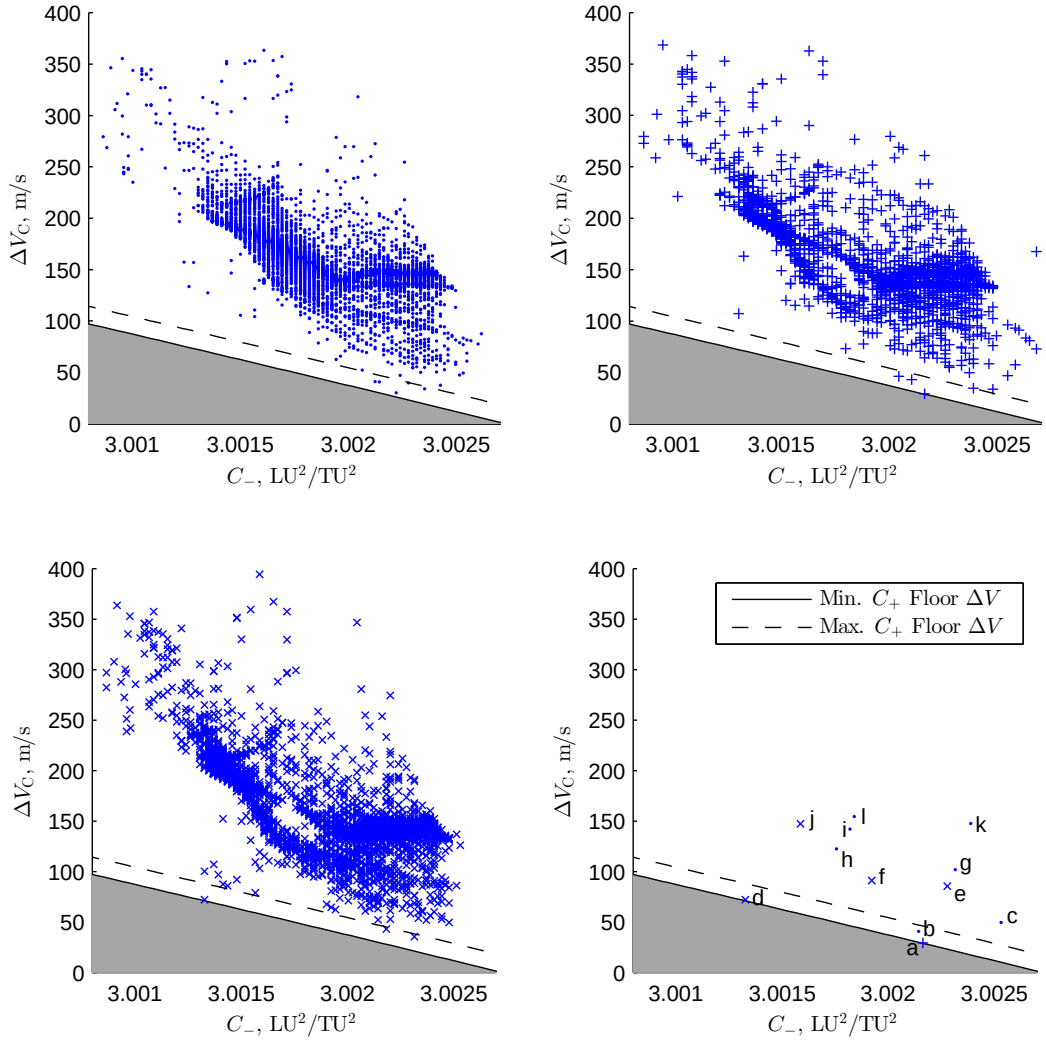

Figure 3.9: Impulse cost for loose captures from L2 halos with inaccessible shaded region. Captures remain bound (dot), depart (plus), or impact (x) within 90 days. Labels correspond to orbits in Figure 3.10

The grid search is run using a 100×100 grid of τ and ΔV_{C}. Unstable manifolds are generated using Equation (2.3) with perturbation size $\epsilon = \pm 10^{-6}$. All capture trajectories are integrated forward by 90 days to ver-

ify long lifetime orbits. Trajectories that impact or depart Europa within 45 days are discarded. In order to save computer memory and runtime, the ΔV_{C} grid stops after the first long lifetime capture is found. This approach ensures that the capture found has the smallest impulse for a given apse. The grid capture search is applied to multiple halo orbits spanning the entire range of the L2 halo family to ensure a thorough search of the available design space. The resulting manifold transfers and capture trajectories are fully parameterized by halo orbit Jacobi constant C_{-}, depart location τ, manifold perturbation sign, transfer time to capture T_{T}, and maneuver ΔV_{C}.

A total of 19,604 captures were found with a lifetime greater than 45 days. Figure 3.9 plots the total ΔV_{C} of the captures as a function of the initial L2 halo Jacobi constant. Lines of the analytical minimum for both the maximum and minimum C_{+} values are included. Unlike the tight capture case, the range of capture Jacobi constant is relatively broad, resulting in a difference of approximately 17 m/s between the lines. Trajectories that closely follow the ideal capture case are between these bounds. The dark gray region indicates values that are inaccessible. Captures are further classified based on their lifetime behavior within 90 days: bound to the secondary, departure, or impact.

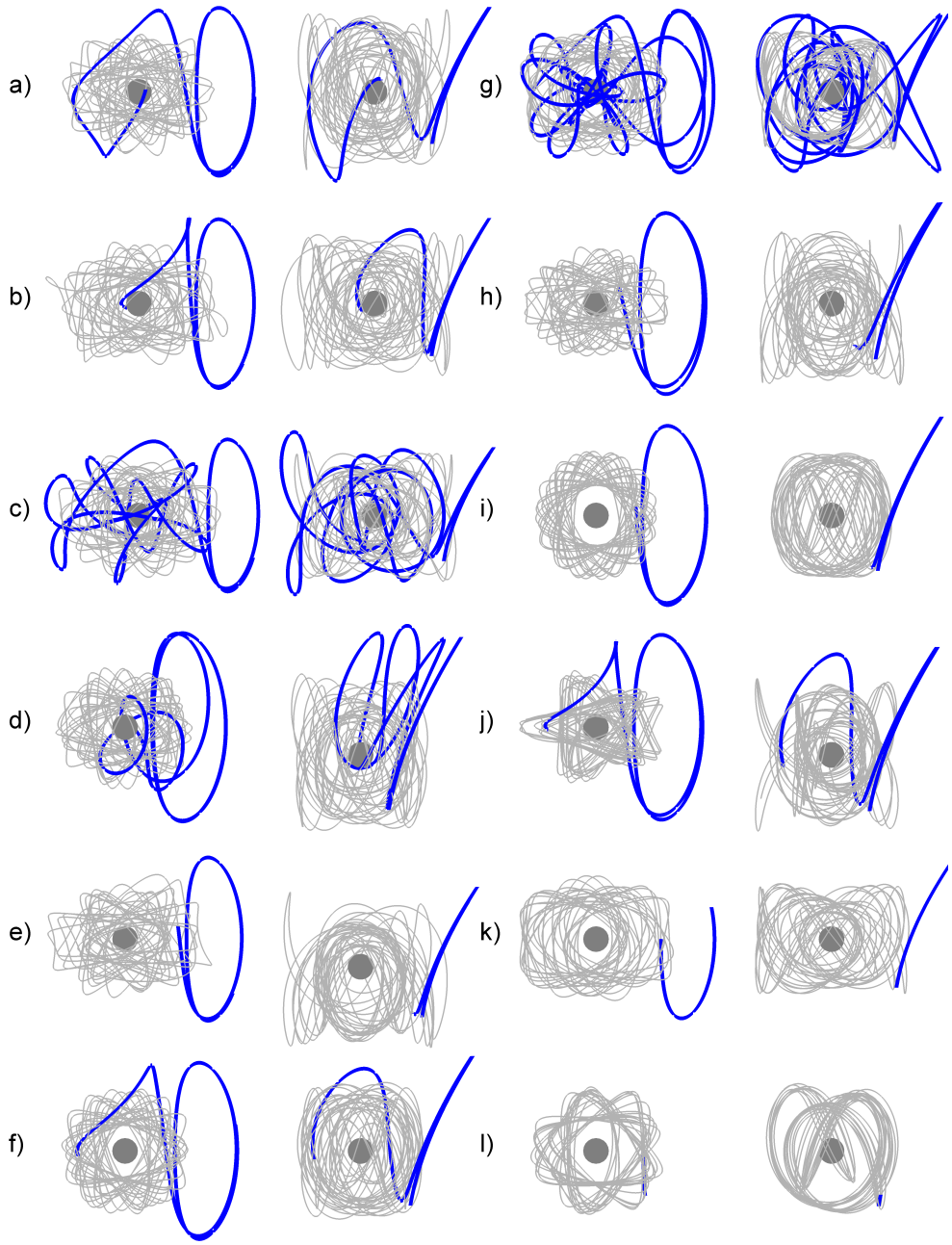

Figure 3.10: Example manifold trajectories (thick) leading to an apse collinear insertion maneuver and capture orbits (thin) that remain bound to Europa for at least 45 days. Each solution has xy-plane and xz-plane projections

Table 3.2: Transfer trajectory parameters for example captures, including capture radius and expected capture lifetime

Case	τ	C_-, $\mathrm{LU^2/TU^2}$	C_+, $\mathrm{LU^2/TU^2}$	T_T, day	ΔV_C, m/s	ΔV_min, m/s	r_2, km	Lifetime, day
a)	0.01010	3.0021634	3.0027306	4.184	29.19	29.12	1661	78.7
b)	0.13131	3.0021439	3.0028920	3.221	40.65	38.49	1825	90.0+
c)	0.10101	3.0025316	3.0030558	8.330	49.48	27.18	4130	90.0+
d)	0.94949	3.0013279	3.0027273	5.675	72.00	71.03	1699	74.1
e)	0.12121	3.0022785	3.0027554	2.367	85.41	24.53	8713	50.1
f)	0.94949	3.0019234	3.0027273	3.527	91.04	41.14	5743	53.1
g)	0.60606	3.0023160	3.0029511	10.54	101.7	32.78	8041	90.0+
h)	0.63636	3.0017574	3.0027577	3.133	122.5	51.09	6133	90.0+
i)	0.97980	3.0018202	3.0027273	2.564	142.0	46.35	7968	90.0+
j)	0.51515	3.0015876	3.0028609	4.246	147.5	64.98	6006	48.1
k)	0.92929	3.0023898	3.0030470	0.994	147.8	34.00	9847	90.0+
l)	0.41414	3.0018410	3.0027273	0.109	154.5	45.31	8811	90.0+

Figure 3.9 illustrates that only a few of the found captures approach the analytical floor. The sparsity of solutions is largely due to the use of the minimum 45-day lifetime limit. Reducing this constraint would yield more results; however investigating changes to this limit is not within the scope of this work. All the captures are less expensive than the tight captures seen in Figure 3.6, typically on the order of hundreds of meters per second. The case closest to the ideal floor, (a), requires 29.19 m/s for capture, slightly larger than the expected minimum value. Two other captures, (b) and (d), are similarly near-ideal at 40.65 and 72.00 m/s respectively. In total, 569 captures are found with costs less than 100 m/s, with 20 transfers below 50 m/s.

A collection of example capture orbits propagated for 30 days are plotted in Figure 3.10, with associated data in Table 3.2. The captures chosen represent the majority of general qualitative behaviors seen for both transfer and capture orbits. For example, transfers (c), (d), and (g) represent options

with total transfer times on the order of a week. These transfer manifolds exhibit multiple low and high-altitude apsides of Europa before final capture. As stated, case (a) shows the lowest ΔV capture. The low cost is primarily due to the efficient capture radius of 1661 km. Two other near-ideal captures (b) and (d) have similarly small capture radii. Several captures such as (d), (e), and (h), resemble the "ball-of-yarn" orbits found in Reference [86]. These orbits provide a wide range of viewing geometries and varying locations of periapse but are dynamically chaotic. If a more predictable orbit is desired, captures (i), (j), and (l) represent near-periodic orbits that could potentially be driven to periodicity with minor targeting adjustments.

Comparison of the actual and analytical impulse costs in Table 3.2 matches expectations: all captures are above the energetic floor. In addition, the idealness of the solution can be determined by its distance from the floor. Captures that occur with r_2 close to the physical radius limit of 1560 km, such as case (a), (b), and (d), are within a few meters per second of the ideal values. As capture radius is increased the solutions diverge from ideal. Solution (c) is particularly notable: it has the third lowest ΔV of the solutions listed, which initially indicates that it may be a near-ideal solution. However, comparison to the energetic floor shows that the impulse cost can be nearly halved if a lower capture radius can be found. Solution (k), with the largest listed capture radius, is furthest from ideal. Assuming a lower radius impulse location can be found, it is possible to save over 100 m/s.

3.3 Conclusions

The problem of transferring from the L2 halo family to two types of capture orbits is addressed. Equations for an energetic minimum on the ΔV in the CRTBP are derived, allowing rapid analysis of the expected propulsive costs without the need for generating physical transfers. Notably, the new equation is general in nature and can be applied to any transfer constrained by energetic bounds. A similar derivation in the Hill's model removes system dependency from the equation, enabling scaling of the results (assuming the energy bounds are constant between systems). While this consistency is not true for the capture orbit energy, it holds for the L2 halo orbits, eliminating the need to generate a periodic orbit family for every planet-moon system. Due to this scalability, a survey of capture costs for most planetary moons of interest is rapidly generated using the Hill's model equation. Comparing costs of the capture options shows that loose captures can save up to an order of magnitude in ΔV over traditional tight captures.

The analytical results are confirmed with physical transfers to Europa capture. Systematic grid searches are presented to find transfers for each capture option. In the tight capture case, application of the continuation method leads to multiple transfer families connecting orbits in the L2 halo family at Europa to a specified science orbit state. While a departure impulse is allowed, the lowest ΔV transfers closely follow the ideal transfer assumptions of a manifold-like departure with a single, tangential capture impulse. Due to less restrictive capture constraints a wide variety of loose captures are found,

allowing some flexibility in the choice of capture orbit. General classes of orbit are highlighted from a mission design perspective, including circulating eccentricity "ball-of-yarn" orbits and less chaotic near-periodic orbits. The numerical results confirm that loose captures can significantly reduce propulsive costs over tight capture, up to an order of magnitude. This cost reduction over tight capture, coupled with long lifetimes and access to multiple viewing geometries, indicates that loose captures can enable single orbiter, multi-moon missions.

Chapter 4

Primer Vector Optimization

In this chapter the problem of optimizing highly-sensitive transfer trajectories is investigated. The initial contributions are algorithm developments to mitigate or otherwise account for the extreme sensitivity encountered when using long, multi-revolution orbits with chaotic dynamics. As part of this work, a specialized nonlinear programming optimizer is written to account for convergence difficulties due to the sensitivity; a pseudcode is provided in Appendix A. Primer vector theory is then extended to include the removal of impulses that converge towards zero magnitude, eliminating singularities. A new family of three-dimensional periodic orbits is generated that enables efficient connection of resonant and halo orbits. Optimization of several different transfers leads to new insights on the utility of the primer vector in determining the proximity of an initial guess to an optimal solution.

4.1 Problem Definition

The problem posed is to find the minimum ΔV, time-free, impulsive transfer that connects two boundary orbits:

$$\Gamma\left(t_i, \mathbf{r}_i\right) = \sum_{i=0}^{\mathrm{N}} \Delta V_i \tag{4.1}$$

where there are N + 1 impulsive maneuvers, with the number determined during optimization. Note that the impulses are not controlled directly, but are instead implicit functions of the times and positions of the maneuvers, t_i and $\mathbf{r}_i$, respectively. There are three conditions which impose limits on the trajectory, leading to constraints:

1) The trajectory is continuous in position

2) The positions of the trajectory at the initial and final times must be on their respective boundary orbits

3) The trajectory must not impact Jupiter or Europa

The first condition is predominately satisfied implicitly by integrating the equations of motion between impulses. However, at each impulse the continuity condition leads to an equality constraint, which is satisfied using a forward-shooting algorithm presented later in this chapter. The boundary orbit constraints are trivially satisfied by explicitly setting the first and last maneuvers to be within their receptive orbits, with the position determined via cubic spline functions. The last condition results in two inequality constraints, which are handled using an event function on the trajectory to stop integration when impacts occur.

4.1.1 Impulsive Primer Vector Theory

The Hamiltonian of the system, H, is introduced to augment the optimization problem:

$$H = \boldsymbol{\lambda}_{\mathrm{r}}^{\mathrm{T}}\mathbf{v} + \boldsymbol{\lambda}_{\mathrm{v}}^{\mathrm{T}}\ddot{\mathbf{r}} \tag{4.2}$$

where $\boldsymbol{\lambda}_{\mathrm{r}}$ and $\boldsymbol{\lambda}_{\mathrm{v}}$ are 3×1 vector Lagrange multipliers that include the equations of motion as differential constraints in the augmented optimization problem. Specifically, $\boldsymbol{\lambda}_{\mathrm{v}}$ is known as the primer vector, hereafter represented as $\mathbf{p}$ (following Prussing's notation) [79]. Using calculus of variations, several conditions for the local optimum of a time-free trajectory are obtained:

$$||\mathbf{p}(t)|| \leq 1 \tag{4.3}$$

$$\mathbf{p}(t_i) = \frac{\Delta\mathbf{V}_i}{\Delta V_i} \tag{4.4}$$

$$\dot{p}(t_i) = 0 \tag{4.5}$$

where $\Delta\mathbf{V}_i$ is the ith impulse vector, t_i is the time at each impulse, and $\dot{p}$ is the time derivative of the primer vector magnitude [26, 60]. Equation (4.5) must always hold for intermediate impulses, however it only applies to the initial and final maneuvers for time-free optimal departures and arrivals. In addition to these necessary conditions, the primer vector and its time derivative must be continuous everywhere, including across impulses.

The full time histories of the primer vector and its time derivative are required to evaluate whether a trajectory is optimal. Noting that the primer vector equations of motion are identical to the variational equations of motion, i.e. Equation (2.4), the state transition matrix is used to propagate $\mathbf{p}$ and $\dot{\mathbf{p}}$ for each leg:

$$\mathbf{p}(t) = \mathbf{A}(t)\mathbf{p}_i + \mathbf{B}(t)\dot{\mathbf{p}}_i \tag{4.6}$$

$$\dot{\mathbf{p}}(t) = \mathbf{C}(t)\mathbf{p}_i + \mathbf{D}(t)\dot{\mathbf{p}}_i \tag{4.7}$$

where $\mathbf{A}(t)$, $\mathbf{B}(t)$, etc. are the submatrices of the state transition matrix $\mathbf{\Phi}(t, t_i)$, and $\mathbf{p}_i$ and $\dot{\mathbf{p}}_i$ are evaluated at time t_i. At each impulse, Equation (4.4) is explicitly enforced, providing known boundary conditions $\mathbf{p}_i$ and $\mathbf{p}_{i+1}$ between two successive impulses. Rearranging Equation (4.7) solves for the initial time derivative vector:

$$\dot{\mathbf{p}}_i = \mathbf{B}_i^{-1}[\mathbf{p}_{i+1} - \mathbf{A}_i\mathbf{p}_i] \tag{4.8}$$

The subscripts on $\mathbf{A}_i$ and $\mathbf{B}_i$ denote the mapping is from t_i to the time of the next impulse (typically t_{i+1}). Note that Equations (4.6) – (4.8) must be evaluated only between successive impulses, as the primer vector time derivative may not be continuous across a maneuver.

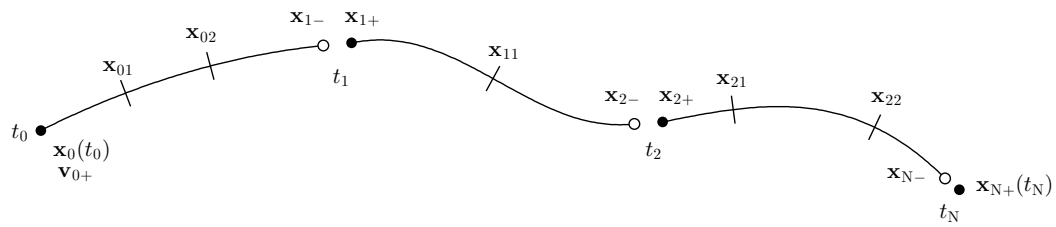

Figure 4.1: Example forward-shooting trajectory with leg nodes $\mathbf{x}_i$ at times t_i, and segment nodes at $\mathbf{x}_{ij}$. Velocity $\mathbf{v}_{0+}$ is independent of t_0

4.1.2 Multiple Forward-Shooting

The position continuity constraints of the trajectory are explicitly enforced using a multiple forward-shooting algorithm. Given an initial guess trajectory, the transfer is divided into multiple legs bounded by nodes located at impulses in the initial guess. Figure 4.1 depicts a notional four-impulse trajectory, consisting of three legs. Each leg node has two associated spacecraft states: $\mathbf{x}_{i+}$ and $\mathbf{x}_{i-}$. The plus state is the initial state of the leg starting at time t_i, and is generally independent of other variables. An exception is that the position at the first node and the full state at the final node are constrained to the originating and capture orbits, making these states functions of the departure and arrival times, respectively. The minus state, $\mathbf{x}_{i-}$, is the end state of a leg after integrating the previous node forward to time t_i. Note that the full 6-state of the first node, $\mathbf{x}_{0-}$ is also constrained to the originating boundary orbit as a function of the departure time. Plus and minus sign subscripts are used throughout this work to indicate whether a variable is at the start or end of a leg, respectively.

The chaotic dynamics of the CRTBP can lead to highly-sensitive trajectories that are difficult to differentially correct. These sensitivities are mitigated by further subdividing trajectory legs into n segments. Similar to the legs, each segment is bounded by nodes with states $\mathbf{x}_{ij+}$ and $\mathbf{x}_{ij-}$ at time t_{ij}, where subscript i indicates the leg and j denotes the segment node. The segments are initialized such that the maximum norm of the STM between nodes, $\|\mathbf{\Phi}(t_{ij}, t_{i(j-1)})\|_{\max}$, does not exceed 10^3, enforcing an upper limit on the sensitivity. Once initialized, the times of the segment nodes remain constant.

The dynamics of the problem require the constraints that a) the legs are continuous in position and b) the segments are continuous in position and velocity across their respective nodes. In the tradition of primer vector theory, these constraints are explicitly enforced by solving a boundary value subproblem of the optimization process. For a given leg, the discontinuities of the leg and segment nodes are combined into a single constraint vector, $\mathbf{g}_i(\mathbf{v}_{i+}, \mathbf{x}_{i1+}, \mathbf{x}_{i2+}, ..., \mathbf{x}_{ij+}, \mathbf{r}_{i+1,+}) = \mathbf{0}$, which is minimized via differential correction using the associated sparse Jacobian matrix $\mathbf{J}_i$:

$$\mathbf{J}_i = \begin{bmatrix} -\mathbf{\Phi}_{\mathbf{xv}}(t_{i1}, t_i) & \mathbf{I}_6 & & & \mathbf{0} \\ & -\mathbf{\Phi}(t_{i2}, t_{i1}) & \mathbf{I}_6 & & \\ & & -\mathbf{\Phi}(t_{i3}, t_{i2}) & & \\ & & & \ddots & \mathbf{I}_6 \\ \mathbf{0} & & & & -\mathbf{\Phi}_{\mathbf{rx}}(t_{(i+1)}, t_{i(n-1)}) \end{bmatrix} \tag{4.9}$$

where $\mathbf{\Phi}_{\mathbf{xv}}$ is the 6×3 submatrix of $\mathbf{\Phi}$ containing $\mathbf{B}$ and $\mathbf{D}$, and $\mathbf{\Phi}_{\mathbf{rx}}$ is the 3×6 submatrix consisting of $\mathbf{A}$ and $\mathbf{B}$.

4.1.3 Optimization Algorithm

Once the forward-shooting algorithm has enforced position continuity, the total cost of the trajectory expressed in Equation (4.1) is calculated by treating the velocity discontinuities as impulses, i.e. $\Delta V_i = ||\mathbf{v}_{i+} - \mathbf{v}_{i-}||$. The independent design variables that affect the cost are stored in a single-column vector, $\mathbf{k}$:

$$\mathbf{k} = \begin{bmatrix} t_0 & \mathbf{r}_{1+}^{\mathrm{T}} & t_1 & \mathbf{r}_{2+}^{\mathrm{T}} & t_2 & \ldots & \mathbf{r}_{\mathrm{N}+}^{\mathrm{T}} & t_{\mathrm{N}} \end{bmatrix}^{\mathrm{T}} \tag{4.10}$$

The gradient of the cost with respect to $\mathbf{k}$ can be expressed in terms of the primer vector and its time derivative [79]. For readability, the gradient is decomposed into its constituent derivatives:

$$\frac{d\Gamma}{dt_0} = -\dot{p}_0 \Delta V_0 \tag{4.11}$$

$$\frac{d\Gamma}{d\mathbf{r}_{i+}} = \dot{\mathbf{p}}_{i+}^{\mathrm{T}} - \dot{\mathbf{p}}_{i-}^{\mathrm{T}} \tag{4.12}$$

$$\frac{d\Gamma}{dt_i} = \dot{\mathbf{p}}_{i-}^{\mathrm{T}} \mathbf{v}_{i-} - \dot{\mathbf{p}}_{i+}^{\mathrm{T}} \mathbf{v}_{i+} \tag{4.13}$$

$$\frac{d\Gamma}{dt_{\mathrm{N}}} = -\dot{p}_{\mathrm{N}} \Delta V_{\mathrm{N}} \tag{4.14}$$

$$\nabla\Gamma = \begin{bmatrix} \frac{d\Gamma}{dt_0} & \frac{d\Gamma}{d\mathbf{r}_{1+}} & \frac{d\Gamma}{dt_1} & \frac{d\Gamma}{d\mathbf{r}_{2+}} & \frac{d\Gamma}{dt_2} & \ldots & \frac{d\Gamma}{d\mathbf{r}_{\mathrm{N}+}} & \frac{d\Gamma}{dt_{\mathrm{N}}} \end{bmatrix} \tag{4.15}$$

Note that these derivatives are specific to the time-free, bounding-orbit constrained problem, and assume continuity has been enforced by the forward-shooting inner-loop BVP.

The existence of a simple, analytical gradient naturally leads to the use of a gradient-based line search method to minimize the cost. Given a normalized search direction, $\mathbf{s}$, the variable vector $\mathbf{k}$ is updated as $\mathbf{k} = \mathbf{k} + \alpha\mathbf{s}$, where α is the value that minimizes the cost along $\mathbf{s}$, found using the golden-ratio line search technique. The direction of $\mathbf{s}$ strongly influences the total number of iterations needed to optimize the problem. In an effort to reduce the number of iterations required, the Broyden-Fletcher-Goldfarb-Shanno (BFGS) algorithm is utilized to generate the search direction [100]. This quasi-Newton method approximates the inverse of the shifted Hessian matrix, typically resulting in fewer optimization iterations than basic steepest descent algorithms. As the second-order update uses an approximation, the BFGS algorithm is reinitialized every twenty iterations, or when the search direction is uphill, i.e. $\mathbf{s}^{\mathrm{T}}\nabla\Gamma \geq 0$.

4.1.4 BVP Predictor-Corrector

A prediction step is included in the initial step of the line search to reduce the number of inner-loop BVP iterations. Linear approximations to the expected changes in the positions due to perturbations of the design variables in $\mathbf{k}$ are calculated using the STM. These perturbations are then further mapped to the required change in the velocities. Excluding the simple case

of varying $\mathbf{r}_{i+}$ directly, the general, non-contemporaneous perturbation to the position at a node is:

$$d\mathbf{r}_{i+1,-} = \mathbf{A}_i d\mathbf{r}_{i+} + \mathbf{v}_{i+1,-}\left(dt_{i+1} - dt_i\right) \tag{4.16}$$

Two special cases exist as the initial and final positions, $\mathbf{r}_0$ and $\mathbf{r}_{\mathrm{N}+}$, are constrained to specific orbits and can not be varied independently of time:

$$d\mathbf{r}_0 = \mathbf{v}_{0-} dt_0 \tag{4.17}$$

$$d\mathbf{r}_{\mathrm{N}+} = \mathbf{v}_{\mathrm{N}+} dt_{\mathrm{N}} \tag{4.18}$$

To enforce continuity, the position differential at each node is corrected via a change in the velocity of the previous node:

$$\left(d\mathbf{r}_{i+1,+} - d\mathbf{r}_{i+1,-}\right) = \mathbf{B}_i d\mathbf{v}_{i+} \tag{4.19}$$

Substituting Equations (4.16) – (4.18) leads to the predicted changes in the velocities required by the multi-shooting algorithm:

$$d\mathbf{v}_{i+} = \mathbf{B}_i^{-1}\left[\mathbf{v}_{i+1,-}\left(dt_i - dt_{i+1}\right) - \mathbf{A}_i d\mathbf{r}_{i+} + d\mathbf{r}_{i+1,+}\right] \qquad i \neq 0, \mathrm{N}-1 \tag{4.20}$$

$$d\mathbf{v}_{0+} = \mathbf{B}_0^{-1}\left[\left(\mathbf{v}_{1-} - \mathbf{A}_0 \mathbf{v}_{0-}\right) dt_0 - \mathbf{v}_{1-} dt_1 + d\mathbf{r}_{1+}\right] \tag{4.21}$$

$$d\mathbf{v}_{\mathrm{N}-1,+} = \mathbf{B}_{\mathrm{N}-1}^{-1}\left[\mathbf{v}_{\mathrm{N}-1,-}dt_{\mathrm{N}-1} + \Delta\mathbf{V}_{\mathrm{N}}dt_{\mathrm{N}} - \mathbf{A}_{\mathrm{N}-1}d\mathbf{r}_{\mathrm{N}-1,+}\right] \tag{4.22}$$

Equation (4.21) and Equation (4.22) are again special cases due to the boundary orbit constraints on $\mathbf{r}_0$ and $\mathbf{r}_{\mathrm{N}+}$. The use of linear approximations limits the prediction step accuracy to small perturbations. After two additional converged solutions, larger steps in the line search are predicted using quadratic polynomial extrapolation of previously converged states as a function of α. Inclusion of the predictor step is found to at least halve the number of inner-loop iterations. However, the predictor step also enables larger overall step sizes (typically by several orders of magnitude) that might otherwise diverge when solving the inner-loop BVP. The cumulative effect of the increased step size can be the elimination of hundreds of inner-loop calls.

4.1.5 Addition and Removal of Impulses

It is quite common for all the optimality conditions except the magnitude limit on the primer vector, Equation (4.3), to be satisfied. In this case at least one additional interior impulse is required, located at the time of maximum primer vector magnitude, t_{m}. A new node is added to $\mathbf{k}$ at time t_{m} with state $\mathbf{x}(t_{\mathrm{m}})$. The position of the node is perturbed by $d\mathbf{r}_{\mathrm{m}}$ to initiate a velocity discontinuity, i.e. a new impulse (when the associated BVPs are solved). As the new node must be position continuous ($d\mathbf{r}_{\mathrm{m}-} = d\mathbf{r}_{\mathrm{m}+} = d\mathbf{r}_{\mathrm{m}}$), the position perturbation is mapped to state perturbations at neighboring nodes

using Equation (4.19) along with $d\mathbf{r}_{i+1,-} = \mathbf{A}_{\mathrm{m}} d\mathbf{r}_{\mathrm{m}}$, where $i+1$ corresponds to the node immediately after the new interior impulse. Further mapping to the velocity differentials at the new node gives the linear approximation of the new impulse:

$$d\mathbf{v}_{\mathrm{m}+} - d\mathbf{v}_{\mathrm{m}-} = -\mathbf{B}_{\mathrm{m}}^{-1}\mathbf{A}_{\mathrm{m}} d\mathbf{r}_{\mathrm{m}} - \mathbf{D}_i \mathbf{B}_i^{-1} d\mathbf{r}_{\mathrm{m}} \tag{4.23}$$

Recall from Equation (4.4) that an optimum impulse is parallel to the primer vector. Enforcing this condition and solving for the position perturbation gives:

$$d\mathbf{r}_{\mathrm{m}} = \alpha \left[-\mathbf{B}_{\mathrm{m}}^{-1}\mathbf{A}_{\mathrm{m}} - \mathbf{D}_i \mathbf{B}_i^{-1}\right]^{-1} \frac{\mathbf{p}_{\mathrm{m}}}{||\mathbf{p}_{\mathrm{m}}||} \tag{4.24}$$

where α is the value that minimizes the cost in the search direction given by the vector components of $d\mathbf{r}_{\mathrm{m}}$. Note that this equation follows the same derivation by Davis in Reference [26], modified to be consistent with the forward-shooting approach used in this work.

After an initializing search in the direction given by Equation (4.24), optimization using the full search direction with the newly added impulse is resumed until the gradient again becomes trivially small. This iterative loop of optimize, add interior impulse, optimize, continues until all optimality conditions are satisfied. It is important that the method is applied iteratively, one additional impulse at a time, as the primer vector changes unpredictably during the optimization [43]. For example, a trajectory that initially violates

$||\mathbf{p}(t)|| \leq 1$ may satisfy all optimality conditions upon convergence, indicating that additional interior impulses are not actually necessary.

Traditionally, impulsive primer vector theory has been applied to bi-impulsive initial guess trajectories. In this work trajectory phases are patched together, resulting in initial transfers with multiple interior impulses. Maneuvers unnecessary to the optimal solution shrink towards zero during optimization, causing singularities in the derivatives that can prevent convergence. Simply removing minuscule impulses is not possible, as some of them may be necessary for the optimal solution. An analytical check is required to ensure that removing an impulse will improve the cost of the transfer.

For a given node $\mathbf{x}_{i+}$, assume that the impulse is small and the trajectory is sufficiently close to the neighboring perturbed path such that linear approximations are sufficient. The impulse is effectively removed when $\mathbf{r}_{i+}$ is perturbed such that $d\mathbf{v}_{i+} = -\Delta\mathbf{V}_i$. Mapping the state changes necessary to maintain continuity leads to the required change in the design variable:

$$d\mathbf{r}_{i+} = \mathbf{B}_{(i-1)}\mathbf{B}^{-1}\left(t_{i+1}, t_{i-1}\right)\mathbf{B}_i\Delta\mathbf{V}_i \tag{4.25}$$

The mapping from t_{i-1} to t_{i+1} excludes the impulse at the ith node and must be calculated with an additional integration. Substitution into Equation (4.12) and noting that the change in cost must be negative gives the sufficient condition for removal of an interior impulse to improve the cost:

$$\left(\dot{\mathbf{p}}_{i+}^{\mathrm{T}} - \dot{\mathbf{p}}_{i-}^{\mathrm{T}}\right) \mathbf{B}_{(i-1)} \mathbf{B}^{-1}\left(t_{i+1}, t_{i-1}\right) \mathbf{B}_i \Delta \mathbf{V}_i < 0 \tag{4.26}$$

A similar condition exists for the initial impulse. Note that the initial impulse is removed by explicitly setting $\mathbf{r}_1$ to the state of the initial boundary orbit at time t_1:

$$\left(\dot{\mathbf{p}}_{1+}^{\mathrm{T}} - \dot{\mathbf{p}}_{1-}^{\mathrm{T}}\right) \mathbf{B}_0 \Delta \boldsymbol{V}_0 > 0 \tag{4.27}$$

Evaluating the removal of an impulse occurs when the magnitude of the maneuver is below a specified tolerance, typically selected sufficiently small such that the linear approximations are reasonably valid.

4.1.6 Numerical Considerations

As part of the goal of this work is to verify the energetic floor cost derived in the previous chapter, the convergence criteria are chosen to be extremely tight in order to document the lowest minima possible. Ideally, the optimization is considered converged when the gradient magnitude is on the order of 10^{-10}. Occasionally the problem becomes highly sensitive such that the gradient is not small despite being close to the optimum. A second convergence criteria on the absolute improvement of the impulsive cost is included, set at $|\Gamma(\mathbf{k} + \alpha \mathbf{s}) - \Gamma(\mathbf{k})| \leq 10^{-11}$ (equivalent to 10^{-7} m/s). The absolute difference criteria must be satisfied several times in succession before the solution is considered to be "converged".

For highly sensitive problems near the optimum, values of α on the order of 10^{-13} can be sufficient to minimize the cost along the current search direction. At this small magnitude, perturbations to $\mathbf{k}$ can leave the position discontinuities in the forward-shooting algorithm within the defined tolerance, resulting in no change in $\mathbf{v}_{i+}$. As a consequence, the cost function is not truly continuous at this very fine resolution. While the severity of this behavior is reduced with smaller tolerances, the position discontinuities can not be made arbitrarily small due to limitations on machine precision. With double precision numbers the tolerance is limited to roughly 10^{-13}, insufficient to mitigate the cost discontinuity.

While the position tolerance issue can not be fully eliminated, its effects can be significantly diminished by using quadruple precision ($\sim$32 digit) numbers. As a result, the position discontinuity tolerances can be reasonable reduced to as small as 10^{-20}, improving the continuity of the cost function. Similar improvement in the precision of the velocity differences leads to more accurate primer vector and gradient information. The notable drawback of this extra precision is a significant increase in the total computation time (approximately two orders of magnitude in the current Fortran implementation). The impact of this slowdown is reduced by first optimizing in double precision, then switching to quadruple precision for highly sensitive problems near the optimum (and only when necessary).

4.2 Halo to Capture Optimization

In this section the optimization algorithm is applied to two spacecraft trajectories generated in the previous chapter which are expected to be near-optimal. Both trajectories start on an L2 halo orbit, and transfer to one of two capture options: a tightly captured, low-altitude orbit, or a loosely captured high-altitude orbit. The impulsive cost of the trajectories before and after optimization are compared as a means of verifying the methods used to construct the orbits. The optimized cost is also used to confirm that the floor ΔV is a good measure of optimality.

4.2.1 Halo Orbit to Tight Capture

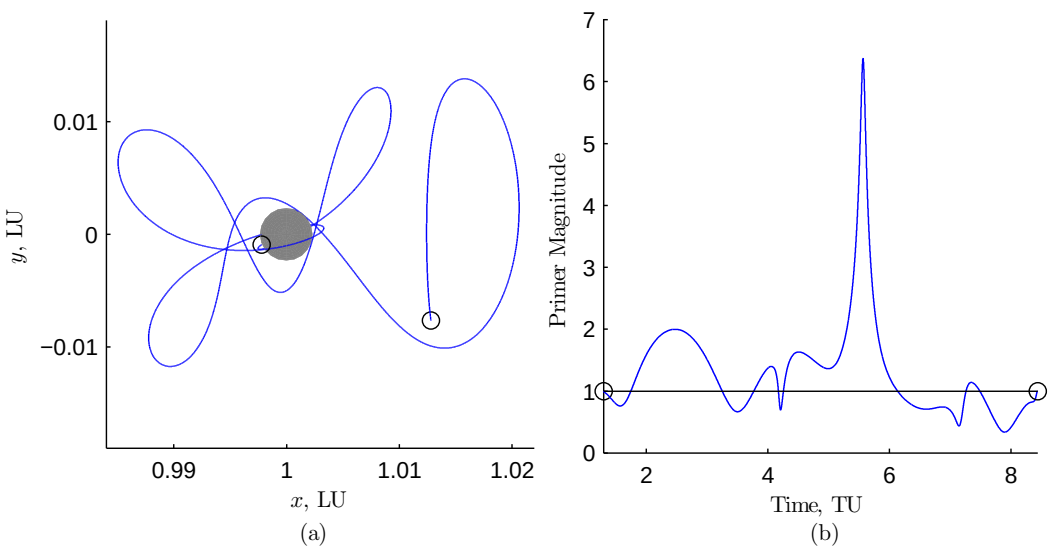

Figure 4.2: (a) Initial two-impulse, one-leg, halo orbit to tight capture trajectory. (b) Primer vector time history of the transfer. Circles indicate impulse locations

The first example is the transfer to the tight capture orbit. This trajectory is shown in plot (a) of Figure 4.2. A small impulse of 1.86 m/s leads to a relatively swift departure from the initial halo orbit. The transfer follows a highly-perturbed trajectory with several low-altitude Europa periapsides, ending with a 422 m/s impulse to enter the capture orbit (not shown for transfer visibility). The time history of the primer vector magnitude is shown in plot (b) of Figure 4.2, where time is measured from the initial xz-plane crossing of the halo orbit. It is readily seen from the history that the trajectory is sub-optimal: both impulses have non-zero slopes of p, and its value is frequently above unity with a notable spike near $T = 5.50$ TU. While the primer vector appears to indicate a highly sub-optimal trajectory, the floor ΔV is 422.18 m/s. Therefore from an energy standpoint, the cost can at most be reduced by 1.65 m/s, implying that the current solution is already near-optimal. It follows that the apparent severe optimality violation of the primer magnitude can not be considered as a proxy for optimality, an important takeaway when using primer vector theory on such highly-sensitive orbits.

Optimization of the trajectory results in the converged transfer shown in Figure 4.3. From a physical standpoint the transfer is essentially unchanged, indicating the solution has stayed within its local bin of attraction. Inspection of the optimized trajectory shows that the departure time has been shifted backwards, as expected from the initial non-zero slope of p. This coasting arc accounts for the largest change from the initial guess, with a total difference of 0.15 TU, equivalent to 2 hours. Another notable change in the transfer is

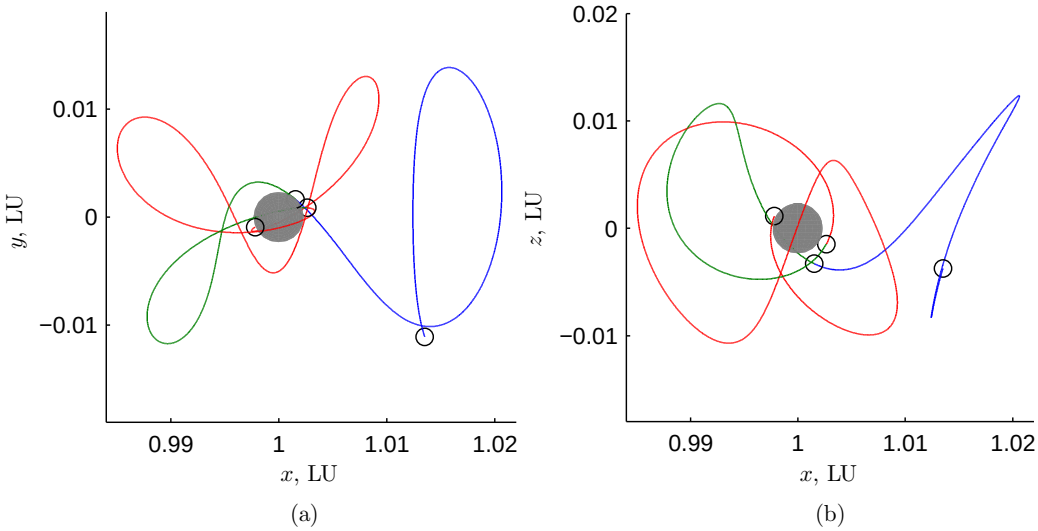

Figure 4.3: Optimized three-leg halo orbit to tight capture transfer, circles indicate impulse locations. (a) xy view (b) xz view

the addition of two interior impulses, both occurring near Europa periapse. These locations are expected, as the energy of the trajectory is most sensitive to changes when the velocity in the rotating frame is at a maximum [26]. Note that based on the peaks in the primer vector history in Figure 4.2, it initially appears that an additional five interior impulses are required. The fact that only two are required emphasizes the principle that impulses should be iteratively added only as needed.

The optimality of the solution is verified by checking the primer magnitude and magnitude derivative history in Figure 4.4. It is first noted that the primer magnitude remains below unity throughout the trajectory. Recall from Equation (4.4) that the primer magnitude is explicitly enforced to be unity at

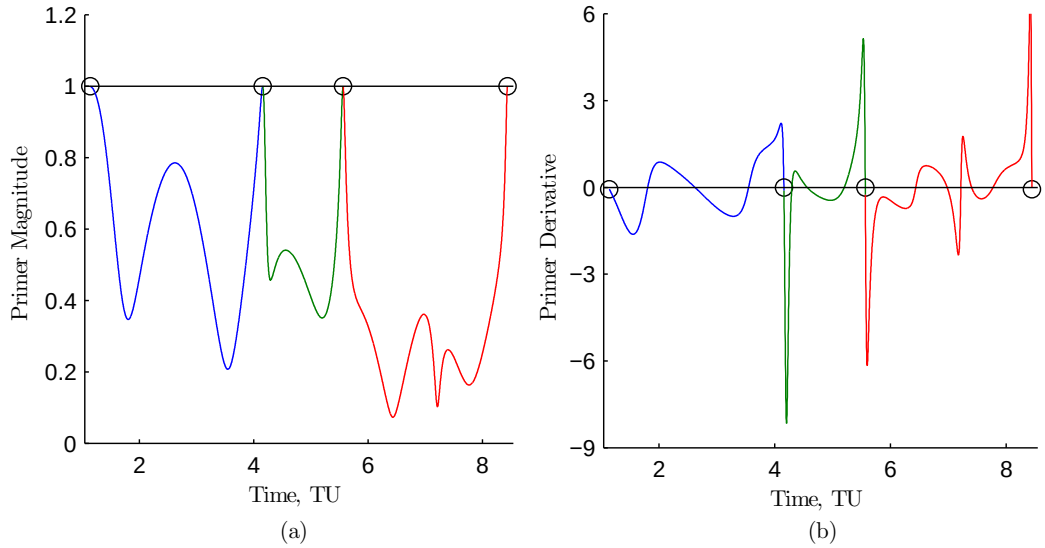

Figure 4.4: Optimal three-leg tight capture transfer primer vector history, circles indicate impulse locations. (a) Primer magnitude (b) Primer magnitude time derivative

impulses. Visually it appears the slopes are non-zero "cusps" at the impulses, however the time derivative history in the right plot of Figure 4.4 confirms that $\dot{p}$ is sufficiently near-zero and continuous (although rapidly varying) at maneuvers. As all of the necessary conditions are satisfied within tolerance, the final trajectory is confirmed to be a local optimum.

Table 4.1: Impulse magnitudes for the halo orbit to tight capture transfer, m/s

Case	$\Delta \boldsymbol{V_0}$	$\Delta \boldsymbol{V_1}$	$\Delta \boldsymbol{V_2}$	$\Delta \boldsymbol{V_3}$	Γ
Initial	1.854	421.97	—	—	423.83
Optimal	1.035	0.399	0.091	422.03	423.56

A comparison of the impulses before and after optimization is given in Table 4.1. Looking at the total cost, Γ, it is seen that the optimized trajectory

requires 423.56 m/s, saving (a rather small) 0.27 m/s from the original trajectory. Given that the is 1.36 m/s above the energetic floor, it is plausible that the solution is a global minimum. Looking at individual impulses, it can be seen that the departure cost was reduced by 0.82 m/s due to the inclusion of the coasting arc. This improvement is offset by the two new interior impulses, which add 0.49 m/s to the total cost. Both new impulses are nearly parallel to their corresponding velocities, primarily changing the energy of the trajectory.

4.2.2 Halo Orbit to Loose Capture

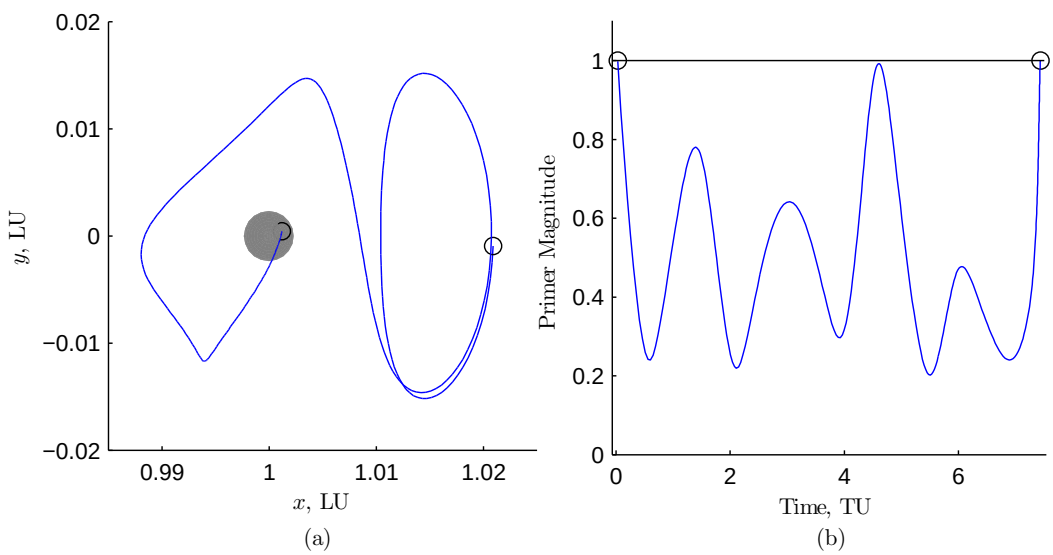

Figure 4.5: (a) Initial one-leg guess transfer trajectory from halo orbit to loose capture. (b) Primer magnitude time history of the transfer. Circles indicate impulse locations

The next transfer trajectory considered is from a second L2 halo orbit to a loose capture at Europa. Recall from Chapter 3 that this transfer was

generated using a full-state perturbation unstable manifold of the halo orbit. As the current multi-shooting algorithm assumes the positions across the first impulse are identical, targeting is used to change the trajectory to a velocity-only perturbation with negligible change to the total ΔV. An xy-plane view of the trajectory is shown in the plot (a) of Figure 4.5. The use of the unstable manifold results in a gradual departure from the halo orbit, leading to the insertion impulse at a low-altitude periapse. Looking at the primer history in the plot (b), the transfer appears to be a good initial guess as the magnitude remains below unity at all times. Evaluation of the slopes at the impulses gives $\dot{p}_0 = -2.40$ and $\dot{p}_\mathrm{N} = 0.05$, indicating that an initial coasting arc may be sufficient to optimize the transfer [41]. However, considering that the total cost of this transfer is 29.22 m/s compared to a predicted floor of 29.12 m/s, a notable improvement is not expected.

Running the optimization algorithm for the loose capture transfer does not result in an analytically optimal time-free orbit: $\dot{p}_0$ is non-zero in the final solution despite a significant coasting arc of 27 hours, more than half of the period of the halo orbit. This continual time-shifting follows a known property of unstable manifolds, where a trade off between flight time and perturbation size exists for a given manifold [53]. Essentially, the initial impulse to depart the halo orbit can be made infinitesimally small at the cost of infinite travel time. Given this insight, the constraint that $\dot{p}_0 = 0$ can be safely ignored as the spacecraft is departing on a manifold-like transfer.

The converged trajectory is given in the plot (a) of Figure 4.6. Once

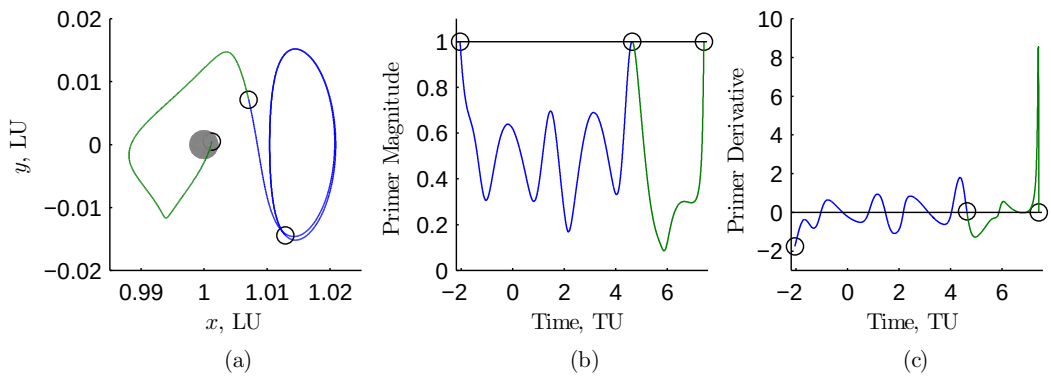

Figure 4.6: (a) Optimal two-leg transfer trajectory from halo orbit to loose capture at Europa. (b) Primer magnitude time history of the transfer. (c) Primer derivative time history of the transfer. Circles indicate impulses

again, the overall path of the spacecraft remains unchanged, although an interior impulse has been added near a high-altitude periapse at Europa. The interior and final maneuvers are near-parallel to the velocity in the rotating frame, indicating they primarily change the energy of the trajectory. Conversely, the initial impulse is almost perpendicular to the velocity, resulting in a small direction change to initiate the unstable manifold transfer. Looking at the primer magnitude history in plot (b) and the primer time derivative in plot (c) of Figure 4.6 shows that all optimality conditions are satisfied to numerical tolerance, recalling that $\dot{p}_0 = 0$ has been excluded.

Table 4.2: Impulse magnitudes for the halo orbit to loose capture transfer, m/s

Case	$\Delta \boldsymbol{V_0}$	$\Delta \boldsymbol{V_1}$	$\Delta \boldsymbol{V_3}$	Γ
Initial	0.026	29.19	—	29.22
Optimal	3.1E-4	1.8E-5	29.19	29.19

A summary of the impulses and total cost is given in Table 4.2. It is

readily apparent that the converged solution is marginally improved, with a total reduction of only 0.026 m/s. The minimal reduction in the total cost is expected, as the initial solution was already near the predicted floor cost of 29.12 m/s. The optimal cost in a marginal 0.07 m/s above the energetic floor, strongly indicating it is a global optimum. Note that while the interior impulse is minuscule, evaluating Equation (4.26) shows that it is necessary for analytical optimality. In terms of practicality for real spacecraft, the interior impulse can be excluded with negligible effects on the trajectory and cost.

4.3 Resonant Orbit to Europa Capture

The trajectories optimized so far have focused on the final phase of the capture problem, starting at a halo orbit already in the vicinity of Europa. It is ultimately desirable to have a fully optimized end-to-end transfer that includes the approach phase from beyond Europa's orbit. Constructing such a trajectory is a complex process, particularly in three-dimensions where natural intersections of orbits are not guaranteed to exist. As a starting point, this work focuses on extending the capture transfers optimized in earlier sections to include one additional approach orbit. A detailed process of generating this extension is given below.

4.3.1 Three-dimensional Resonant Orbit

Extending the transfer to include the approach phase starts with the generation of a new initial reference orbit. An exterior Europa approach from

Ganymede typically utilizes resonant orbits, as seen in References [54] and [4]. Following these works, the orbits are referred to as p:q resonances, where p and q are the number of inertial spacecraft and moon revolutions, respectively. Given that an optimized transfer from the L2 halo orbit has been found, a useful connecting orbit would be one that naturally transfers between a resonant orbit and a halo orbit. Periodic orbits that traverse multiple dynamic regimes are well known, typically found directly using heteroclinic connections between invariant manifolds, or indirectly by continuation of bifurcations to an unstable orbit [57, 101]. The trajectory sought here is a 3D version of what Restrepo and Russell call *connecting resonance periodic orbits* [80].

Recall from symmetry of the CRTBP that any trajectory with perpendicular crossings of the xz-plane as boundary conditions will result in a periodic orbit. Given the initial state of the halo orbit is defined with a perpendicular crossing of the xz-plane, it follows that finding a second perpendicular crossing far from Europa will lead to a new periodic orbit. A small parallel perturbation of δv is added to the initial perpendicular velocity. The perturbed state is propagated forward in time by 94 TU, approximately equal to 15 Europa revolutions. This time is sufficiently long to result in expected useful resonances. The state and time of the trajectory at subsequent xz-plane crossings are saved. To ensure the state is associated with a resonant orbit, only crossings that occur after the trajectory has departed Europa's sphere of influence are recorded. The process is repeated over a 10,000 point grid search of velocity perturbations, up to a maximum δv of 0.10 m/s.

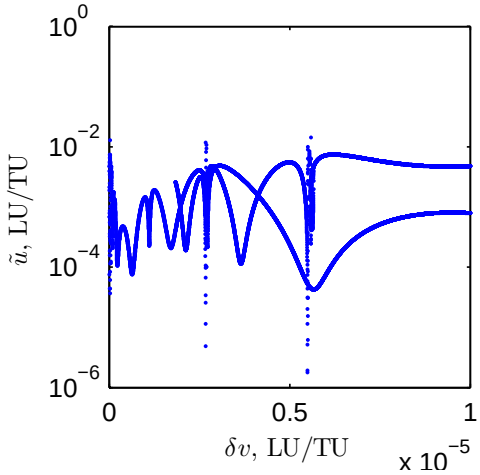

Figure 4.7: Magnitude of non-perpendicular velocity at xz-plane crossings due to perturbations of halo orbit initial state v_0

In the search for a second perpendicular crossing only two states are relevant: u and w. The dimensionality can be further reduced by combining the velocities to $\tilde{u} = \sqrt{u^2 + w^2}$, where $\tilde{u} = 0$ for a perpendicular planar crossing. Figure 4.7 shows this velocity magnitude as a function of the perturbation to the halo orbit. Most perturbation magnitudes result in only one or two plane crossings in the alloted time frame, however there are two regions where numerous crossings can be seen. These clusters indicate that the trajectory returns to a loose orbit near Europa. The corresponding trajectories with small values of $\tilde{u}$ are used as initial guesses to hone in on new periodic orbits.

The initial state is differentially corrected to target an exact (to machine precision) perpendicular plane crossing. For an xz-plane to xz-plane trajectory with initial state $\mathbf{x}_0$, there are three variables (x_0, z_0, and v_0) to target two

velocities. The dimension is reduced by one by keeping either of the position variables constant, resulting in a fully constrained problem. Recall that there may be multiple plane crossings between the initial and final states. Given the time between desired crossings, $T/2$, is implicitly varied by stopping at $y = 0$, and keeping z_0 fixed, the differential correction to the initial state is given by the solution to the system of equations:

$$\begin{bmatrix} \delta u \\ \delta w \end{bmatrix} = \left(\begin{bmatrix} \Phi_{\mathrm{ux}} & \Phi_{\mathrm{uv}} \\ \Phi_{\mathrm{wx}} & \Phi_{\mathrm{wv}} \end{bmatrix} - \frac{1}{v} \begin{bmatrix} \dot{u} \\ \dot{w} \end{bmatrix} \begin{bmatrix} \Phi_{\mathrm{yx}} & \Phi_{\mathrm{yw}} \end{bmatrix} \right)_{T/2} \begin{bmatrix} \delta x_0 \\ \delta v_0 \end{bmatrix} \tag{4.28}$$

where Φ_{ux}, etc. are individual elements of the STM corresponding to the subscripted variables [42].

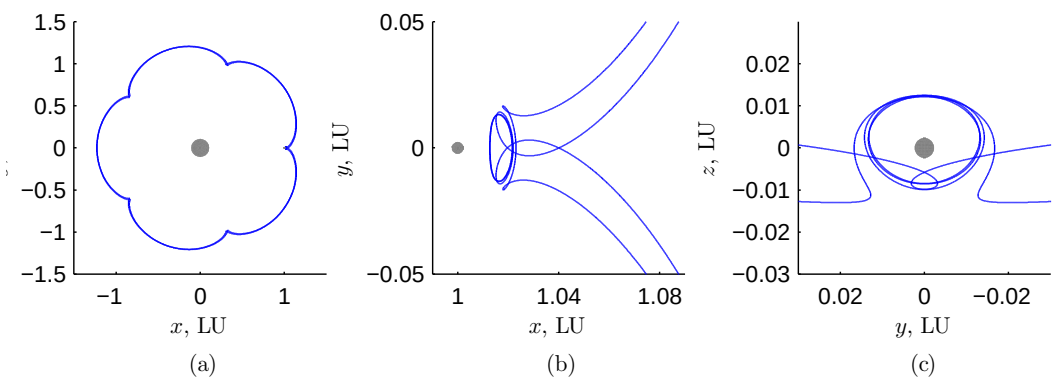

Figure 4.8: Example periodic orbit (labeled d) that includes 5:6 resonance and halo orbits. (a) Full orbit with Jupiter for scale (b, c) xy and yz detailed views near Europa

Table 4.3: Non-zero parameters and stability indices for example members of the resonant-halo orbit family

Parameter	**a**	**b**	**c**	**d**
x_0, LU	1.00742246381	1.01360110944	1.02040012031	1.02156524254
z_0, LU	0.03267463087	0.02587220941	0.01614679433	0.01253412421
v_0, LU/TU	-0.00000000024	-0.01238895614	-0.02580667789	-0.02431113981
T, TU	91.257100	89.125299	88.280002	88.311965
C, LU^2/TU^2	3.0005299	3.0013841	3.0021643	3.0025645
k_1	6.6E+12	2.6E+13	2.8E+13	1.0E+14
k_2	-7.05	-0.30	0.03	-2.0

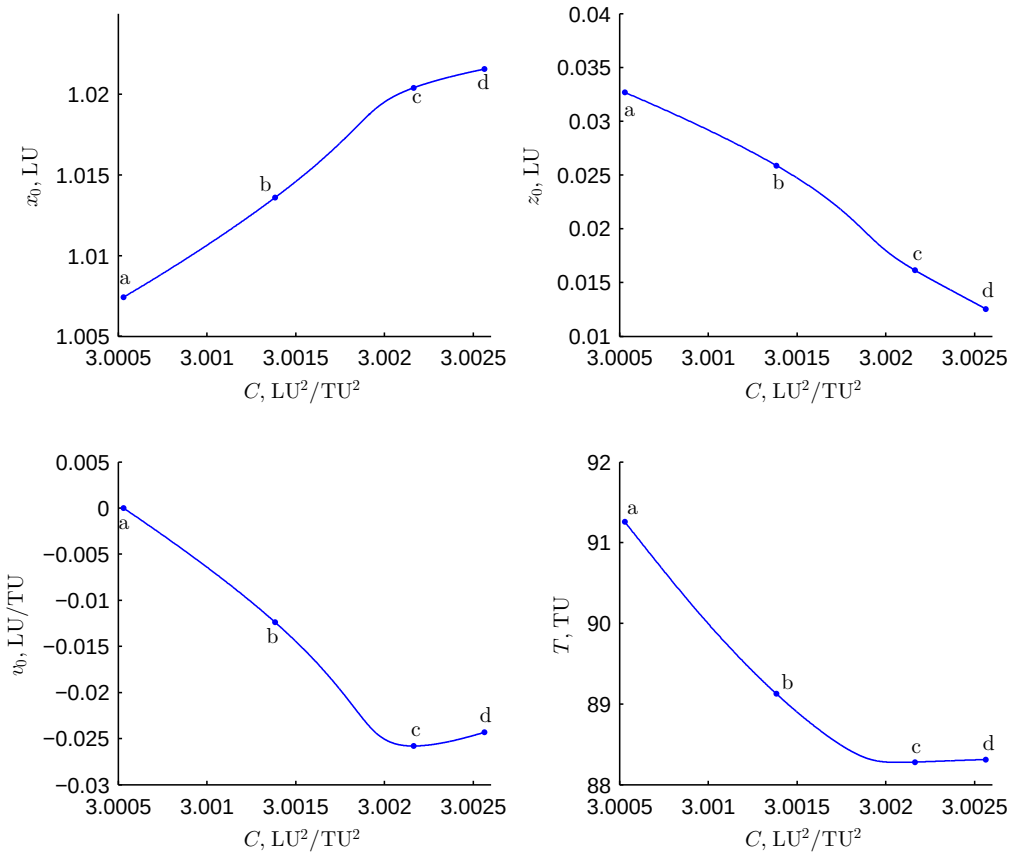

Figure 4.9: Characteristic curves of the 5:6 resonant-halo orbit family. Points correspond to orbits listed in Table 4.3

Differential correction of the grid search based initial guess leads to the fully-periodic, three-dimensional orbit shown in Figure 4.8, with non-zero initial states and periodic time listed as orbit (d) in Table 4.3. The Jacobi constant of this new orbit is a small increase from the original halo orbit energy. Given that the tight capture Jacobi constant is 3.00950434, the new periodic orbit is energetically closer to the capture orbit than the halo orbit was, and a cheaper transfer is expected. The trajectory starts in a near-halo orbit before falling off after a few revolutions, similar to the path followed by invariant manifolds. Next the trajectory enters a slightly inclined, 5:6 resonant orbit. Halfway through the orbit there is a high-altitude Europa flyby shadowing the near-halo phase, visible in plot (b) of Figure 4.8. A second resonant phase occurs, ending at reentry of the halo-like orbit.

A family of these orbits is generated using continuation methods with the Jacobi constant as a generating parameter. Surveying the family allows selection of different resonant orbits depending on the desired transfer. Initial states and periodic times for a few members of the family are provided in 4.3, with full characteristic curves shown in Figure 4.9. The stability of the periodic orbits to perturbations in the initial state is evaluated using the eigenvalues, λ_i, of the STM over one orbital period, a.k.a. the monodromy matrix. Stability indices are defined as $k_i = \lambda_i + 1/\lambda_i$, where absolute values greater than 2 indicate instability, and only two non-trivial indices exist [14]. All members of the resonant-halo family are extremely unstable with indices on the order of 10^{13}, as seen in Table 4. The instability is predominantly a result of the

dynamically chaotic near-halo portion of the orbit.

4.3.2 Resonant Orbit to Tight Capture

The next step is to connect the new periodic orbit to the previously optimized tight capture transfer. Orbit (d) of the resonant-halo family is selected as it closely shadows the halo orbit of the optimized tight capture transfer. A simple direct targeting approach is used to avoid generating and searching a broad space of three-dimensional invariant manifolds. It is assumed that two small maneuvers will be sufficient to connect the phases: the first to target the halo orbit from the resonant phase, and the second to capture into the halo orbit. For this initial approach, the locations of the impulses are selected heuristically. Following two-body approximations it is expected that a near-optimal targeting impulse will occur at one of the apsides of the resonant orbit. Similarly, recall that in the CRTBP the energy change from an impulse is maximized at the location of maximum velocity in the rotating frame. The combination of these two insights indicates that the apsides just before and after the high-altitude Europa flyby are likely good initial guesses for the resonant departure impulse location. Both options are considered for comparison. The targeted halo orbit location is the initial state of the halo orbit, as the location is naturally in close proximity to the halo-resonant orbit and occurs at an xz-plane crossing, allowing use of Equation (4.28). A minor difference to the equation is that the time of flight is from the initial departure impulse to the target plane crossing, t_{f}, rather than the time between two

planar crossings, $T/2$.

With the location of the resonant departure and halo capture impulses known, the resonant-to-halo transfer trajectory becomes a highly-sensitive single-leg BVP solved by iterative application of Equation (4.28). Comparing the potential departure locations shows that the impulse before Europa flyby requires 0.53 m/s to target the halo orbit, versus 3.56 m/s for the post-flyby impulse. However, the total cost up to halo orbit capture is effectively 15 m/s for both options. Given the near-equal cost, a different selection criteria is used to proceed. Accounting for the sensitivity of the trajectory to the design variables leads to the selection of the post-flyby option, as it is expected to exhibit less chaotic behavior and faster targeting convergence. The total ΔV for this initial transfer is 439.88 m/s, with a predicted floor cost of 419.38 m/s. Note that this minimum is lower than the original tight capture as the energy difference between the resonant orbit and capture orbit is smaller.

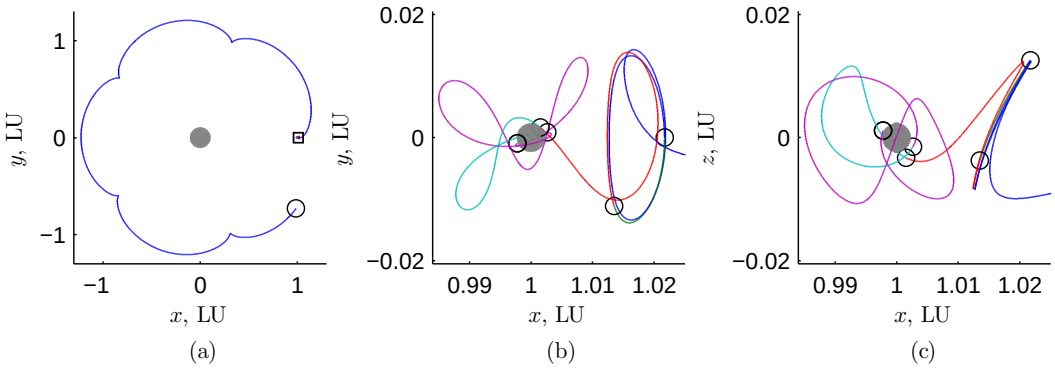

Figure 4.10: Initial five-leg guess for resonant to tight capture transfer trajectory. Circles indicate impulses. (a) Full trajectory with Jupiter for scale; (b, c) xy and xz detailed views near Europa

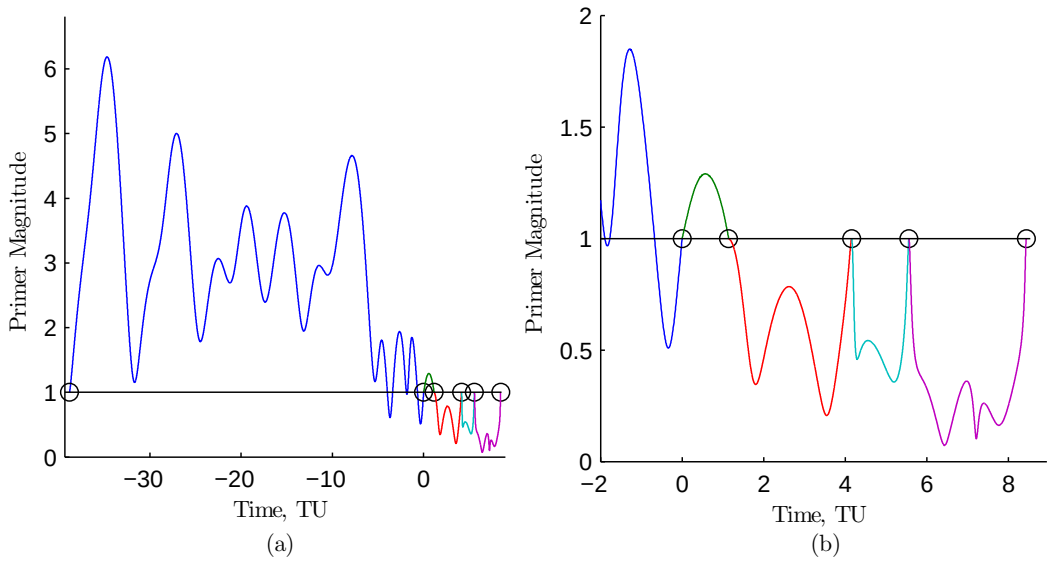

Figure 4.11: Primer magnitude history of initial guess resonant to capture transfer. Circles indicate impulses. (a) Full history; (b) Detailed view over the halo to capture phase

The initial guess trajectory for the transfer is shown in Figure 4.10, where circle markers highlight the location of the impulses. Plot (a) shows the full trajectory in the rotating frame, with detailed views of the halo and capture phase in plots (b) and (c). The halo orbit capture maneuver is seen at the top of the halo orbit, followed by a short coasting phase to the start of the halo to capture phase of the transfer. Comparison to Figure 4.3 shows that this phase is unchanged from the previously optimized solution, with optimality of the phase verified by the primer vector history in plot (b) of Figure 4.11. It is clear from plot (a) that the newly added resonant to halo orbit phase does not satisfy optimality, indicated by several long periods with $p > 0$.

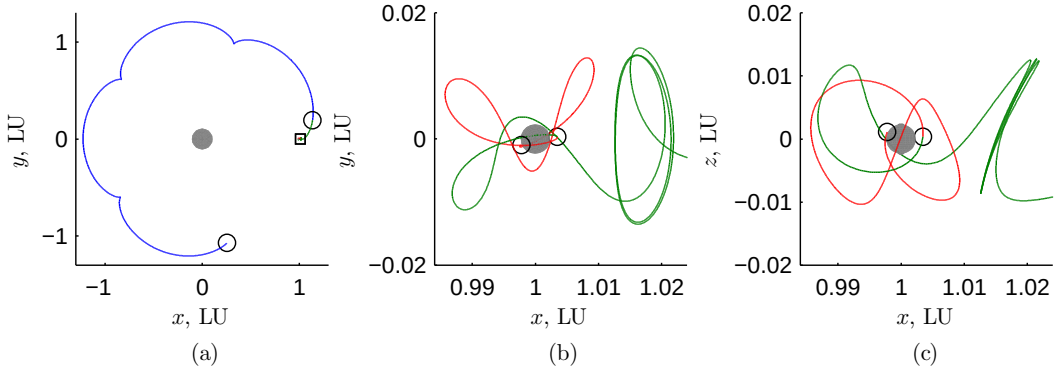

Figure 4.12: Optimized resonant to tight capture transfer trajectory with three legs. Circles indicate impulses. (a) Full orbit with Jupiter for scale; (b, c) xy and yz detailed views near Europa

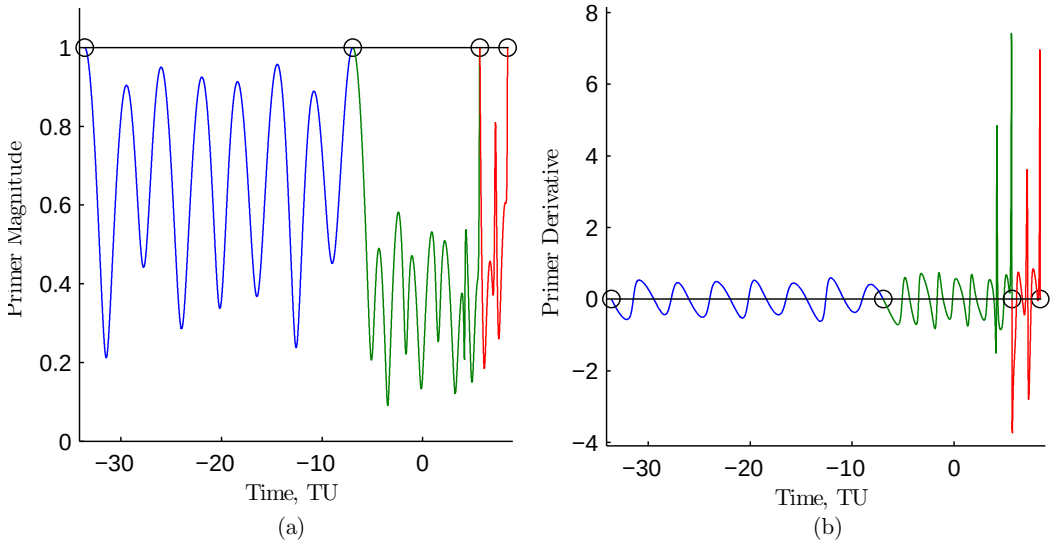

Figure 4.13: Time history of the primer vector for the optimal three-leg resonant to tight capture transfer. Circles indicate impulses. (a) Primer magnitude; (b) Primer magnitude time derivative

The optimization algorithm successfully converges to the trajectory

Table 4.4: Impulse magnitudes for the resonant orbit to tight capture transfer, m/s

Case	ΔV_0	ΔV_1	ΔV_2	ΔV_3	ΔV_4	ΔV_5	Γ
Initial	3.56	12.77	1.04	0.40	0.09	422.03	439.88
Optimal	0.15	1.23	0.89	421.74	—	—	424.12

shown in Figure 4.12. A total of five major iterations, where an impulse is either added or removed, are required. The initial departure impulse is removed, shifting the new departure maneuver forward in time to shortly after perijove of the resonant orbit. A new impulse has been added roughly 4 days before entering the region of the halo orbit. Both of the impulses used to patch the transfer phases are removed, resulting in a ballistic trajectory leg that closely shadows the halo orbit. Similarly, the first Europa periapse maneuver has been removed, indicating that optimizing the full transfer requires changing the previously optimal halo to tight capture phase. The last two impulses remain near Europa periapse. Optimality is visually confirmed by the primer vector history seen in Figure 4.13, with all impulse satisfying $p_i = 1$ and $\dot{p}_i = 0$.

A summary of the impulse magnitudes in Table 4.4 shows that the optimized total ΔV is 424.12 m/s, an improvement of 16 m/s. This total cost is 5 m/s above the energetic floor and is therefore close to the global optimum, noting that primer vector theory confirms the solution is a local optimum. The first three impulses are all small, on the order of 1 m/s or less, indicating that the transfer has converged towards quasi-ballistic, manifold-like behavior. These maneuvers are not tangential to the rotating velocity and primarily align

the transfer with the capture orbit, equivalent to a plane change in the two-body problem. The capture burn is near-parallel to the velocity and performs the majority of the energy change from the transfer.

4.3.3 Resonant Orbit to Loose Capture

The next transfer considered is from the resonant phase to the loose capture orbit. A different initial resonant orbit, family member (c), is selected to be more energetically consistent with the halo orbit used in the previously optimized halo to loose capture solution. Connecting both phases results in an initial guess transfer with a total cost of 52.58 m/s, compared to the floor of 30 m/s.

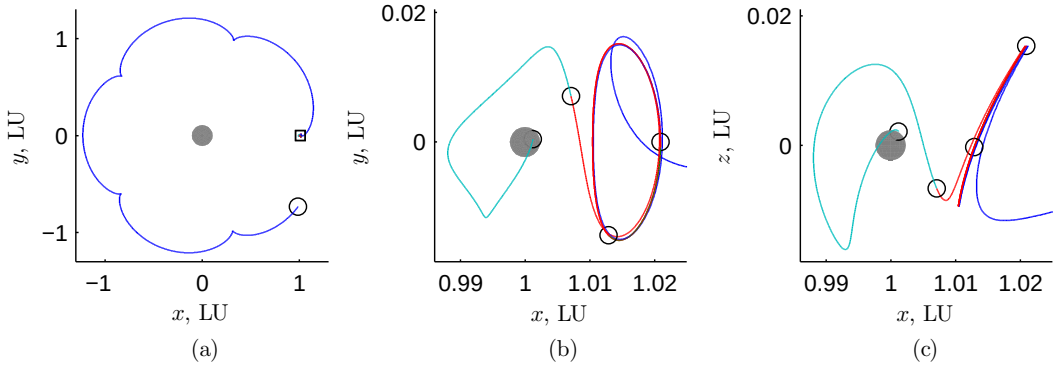

Figure 4.14: Initial four-leg resonant to loose capture transfer trajectory. Circles indicate impulses. (a) Full transfer with Jupiter for scale; (b, c) xy and xz detailed views near Europa

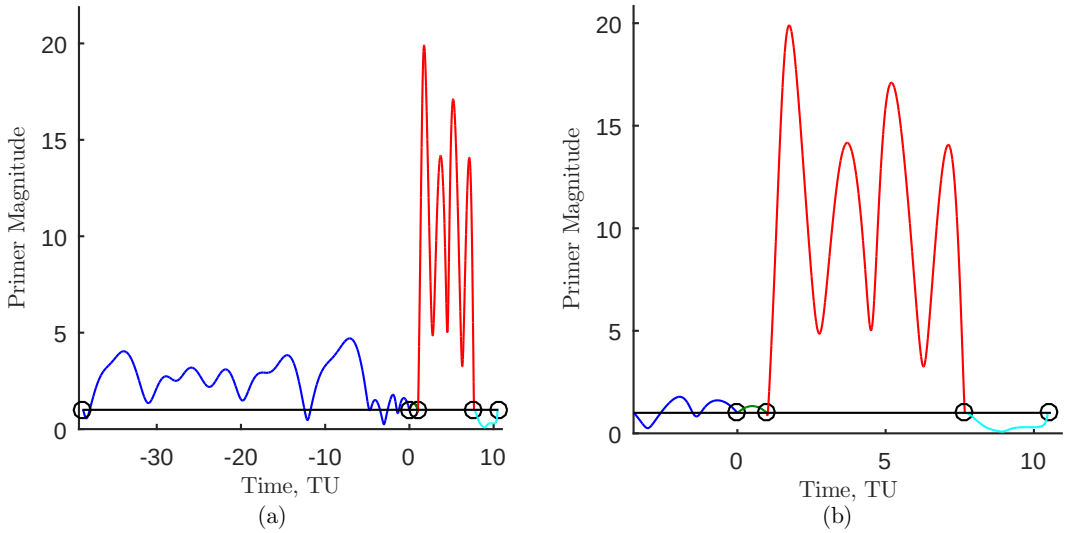

Figure 4.15: (a) Primer magnitude time history of initial resonant to loose capture transfer. (b) Detail of primer magnitude during halo to capture phase. Circles indicate impulses

Figure 4.14 shows the initial four-leg trajectory. Once again the resonant orbit connects directly to the halo, followed by a short coast to match the phasing of the halo to loose capture transfer. The primer vector history in Figure 4.15 shows that this new transfer is not optimal. An interesting note is that the previously optimal two-leg halo to loose capture phase (starting at $t_2 = 1.0$) now has a non-optimal first leg. This change is a numerical artifact caused by near-singular derivatives when the impulses are close to zero; the slight change to the halo departure impulse from adding the resonant orbit is sufficient to drastically change the primer vector history.

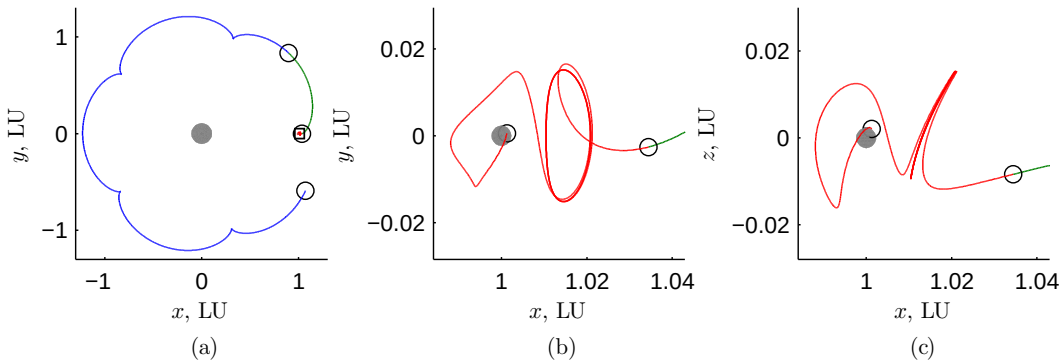

Figure 4.16: Optimal resonant to loose capture transfer trajectory. Circles indicate impulses. (a) Full orbit with Jupiter for scale; (b, c) xy and xz detailed views near Europa

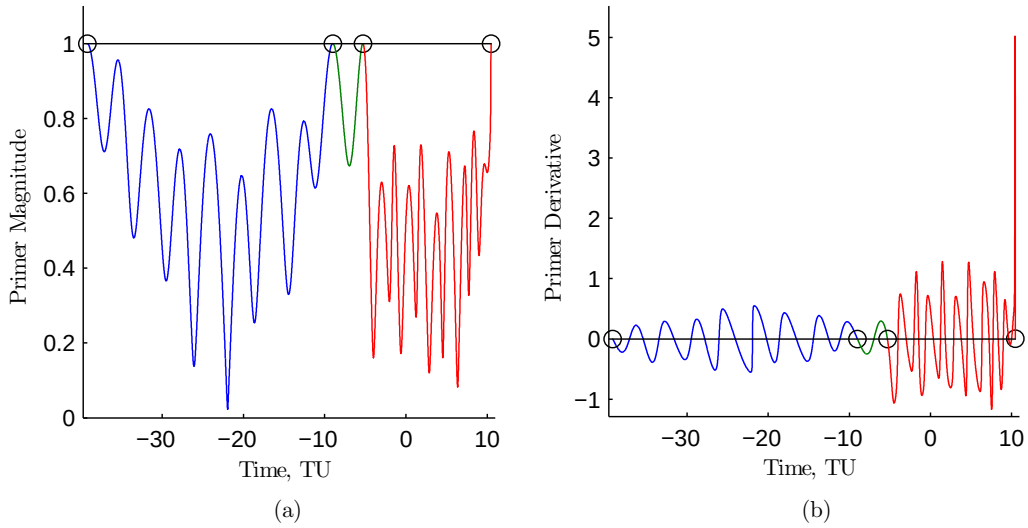

Figure 4.17: Primer vector time history of the optimal three-leg resonant to loose capture transfer, circles indicate impulses. (a) Primer magnitude (b) Primer magnitude derivative

Optimization converges to a four-impulse trajectory that closely shad-

Table 4.5: Impulse magnitudes for the resonant orbit to loose capture transfer, m/s

Case	ΔV_0	ΔV_1	ΔV_2	ΔV_3	ΔV_4	Γ
Initial	18.79	4.52	0.08	1.81E-5	29.19	52.58
Optimal	0.35	0.34	10.44	29.38	—	40.51

ows the initial guess, shown in Figure 4.16. The first impulse is shifted back towards an earlier departure shortly before apojove. As with the tight capture case, the halo orbit patching maneuvers are removed. Two new impulses are added leading up to the halo, one before the last apojove and another on approach to the halo orbit. The location of the capture maneuver remains relatively unchanged. Optimality of the solution is again visually confirmed via the primer vector history shown in Figure 4.17.

A summary of the impulses in Table 4.5 shows that the optimized total ΔV is 40.51 m/s, a 23% improvement of 12 m/s from the initial guess, and 10 m/s above the energetic floor. This relatively large distance from the floor is expected, as several significant maneuvers occur well above the idealized minimum maneuver radius of $r_2 = 1760.7$ km used in Equation (3.6). The first two maneuvers of the transfer are small, non-tangential impulses that lead up to the halo orbit phase. Surprisingly, the large third maneuver (ΔV_2) is nearly perpendicular to the velocity in both the rotating and inertial frames, solely changing the trajectory direction rather than energy. The final capture impulse is within 3° of the rotating velocity (4° of the inertial velocity), and accounts for most of the energy change throughout the entire transfer.

4.3.4 Resonant Orbit to Loose Capture: "Bad" Initial Guess

All of the transfers optimized thus far have started with considerably good initial guesses. While the use of solutions close to the final answer is desirable in optimization, it leaves the robustness of the optimizer method untested. In a similar vein, the flexibility of the solution based on the initial guess (i.e. whether it is stuck in a local minimum well) is so far unknown as the initial and optimal trajectories are relatively close to the energetic floor. To that end, a third transfer case is considered utilizing an initial guess that is relatively poor compared to the minimum ΔV.

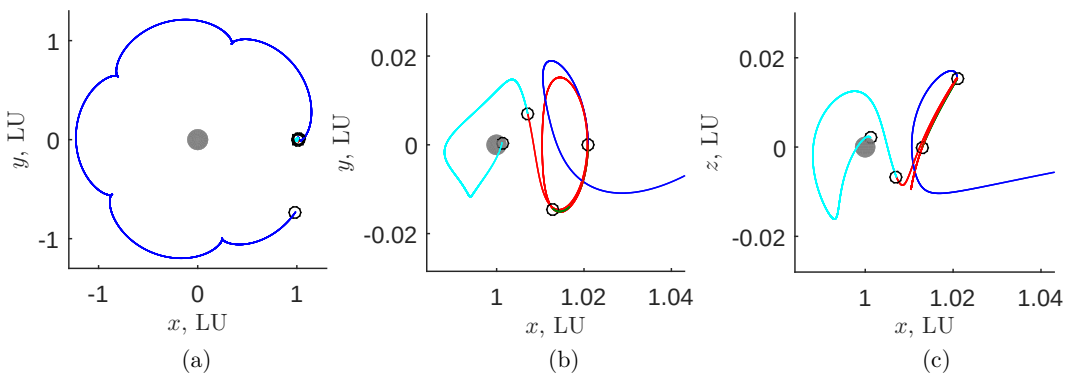

Figure 4.18: Initial bad guess, four-leg resonant to loose capture transfer trajectory. Circles indicate impulses. (a) Full transfer with Jupiter for scale; (b, c) xy and xz detailed views near Europa

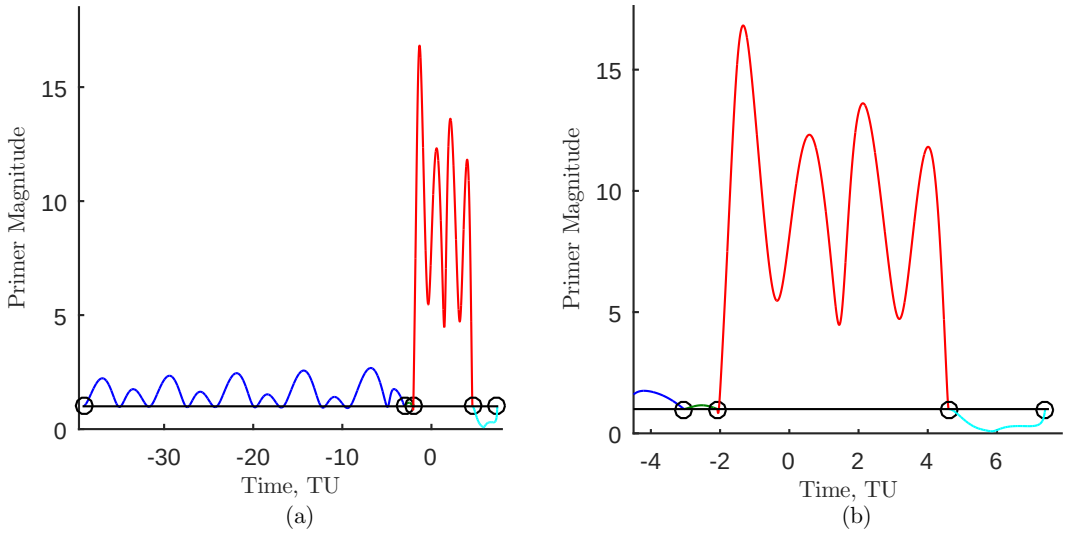

Figure 4.19: (a) Primer magnitude time history of initial bad guess resonant to loose capture transfer. (b) Detail of primer magnitude during halo to capture phase. Circles indicate impulses

The transfer is intentionally constructed using energetically similar resonant and capture orbits (C = 3.0025645 and 3.0027306 LU^3/TU^2, respectively) such that a low-cost solution is analytically plausible. However, the resonant orbit does not naturally travel near the halo orbit used for the loose capture, leading to high costs to depart the resonant orbit and capture into the halo, at 192 m/s and 150 m/s respectively. As an additional measure the halo departure impulse location is altered such that a significant 18 m/s maneuver replaces the original manifold transfer. This construction results in a relatively high cost of 388.85 m/s, while the energetic floor is 8.87 m/s second. Figure 4.18 shows the initial four-leg transfer. Detailed views in plots (b) and (c) show that the trajectory approaches the halo orbit at a high angle; the im-

pulse is 130° relative to the velocity in the rotating frame such that much of the impulse is spent changing the direction of the trajectory. The primer history in Figure 4.19 clearly shows a non-optimal solution, as the primer magnitude is above unity for most of the transfer.

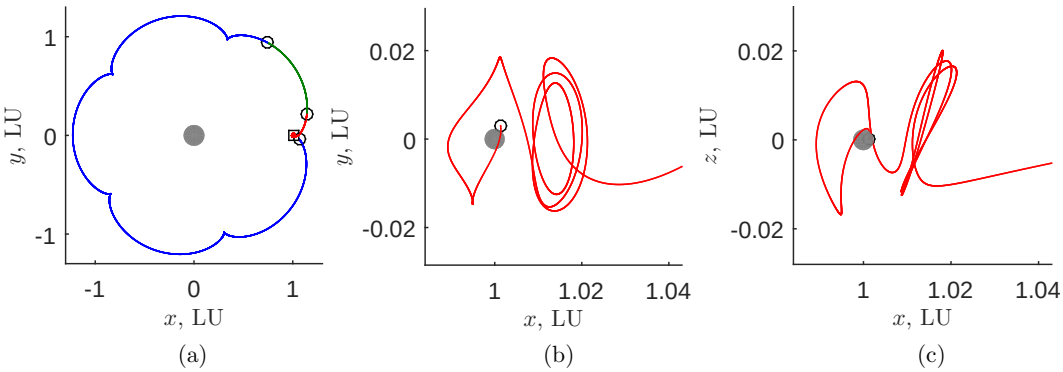

Figure 4.20: Optimized bad guess resonant to loose capture transfer trajectory. Circles indicate impulses. (a) Full orbit with Jupiter for scale; (b, c) xy and xz detailed views near Europa

Table 4.6: Impulse magnitudes for the bad guess resonant orbit to loose capture transfer, m/s

Case	ΔV_0	ΔV_1	ΔV_2	ΔV_3	ΔV_4	Γ
Initial	191.82	148.99	18.85	1.81E-5	29.19	388.85
Optimal	1.87	8.03	13.10	53.20	—	76.21

The optimization algorithm successfully converges to an optimal solution, showing that it is robust to poorly generated initial guesses. The trajectory shown in Figure 4.20 is markedly different from the original solution, particularly during the halo orbit phase. Much like the earlier transfers, the phase patching maneuvers have been removed and replaced by new impulses on approach to Europa. However, the new transfer does not cleanly shadow

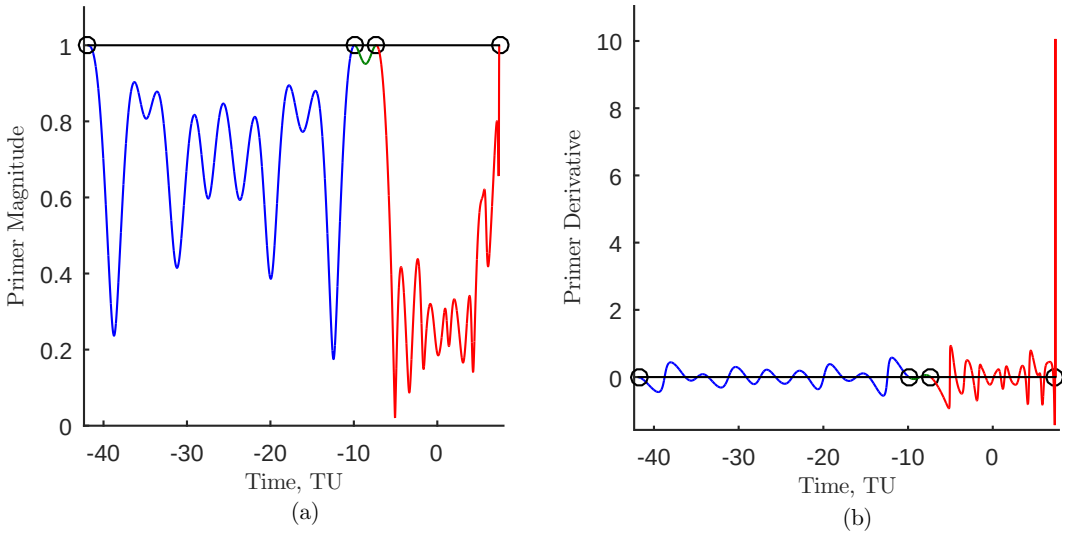

Figure 4.21: Primer vector time history of the optimized bad guess resonant to loose capture transfer, circles indicate impulses. (a) Primer magnitude (b) Primer magnitude derivative

the original halo orbit, but instead follows a relatively chaotic path. Another unique result is that the first impulse has shifted backward by 1.5 days to a non-apse departure that is 50,000 km from Europa, arguably close to its sphere of influence. The newly added maneuvers on approach to Europa are similarly not located at apsides. Despite these non-intuitive results, the primer history in Figure 4.21 visually confirms that all necessary conditions of optimality are met.

A summary of the impulses in Table 4.6 shows that the total cost has significantly reduced from 389 m/s down to 76 m/s. Much of the improvement comes from the initially large departure impulse shrinking by two orders of magnitude, and the complete removal of the large original ΔV_1. The savings

are mildly offset by a 24 m/s increase in the capture impulse. Checking the maneuver directions relative to the velocity shows that all of the impulses are non-tangential in both the rotating and inertial frames. The final impulse has a particularly noteworthy angle of 163° relative to the rotating frame, whereas all previous cases considered have near-tangential capture maneuvers.

While the cost of the transfer is markedly improved, it remains an order of magnitude larger than the energetic floor. This disparity strongly implies that the initial guess does indeed lead to a solution that is stuck in a local well. A likely culprit of this result is the use of the patching halo orbit, which has a Jacobi constant of 3.0021548 LU^3/TU^2. This energy level is in the wrong direction compared to the expected increase from the resonant orbit to the capture orbit. In fact, all of the maneuvers of the optimal solution take the trajectory energetically farther from the capture orbit, ultimately increasing the cost of the final impulse. While useful for patching transfer phases together, the halo orbit forces the trajectory to follow an inefficient path that is likely not the global optimum.

4.4 Conclusions

The principles of primer vector theory are successfully applied to optimize time-free capture transfer trajectories at Europa. The first two transfers considered are previously generated trajectories from halo orbits to a low-altitude tight capture, as well as a high-altitude loose capture. Despite the initial primer vector history appearing highly non-optimal, the optimization of

the two-impulse transfer to tight capture is relatively well-behaved. The total cost is slightly improved, indicating that the predicted floor ΔV is a good initial measure of optimality. Conversely, optimization of the unstable manifold transfer to loose capture experiences constant non-zero $\dot{p}_0$, as the cost can always be improved with a longer flight time. It follows that manifold transfers require a fixed time of departure to prevent the optimizer from targeting an infinite-time solution.

In order to extend the endgame problem to the approach phase, a new family of three-dimensional periodic orbits is generated using a grid search of perturbations to the L2 halo orbit. This perturbation-based technique enables the rapid construction of a manifold-like connection between resonant and halo orbits, without the need to employ intersections of stable and unstable manifolds. The use of the halo orbit as a boundary condition enables direct connection of the resonant-to-halo phase with the previously optimized capture transfers, with phasing naturally handled by a coasting arc along the halo. While impulses are initially used to connect the transfer phases, optimization of the end-to-end trajectory converges to a quasi-ballistic, manifold-like solution.

The use of unstable manifolds and long flight times in the trajectory results in hyper-sensitivity of the cost, primer vector, and gradient to changes in the design variables, particularly when near the local optimum. To the authors' knowledge, the resulting problem is the most sensitive application of impulsive primer vector theory in literature. This sensitivity is successfully

overcome by using a combination of multiple shooting legs and segments to limit the maximum values of the STM in the algorithm that solves the embedded boundary value problem solutions. New equations to decide when to remove miniscule impulses enables the elimination of most of the singularities in the transfer. Quadruple precision numbers similarly help by providing extra precision when the problem is in a shallow basin near the optimal solution.

A final take away from the sensitivity of the problem is that the primer vector necessary conditions are found to be extremely strict, confirming the typical struggles to optimize such highly sensitive orbits (using any method). This null result highlights the difficulty of claiming optimality when optimizing such challenging orbits, i.e. practitioners always have to decide on an optimality tolerance, typically in the absence of a known minimum ΔV (a luxury in the current study). While primer vector theory provides a strong visual confirmation of necessary conditions, the severity of the violations do not necessarily serve as a measure of proximity to optimality, as small perturbations to the design variables can completely alter the primer vector history. A prime example is that small maneuvers that have minimal impact on the total cost may be necessary for an analytically optimal trajectory. Conversely to primer vector theory, typical direct methods rely on arbitrarily set numerical tolerances to claim optimality. In either case, strict optimality conditions are notoriously challenging to achieve for multiple-revolution, multi-body space trajectories problems. As demonstrated in this chapter, a post processed primer vector history remains a useful tool (only requiring the STM along the final solution)

for such complicated problems, even if the optimization is performed without explicit use of primer vector theory.

Chapter 5

Electrodynamic Tether Periodic Orbits[1]

In this chapter the use of an electrodynamic tether in the Jupiter system is investigated. The primary focus of the work is on generating periodic orbits due to their utility in low-energy mission design. To that end a new conservative approximation to the tether force is developed that allows an integral of motion, enabling many of the techniques common to unperturbed CRTBP analysis. Analytical equations are derived for the torque on the tether to assess the controllability of a given orbit. The modified equilibrium points of this conservative tether are found as a function of tether length for both Metis and Io. From these equilibrium points new families of perturbed Lyapunov orbits are generated at Io, using a specialized targeting algorithm due to the lack of symmetry in the dynamics.

5.1 Tether-Perturbed Body Dynamics

The CRTBP is modified to the Lorentz-perturbed equations of motion:

[1]Bokelmann, K.A., Russell, R.P., Lantoine, G., "Periodic Orbits and Equilibria Near Jovian Moons using an Electrodynamic Tether," Journal of Guidance, Control, and Dynamics, Vol. 38, No. 1, 2015, pp. 15-29, DOI: 10.2514/1.G000428
Technical work and writing by Bokelmann, with guidance and edits by Russell and initial research ideas proposed by Lantoine

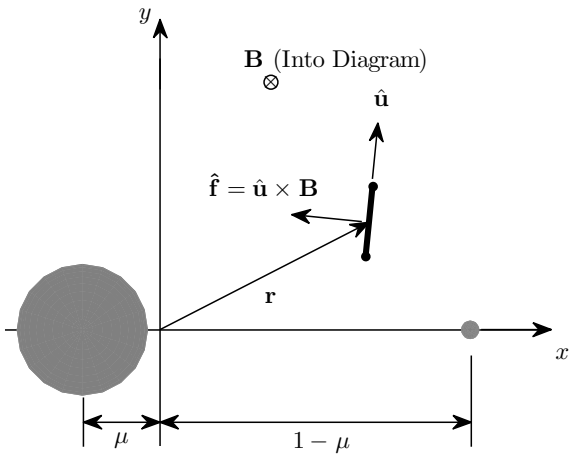

Figure 5.1: Planar diagram of CRTBP frame including radial tether and Lorentz force directions

$$\ddot{\mathbf{r}}_{\mathrm{EDT}} + 2\boldsymbol{\Omega} \times \dot{\mathbf{r}}_{\mathrm{EDT}} = \nabla J + k\mathbf{f}_{\mathrm{L}} \tag{5.1}$$

The subscript EDT signifies tether-perturbed dynamics. The Lorentz force, $\mathbf{f}_{\mathrm{L}}$, is normalized by $k = 0.001b^2/(m_{\mathrm{sc}}a^2)$ LU·kg^{-1}km^{-1}TU^{-2} (assuming the force is given in Newtons), where m_{sc} is the spacecraft mass in kilograms, and a and b are the length and time normalization factors, respectively. Figure 5.1 shows the tether and Lorentz force in the synodic frame.

The electrodynamic principle of the Lorentz force occurs where a conductive wire moving in a magnetic field with a plasma ambient has an induced current that reacts with the magnetic field to generate a force. The induced electric field, $\mathbf{E}$, is dependent on the relative velocity between the spacecraft

and the plasma field fixed to Jupiter's magnetic field, $\mathbf{v}_{\mathrm{pl}} = \boldsymbol{\omega}_{\mathrm{J}} \times \mathbf{r}_1$:

$$\mathbf{E} = (\mathbf{v}_{\mathrm{sc}} - \mathbf{v}_{\mathrm{pl}}) \times \mathbf{B}(\mathbf{r}) \tag{5.2}$$

where $\mathbf{B}$ is the local vector of the magnetic field and $\boldsymbol{\omega}_{\mathrm{J}}$ is the angular velocity of Jupiter [90].

The specifics of the current generation and Lorentz force are dependent on the choice of tether. For the purposes of this dissertation, a noninsulated aluminum tape tether with length L and width w is used. The lack of insulation allows the tether itself to collect plasma (eliminating the need for an anodic plasma contactor). Tape geometry improves survivability by reducing micrometeorite impacts to minor holes rather than severing the tether, as may be expected with traditional wire [52]. The dynamical properties of a physical tether such as bowing or twisting are beyond the scope of this work. Averaging the current along the length of the tether and choosing the zero-bias point for maximum current gives the Lorentz force [104]:

$$I_{\mathrm{avg}} = \frac{3}{5} I_0 \tag{5.3}$$

$$I_0 = \frac{4}{3} \left(\frac{w}{\pi} \right) q_{\mathrm{e}} N_{\mathrm{e}} L^{\frac{3}{2}} \sqrt{2 E_{\mathrm{t}} q_{\mathrm{e}} / m_{\mathrm{e}}} \tag{5.4}$$

$$\mathbf{f}_{\mathrm{L}} = I_{\mathrm{avg}} L \left(\hat{\mathbf{u}} \times \mathbf{B} \right) \tag{5.5}$$

The current given by Equation (5.3) is ideal and requires tether control that is not the focus of this work. The current depends on the orientation of the tether with the electric field as $E_{\mathrm{t}} = \mathbf{E} \cdot \hat{\mathbf{u}}$, where the tether direction $\hat{\mathbf{u}}$ is aligned with the tether and points toward the tether cathode. Magnetic field properties are included in Equation (5.4), where q_{e} and m_{e} are the charge and mass of an electron and N_{e} is the local plasma electron density. Note that the Jovian magnetic environment is a complex system requiring several models for a full and accurate representation. As a basic example, the actual magnetic field of Jupiter is offset from Jupiter's center by 0.1 $\mathrm{R_J}$ and tilted by 10.77 deg from the Jupiter rotational plane, resulting in nonautonomous dynamics [29]. Additional complexities include variations in the plasma density and corotating velocity. To simplify the model, it is assumed that the magnetic field is a basic dipole aligned with and in the opposite direction of the rotation of Jupiter. The primary consequence of this simplification is a time-varying error in the magnetic field direction. The magnetic field strength is assumed to follow an inverse cube law $B = M/r_1^3$, where $M = 4.25 \times 10^{-4}\ \mathrm{T} \cdot \mathrm{R_J}^3$. The plasma density is assumed constant at its maximum value from the Divine-Garrett model in Reference [29], for example, $N_{\mathrm{e}} = 3 \times 10^9\ \mathrm{m}^{-3}$ at Io. Figure 5.1 gives an example of the tether and the Lorentz force. As described previously, the Lorentz force $\mathbf{f}_{\mathrm{L}}$ is perpendicular to both the tether orientation $\hat{\mathbf{u}}$ and the local magnetic field $\mathbf{B}$.

Note from Equation (5.4) and Equation (5.5) that the Lorentz force scales linearly with tether width but to the five-halves power with tether

length. If the force is known for a given tether orientation, position, and velocity, one can quickly recalculate the force for different tether sizes using this scaling property. Tether direction has a significant effect on the Lorentz force, both in that the force is limited to be perpendicular to the tether direction and that the force magnitude depends on the dot product E_{t}. From Equation (5.4), tether attitudes that lead to $E_{\mathrm{t}} < 0$ do not produce current or Lorentz force. To reduce the scope of the problem, tether orientation is assumed to be aligned with the position vector, $\hat{\mathbf{u}} = \hat{\mathbf{r}}$, such that the tether is always pointing radially to or away from the center of mass of the primaries, unless stated otherwise. This assumption results in the tether force being at near maximum and also leads to a generally stable tether attitude when far from moons [83]. Note that, while recent higher-fidelity studies indicate dynamic instabilities in tether attitude for inclined orbits, the planar assumptions in this work mitigate that instability [73, 76].

As this work focuses on spacecraft operating near moons, the torque on the tether must be considered. At a minimum, the gravitational torque must be counteracted by a control torque M_{C} to maintain tether orientation. The tether is treated as a rigid dumbbell, with point masses at each end. To simplify the analysis, the tether center of mass is located such that the tether is self-balancing, i.e. there is no Lorentz torque. Given the selection of the zero-bias point for maximum current, the tether center-of-mass location as a fraction of tether length from the cathode end is $\gamma = 0.64286$ [74]. With this selection, the torque on the tether is reduced to the gravitational torque about

the center of mass $\mathbf{M}_{\mathrm{G}}$. Taking into account the distribution of the masses, the normalized gravitational torque per unit mass is given by:

$$\mathbf{M}_{\mathrm{G}} = \mathbf{M}_{\mathrm{G},1} + \mathbf{M}_{\mathrm{G},2} \tag{5.6}$$

$$\mathbf{M}_{\mathrm{G},j} = (-1)^j \left(\gamma - \gamma^2\right) \frac{1000L}{a} \hat{\mathbf{u}} \times \left(-\frac{(1-\mu)}{r_{1j}^3} \mathbf{r}_{1j} - \frac{\mu}{r_{2j}^3} \mathbf{r}_{2j} \right) \tag{5.7}$$

$$\mathbf{r}_{i1} = \mathbf{r}_i - \frac{1000L}{a} (1-\gamma) \hat{\mathbf{u}} \tag{5.8}$$

$$\mathbf{r}_{i2} = \mathbf{r}_i + \frac{1000L}{a} \gamma \hat{\mathbf{u}} \tag{5.9}$$

where $i = 1, 2$ denotes the attracting body, $j = 1, 2$ represents the anode and cathode ends of the tether, respectively, and $\mathbf{r}_{ij}$ is the position vector of the tether ends from the primaries.

The attitude of the tether varies over periodic orbits, requiring an additional control torque $\mathbf{M}_{\mathrm{C}}$. The required torque is found by characterizing the dynamics of the tether attitude. The tether angular momentum is $\mathbf{H}_{\mathrm{G}} = \mathbf{I}_{\mathrm{G}} \boldsymbol{\omega}_{\mathrm{T}}$, where $\mathbf{I}_{\mathrm{G}}$ is the central inertia tensor and $\boldsymbol{\omega}_{\mathrm{T}} = \hat{\mathbf{u}} \times \dot{\hat{\mathbf{u}}} + \omega \hat{\mathbf{u}}$ is the general tether rotation rate in an inertial frame. Noting that the moment of inertia about the tether direction is effectively zero, the tether attitude behaves as:

$$\frac{\mathrm{d}}{\mathrm{d}t} (\mathbf{H}_{\mathrm{G}}) = I_{\mathrm{s}} \left(\hat{\mathbf{u}} \times \ddot{\hat{\mathbf{u}}} \right) = \mathbf{M}_{\mathrm{G}} + \mathbf{M}_{\mathrm{C}} \tag{5.10}$$

$$\ddot{\hat{\mathbf{u}}} = \hat{\mathbf{u}}'' + 2\boldsymbol{\Omega} \times \hat{\mathbf{u}}' + \boldsymbol{\Omega} \times (\boldsymbol{\Omega} \times \hat{\mathbf{u}}) \tag{5.11}$$

where $I_{\mathrm{s}} = (1000L/a)^2 (\gamma - \gamma^2)$ is the normalized principal moment of inertia per unit mass about an axis orthogonal to the tether and $\hat{\mathbf{u}}''$ and $\hat{\mathbf{u}}'$ are time derivatives of the attitude in the rotating frame. As the tether is limited to the xy-plane in this work, all torques and angular accelerations are aligned with the z axis.

For all simulations in this study, a spacecraft mass of 1000 kg with a tether width of 0.01 m is used. Note that the tether thickness is sufficiently smaller than the width such that its effect on the Lorentz force is negligible [12]. The dynamics are considered at Io and Metis on a per case basis to highlight differences deriving from changes in the magnetic field strength and relative plasma velocity. Moons with larger orbital radii, such as Europa, Ganymede, and Callisto, are not considered as the tether forces become small.

5.1.1 Tether Conservative Approximation

The tether force is a function of velocity, making the tether-perturbed problem nonconservative. As the energy change is path dependent, it is unlikely that exact periodic orbits will exist in general, although they have been found under special conditions in another nonconservative system [14, 73]. To transform the equations to a conservative form, the following assumptions are made:

1) The force magnitude is proportional to a constant divided by the spacecraft in-plane distance from system center

2) The force direction is always perpendicular to the position vector, as occurs for tether attitudes parallel to the position vector:

$$\tilde{\mathbf{f}}_{\mathrm{L}} = \frac{\alpha L^{5/2} w}{x^2 + y^2} \left(\hat{\mathbf{z}} \times \mathbf{r} \right) \tag{5.12}$$

The definition of the force approximation is motivated because of its simple associated potential function:

$$V_{\mathrm{L}} = \alpha L^{5/2} w \tan^{-1} \left(\frac{y}{x} \right) \tag{5.13}$$

The constant α is determined using a least-squares fit to the actual Lorentz force calculated over $0.95 < x^2 + y^2 < 1.05$ with zero spacecraft velocity within the rotating frame.

Table 5.1: Lorentz force approximation parameters, distance of unperturbed equilibrium points, and comparative forces at bodies of interest

Parameter	**Europa**	**Io**	**Metis**
a, km/LU	671,100	421,700	128,000
b, s/TU	48,843.88	24,329.32	4,068.64
GM, km^3/s^2	3,202.74	5,959.92	0.002403
r_{L1}, km	13,563	10,466	23.67
r_{L2}, km	13,749	10,642	23.67
N_e, m^{-3}	7.0E7	3.0E9	3.4E8
$\alpha, \mathrm{N} \cdot \mathrm{m}^{-7/2}$	1.8241805E-13	4.6696398E-11	-4.4917363E-10
$\tilde{f}_{\mathrm{L}}$, N	0.0002	0.0461	0.4439

The parameter α is calculated at Metis, Io, and Europa to highlight variations in the Lorentz force as the distance from Jupiter's center increases,

as shown in Table 5.1. A comparison of the approximated force magnitudes is also given for a tether length of 25 km. For Metis, there is a negative value in α due to the body's velocity about Jupiter exceeding the rotational velocity of the magnetic field, resulting in a drag-like force. As the distance from Jupiter is increased, the Lorentz force decreases by orders of magnitude between each body due to the weakening magnetic field strength. This diminishing force strength limits tether utility primarily to within the orbital radius of Ganymede.

There are two main sources of inaccuracies in the approximate model force magnitude. Due to an imperfect line fit, the approximation breaks down as r deviates from near unity. While the Lorentz force is better approximated as $1/r^3$, conservative models that use this approximation introduce errors in the direction of the force; the chosen conservative model always results in a force perpendicular to the radial tether orientation. This direction is the same for both the full and approximate models, resulting in zero error for the force direction. Additional error derives from the force dependency on the velocity of the tether relative to the magnetic field, whereas the approximation assumes constant zero spacecraft velocity. To quantify the error, calculations are made of the actual and approximate tether forces over a grid of radii and tangential velocities v. At each grid point, the spacecraft state in the rotating frame is $\mathbf{X} = [-r \;\; 0 \;\; 0 \;\; 0 \;\; v \;\; 0]^{\mathrm{T}}$.

The analysis is applied at Io to obtain a relative error for the conservative force approximation, shown in Figure 5.2. Negative values indicate the

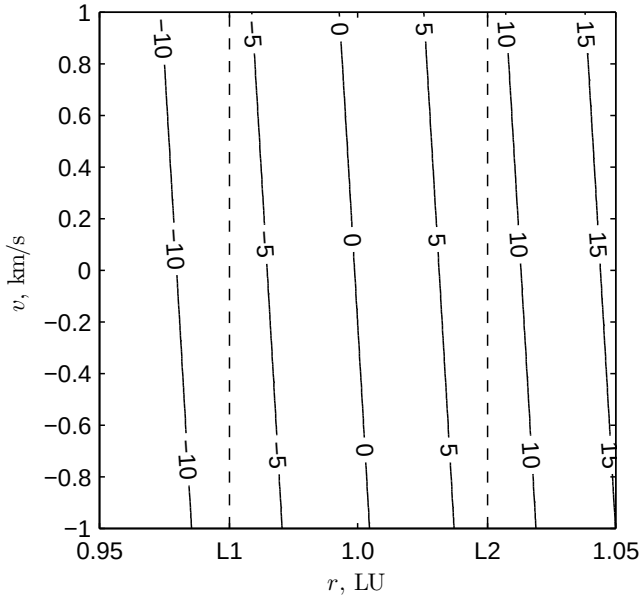

Figure 5.2: Relative error percentage in the force approximation at Io

actual tether force is larger than the conservative model approximation. Because of the size scaling of the force, the relative error is independent of tether length. Looking at the contours, it is clear that differing radii are the largest contributors to errors. Large periodic orbits can go beyond the radii depicted in Figure 5.2, although orbits about the L1 and L2 Lagrange points are expected to remain within 15% error. At the unperturbed L1 and L2 points, the error is at -7.11% and 7.94%, respectively. These are roughly on order with expected errors introduced from assumptions made about the magnetic field strength and simple non-tilted dipole simplifications. The error is comparatively invariant to small changes in orbital velocity, as the spacecraft velocity relative to the plasma is approximately 56 km/s.

The potential function enables a new integral of motion that augments the standard CRTBP Jacobi constant:

$$C = 2\left(J + kV_{\mathrm{L}}\right) - \left(u^2 + v^2 + w^2\right) \tag{5.14}$$

This new integral allows the use of several standard CRTBP analytical tools. It can be used to determine allowed regions of motion through zero-velocity curves, and provides a natural generating parameter for periodic orbit families. The values of the velocity curves are found by setting the velocity in Equation (5.14) to zero and solving for C over a grid of locations.

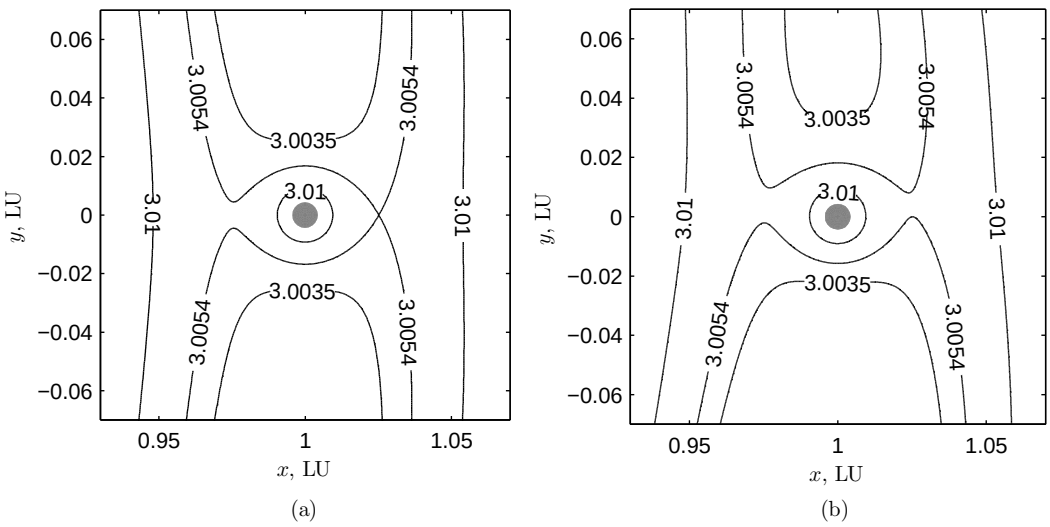

Figure 5.3: Zero-velocity curves near Io for (a) no tether (b) 200 km tether

Plots of zero-velocity curves for the unperturbed and tether-perturbed systems are given in Figure 5.3. The tether curves were made using a 200 km length tether to exaggerate effects. The introduction of the tether leads

to changes as the angle from the Jupiter-Io line varies. In the plots from Figure 5.3, it is seen that relative to the unperturbed case, the tether-perturbed contours of $C = 3.0035$ converge prograde of Io, leading to increased regions of motion. The converse is true retrograde of Io. At $C = 3.0054$, the Hill throats around L1 and L2 are seen, which indicates that travel between Jupiter and Io is possible. For the unperturbed case, the throat at L2 is barely closed. Introduction of the Lorentz force opens this throat, enabling escape from Io via L2. Similar behavior is expected for the throat at L1.

5.2 Equilibrium Points

Equilibrium points are a typical starting point for finding periodic orbits. A primary interest is in the tether-modified equilibrium points within the CRTBP system, particularly the variation of the L1 and L2 points as a function of tether size. The authors of Reference [74] provide a thorough analysis of the stability and dynamics of equilibrium position and attitude for both librating and rotating tethers near the secondary in the Hill model. Zanutto et al. focus on the evolution of the L4 and L5 points with tethers pointing toward the system center of mass, while Bombardelli and Peláez investigate the stability of general artificial equilibrium points [11, 104]. The current work analyzes the equilibrium points in the context of the newly developed conservative model. Qualitative comparisons with the results of the listed references show the dynamical similarity of the conservative model to the full model. In addition, the analysis is made at both Metis and Io to show changes that

arise from differing system mass ratios and switching the sign of the relative velocity in Equation (5.2).

For tether-perturbed equilibrium points to exist, the tether force must exactly cancel the standard three-body acceleration. It is straightforward to show that equilibrium points must satisfy three conditions:

1) Recalling that the Lorentz force is perpendicular to tether attitude, $\ddot{\mathbf{r}} \cdot \hat{\mathbf{r}} = 0$ for the tether force to be aligned with the three-body acceleration.

2) The Lorentz force needs to be opposite the three-body acceleration such that $\ddot{\mathbf{r}} \cdot (\mathbf{r} \times \mathbf{B}) < 0$.

3) For the Lorentz force to exist, $E_{\mathrm{t}} > 0$.

The conservative model assumes the force exists so the third condition is satisfied, and the second condition simplifies to $\alpha \ddot{\mathbf{r}} \cdot (\hat{\mathbf{z}} \times \mathbf{r}) < 0$. A key result of this development is that potential equilibrium locations are solely a function of tether orientation, with tether size determined such that the Lorentz force magnitude cancels the three-body acceleration. For example, when using the radially aligned tether, the equilibrium points in the conservative and nonconservative models will be identical, although the tether sizes will differ due to errors in the Lorentz force magnitude. However, changing the tether orientation in the nonconservative model will result in different equilibrium locations.

As solving for the condition $\ddot{\mathbf{r}} \cdot \hat{\mathbf{r}} = 0$ is analytically challenging, a nu-

merical approach is used to find the tether-perturbed equilibrium points. The method uses a continuation approach to get modified equilibrium points L1* and L2* as functions of tether length. Starting at an unperturbed Lagrange point as an initial guess along with an initially small tether size, a differential corrector is used to iterate on the spacecraft position until a perturbed equilibrium position is found. The tether length is then increased and the differential corrector rerun to obtain a new equilibrium point using the previous point as the initial guess. Continuation methods generate further equilibrium points until they impact the surface of the moon or the tether decreases back to zero length.

The differential corrector uses derivatives of the total tether-perturbed acceleration with respect to position. These derivatives are obtained using the numerical complex step approach that is proven to be accurate to machine precision [64]. The Newton update step is calculated using the following equation:

$$d\mathbf{r}_{\mathrm{eq}} = -\left(\frac{\partial \ddot{\mathbf{r}}_{\mathrm{EDT}}}{\partial \mathbf{r}}\right)^{-1} \ddot{\mathbf{r}}_{\mathrm{EDT}} \tag{5.15}$$

The update is iterated until the total acceleration magnitude is near zero within some small tolerance. Since the starting locations are the known L1 and L2 points, the initial guesses for a small perturbation in tether size are sufficiently close for the simple differential corrector to converge.

In Figure 5.4, the evolution of the equilibrium positions in the xy-plane

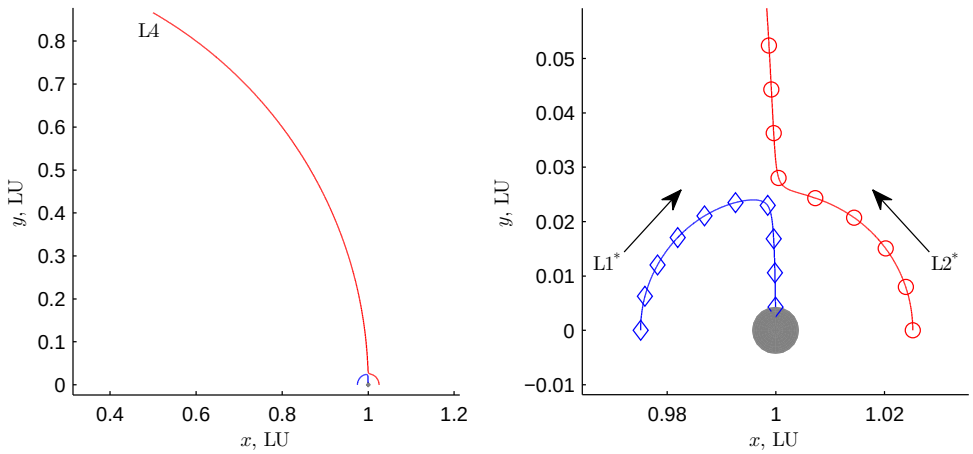

Figure 5.4: Tether-modified L1* (diamond) and L2* (circle) equilibrium coordinates at Io in the xy-plane. The L2* curve travels along Io's orbital radius ending at the unperturbed L4 point

at Io is plotted, while Figure 5.5 gives the x coordinate as a function of tether length. Recalling the start at the unperturbed L1 and L2 points with $y = 0$, the equilibrium points shift toward positive y as tether length increases. Larger tethers lead to curving in front of the leading side of Io at nearly constant distance from the moon. The perturbed L1* points eventually shift down to the surface of Io and impact at a maximum tether length of 1718 km. The L2* points conversely travel away from Io as the tether length decreases from a maximum of 410 km. From Figure 5.4, it can be seen that the L2* curve nearly follows Io's orbital radius, ending at the standard L4 point with zero tether length. Beyond this point, the force direction of the radial tether is incapable of canceling the three-body acceleration. An important result seen

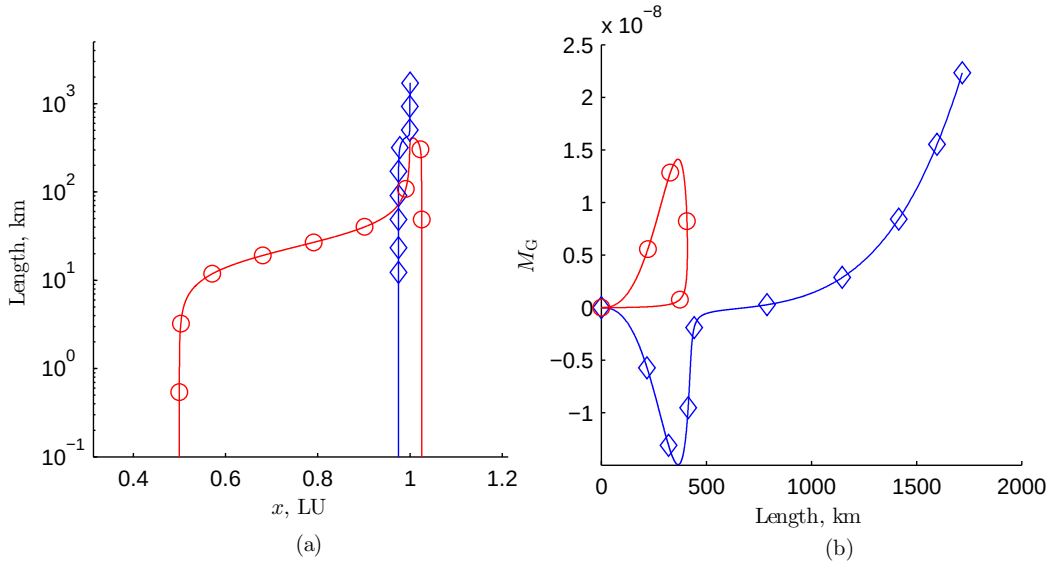

Figure 5.5: (a) Tether-perturbed x equilibria at Io (b) Normalized gravitational torque M_{G}, on the tether

in Figure 5.5 is that the L2* curve has two equilibrium points for a given tether length. This non-uniqueness leads to interesting dynamics for some periodic orbits, which is explored in the succeeding section.

The gravitational torque on the tether center of mass is shown in plot (b) of Figure 5.5 as a function of the tether length. Starting from the unperturbed points at zero length, the torque for both L1* and L2* rapidly grows with tether length up to a local maximum of approximately ±1.5E-8 $\mathrm{LU}^2/\mathrm{TU}^2$ (4.51 kN·m for the 1000 kg spacecraft) at $L = 370$ km. As the L1* points approach Io's surface, the torque rapidly decreases, goes through a point of zero torque, and then grows in the opposite direction due to the large tether lengths and increasing proximity to Io. Conversely, the torque for the

L2* points rapidly decreases and stays relatively small, as expected for radially pointing tethers located far from both bodies.

Note that the evolutions of these points are similar to results from Reference [74] in that the points curve around the front of the primary and then both down to and away from the surface. Initial similarity is expected as both works start at the unperturbed equilibrium points. However, the equilibrium locations in this work follow a roughly circular curve around Io, whereas those from Reference [74] follow an ellipse-like shape that ultimately leads Io approximately twice as far away. The differences arise from the facts that a) those authors included tether attitude equilibrium rather than a general heuristic and b) they developed the analysis in the Hill model of motion.

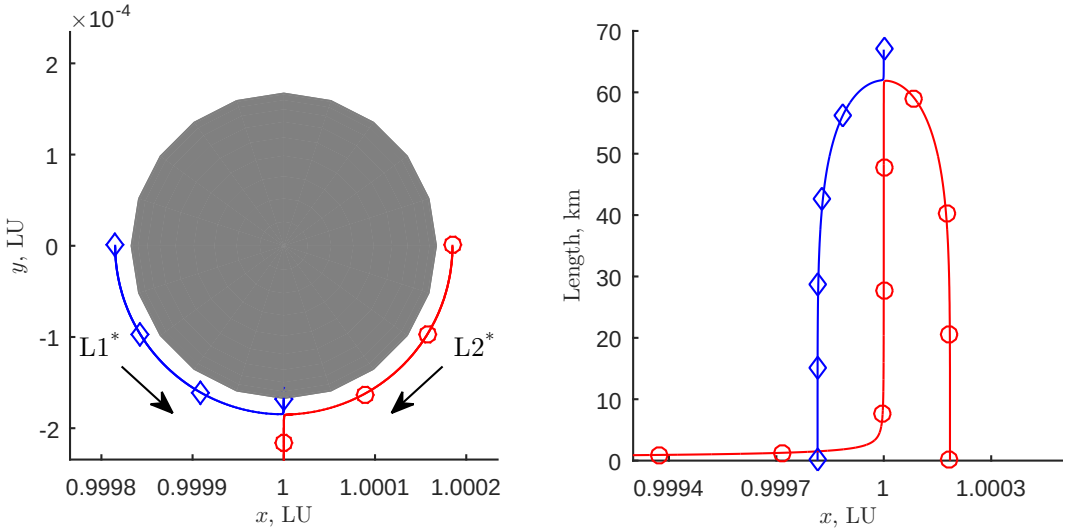

Figure 5.6: Metis L1* (diamond) and L2* (circle) equilibrium coordinates in the xy-plane, and as function of tether length

Next the dynamics at the inner moonlet Metis are considered. The

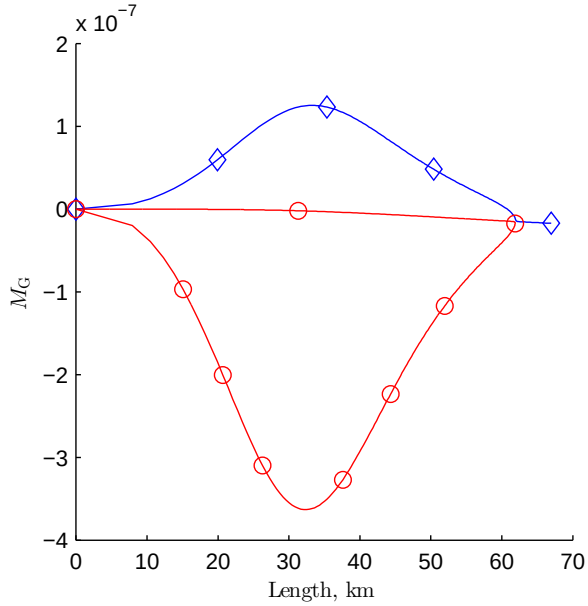

Figure 5.7: Normalized gravitational torque per unit mass, in LU^2/TU^2, of the $L1^*$ (diamond) and $L2^*$ (circle) tether-modified equilibrium points at Metis

moonlet has less mass and is in a stronger region of Jupiter's magnetic field, leading to more effective tether forces and smaller tether lengths. Plots are again made to show the equilibrium points, seen in Figure 5.6. As Metis is only 1.83 R_J from Jupiter, its orbital velocity is greater than the rotating magnetic field; thus, the direction of the tether Lorentz force is switched from that at Io, causing the equilibrium points to shift toward the trailing edge of Metis. Note that the figure does not include the full $L2^*$ curve, which extends out to the L5 point. The stronger Lorentz force allows for significantly shorter tether lengths, with a 60 km tether capable of equilibrium directly trailing the moonlet. This difference in force magnitudes allows for unique possibilities including placing the spacecraft in a position where Metis itself functions as

a partial radiation shield from Jupiter [40]. The gravitational torque is given in Figure 5.7, where it follows a similar evolution as it did at Io. The peak normalized torque is -3.63E-7 LU^2/TU^2 at a tether length of 32.5 km, which converts to 360 kN·m, two orders of magnitude larger than the peak torque for Io.

It is important to note that the unperturbed equilibrium locations are within 2.2 km of the surface of Metis. This close proximity, combined with the radial tether attitude, results in tether lengths that impact Metis. Lengths between 2.17 and 41.5 km result in impacts. These nonphysical locations are plotted for completeness, as the tether length requirements can be scaled using different model parameters such as tether width and density, enabling shorter tether lengths. However, feasible limits on the tether sizing imply that there will always be some impacting equilibrium points. Another practical concern (aside from the ignored nonspherical gravity and uncertainties in the dynamics) is that the average radius of the moonlet is only 21.5 km, meaning the tether length is a significant fraction of the moonlet's circumference.

5.3 Tether-Modified Periodic Orbits

The evolution of the tether-perturbed $L1^*$ and $L2^*$ Lyapunov orbits is a natural extension to equilibrium positions. Two options are explored for finding initial periodic orbits:

1) Starting from known unperturbed orbits

2) Starting from very small orbits about the perturbed equilibrium points

These initial orbits are then expanded into families using continuation methods. The families are naturally characterized by both their integral of motion and the tether size. To limit the scope of the work, only a limited range of the variables is considered by holding one constant while allowing the others to vary. Because of the close proximity of the equilibrium points to Metis, the Lyapunov orbits are generally limited to a small range with little variation, and so only orbits at Io are considered here.

5.3.1 Periodic Orbit Generation

The existence of the tether force causes the CRTBP equations of motion to lose both xy-plane and x-axis symmetry, preventing the common approach of targeting perpendicular planar crossings to find periodic L1 and L2 orbits. Therefore, a full-dimensioned targeting algorithm is implemented to search for periodic orbits [88]. Although the focus of this work is on planar orbits, the algorithm is developed including out-of-plane components for completeness. In brief, the method starts with choosing one fixed variable of the position state (x_0, y_0, z_0) to enable checking for repeats of the initial state $(\mathbf{r}_0, \mathbf{v}_0)$. Typical selections are crossings of the xy-, xz-, or yz- planes. Again, the Lorentz force breaks the system symmetry so these crossing selections are chosen for convenience; the actual trajectory is generally not perpendicular to the crossing plane. As the final state is calculated at this crossing, the fixed

variable is automatically satisfied and can be ignored, leading to a reduced state vector $\boldsymbol{\xi}$. Consider a practical example: if $x_0 = 0$ is the fixed state, then the crossing plane is the yz plane. The value of x at this crossing matches the initial state and does not need correction, so the state is removed from the full state vector to get $\boldsymbol{\xi}$. A constraint vector $\mathbf{K}$ is introduced to enforce that the trajectory returns to its initial state, with an optional constraint to target specific energy levels C^*:

$$\mathbf{K} = \begin{bmatrix} \boldsymbol{\xi}_{\mathrm{T}} - \boldsymbol{\xi}_0 \\ C - C^* \end{bmatrix} \tag{5.16}$$

where $\boldsymbol{\xi}_{\mathrm{T}}$ is the constraint vector evaluated at the cutting plane intersection. Given an initial $\boldsymbol{\xi}_0$ that yields nonzero $\mathbf{K}$, an update to the state, $\Delta\boldsymbol{\xi}_0$, is computed through the solution to the linear equation [88]:

$$\frac{d\mathbf{K}}{d\boldsymbol{\xi}_0}\Delta\boldsymbol{\xi}_0 = -\mathbf{K} \tag{5.17}$$

where:

$$\frac{d\mathbf{K}}{d\boldsymbol{\xi}_0} = \begin{bmatrix} d\boldsymbol{\xi}_{\mathrm{T}}/d\boldsymbol{\xi}_0 - \mathbf{I}_{5\times5} \\ dC/\boldsymbol{\xi}_0 \end{bmatrix}_{6\times5} \tag{5.18}$$

$$\frac{d\boldsymbol{\xi}_{\mathrm{T}}}{d\boldsymbol{\xi}_0} = \frac{\partial\boldsymbol{\xi}_{\mathrm{T}}}{\partial\boldsymbol{\xi}_0} + \frac{\partial\boldsymbol{\xi}_{\mathrm{T}}}{\partial T}\frac{\partial T}{\partial\boldsymbol{\xi}_0} \tag{5.19}$$

An important attribute of the algorithm is its use of singular value decomposition to solve Equation (5.17), allowing it to handle over- or underconstrained

problems as well as singularities.

The algorithm is used iteratively with continuation methods to generate families of orbits characterized by either tether length or the Jacobi constant. In general, the orbits are found using planar x-axis crossings. Because of the asymmetrical tether-perturbed equations of motion, a subset of the periodic orbits does not cross the x-axis. When $y = 0$ fails to occur, the crossing plane is changed to the average x value over the full period of the previously converged periodic orbit. Because of the change in the crossing variable, discontinues initially appear in the characteristic curves of the orbital families. To enforce continuous values, the initial states of the periodic orbit are integrated forward until $u_0 = 0$. The state at this point then becomes the new initial state. As all periodic orbits have a minimum of two locations where $u_0 = 0$, a proximity check ensures that states are sufficiently close between orbits within the family to ensure continuous characteristic curves. Note that the selection of $u_0 = 0$ is done solely for the purpose of plotting continuous characteristic curves and is not indicative of symmetric, perpendicular crossings seen in unperturbed periodic orbits.

To obtain $\partial \boldsymbol{\xi}_{\mathrm{T}} / \partial \boldsymbol{\xi}_0$, the convenient and accurate numerical complex step method is again used [64]. For each periodic orbit, the state transition matrix over one period, the monodromy matrix, is calculated. The eigenvalues of this matrix indicate the stability indices of the periodic orbit using:

$$b_{\mathrm{i}} = \lambda_{\mathrm{i}} + 1/\lambda_{\mathrm{i}} \tag{5.20}$$

As the eigenvalues occur in reciprocal pairs, only three unique stability indices exist [14]. Additionally, because the system is autonomous, one index is trivial as it is always 2, representing a perturbation along the orbit trajectory. For linear stability, the remaining two indices must be real and have magnitudes less than 2; otherwise, the orbit is unstable with larger magnitudes representing greater instability. For planar periodic orbits, the stability indices are denoted as vertical or horizontal, b_{v} and b_{h}, respectively. The horizontal indices correspond to perturbations within the orbit plane, while the vertical indices are out-of-plane deviations [39].

5.3.2 Variable Length Families

The effects of varying the tether length are analyzed while holding C constant for the perturbed Lyapunov orbits. For both L1 and L2, a representative starting orbit is selected from the unperturbed Lyapunov families. The only criteria used for initial orbit selection is a general consideration of the approach distance to Io. The initial L1 orbit has $C = 3.0025008$ with a period of 3.5872 TU (24.24 h), while the L2 orbit starts with $C = 3.0024488$ and has a period of 3.6613 TU (24.74 h). Each periodic orbit is then extended into a family by increasing the tether length and converging the differential corrector, while maintaining a fixed Jacobi constant. Continuing the family requires traversing reflections where the direction of the generating parameter changes. At these reflections, the continuation method temporarily varies x instead of length for traversing to the next member of the family. The L2 family ends

with an impact at the surface of Io, while the L1 family is continued until convergence becomes difficult without using unreasonably small steps.

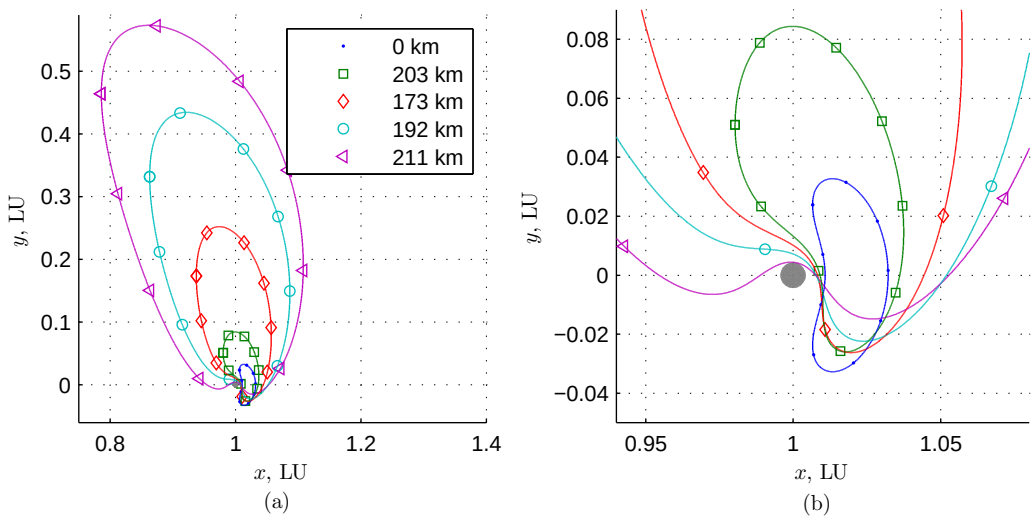

Figure 5.8: Evolution of modified L2 Lyapunov orbits at constant C with (a) full view and (b) detail view. Legend indicates tether length

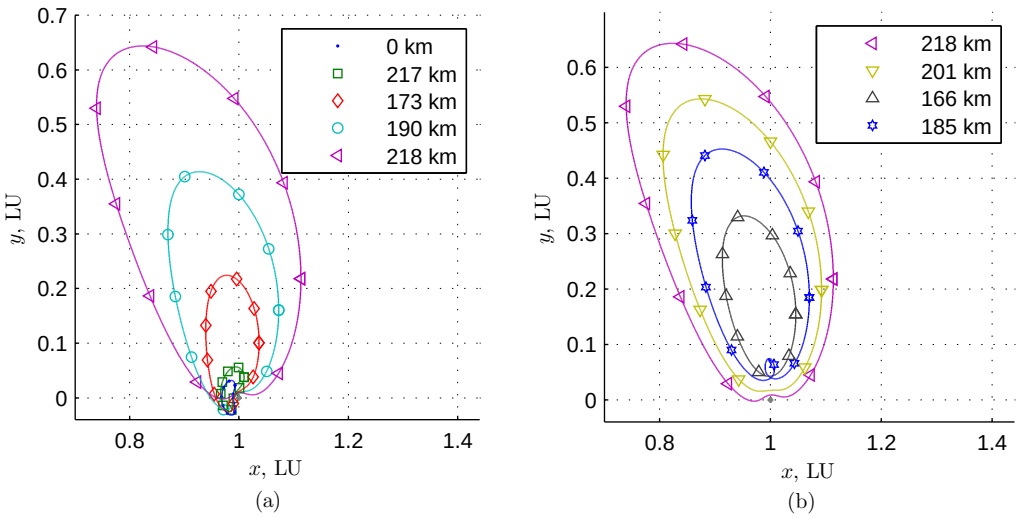

Figure 5.9: Evolution of modified L1 Lyapunov orbits at constant C from (a) set 1 and (b) set 2. Legend indicates tether length.

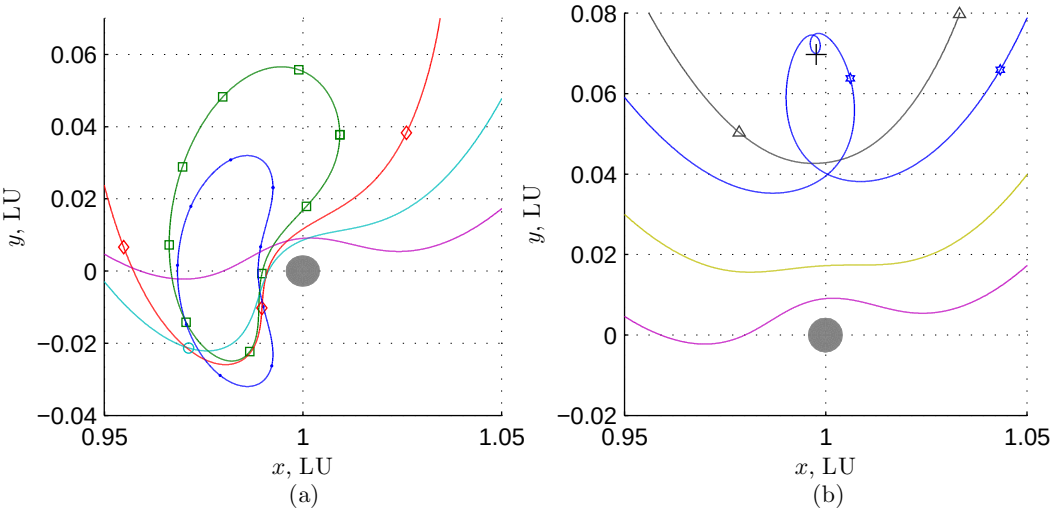

Figure 5.10: Detailed view of the modified L1 Lyapunov family at constant C for (a) set 1 and (b) set 2. The plus marker indicates the leading L2* equilibrium point at $L = 185$ km

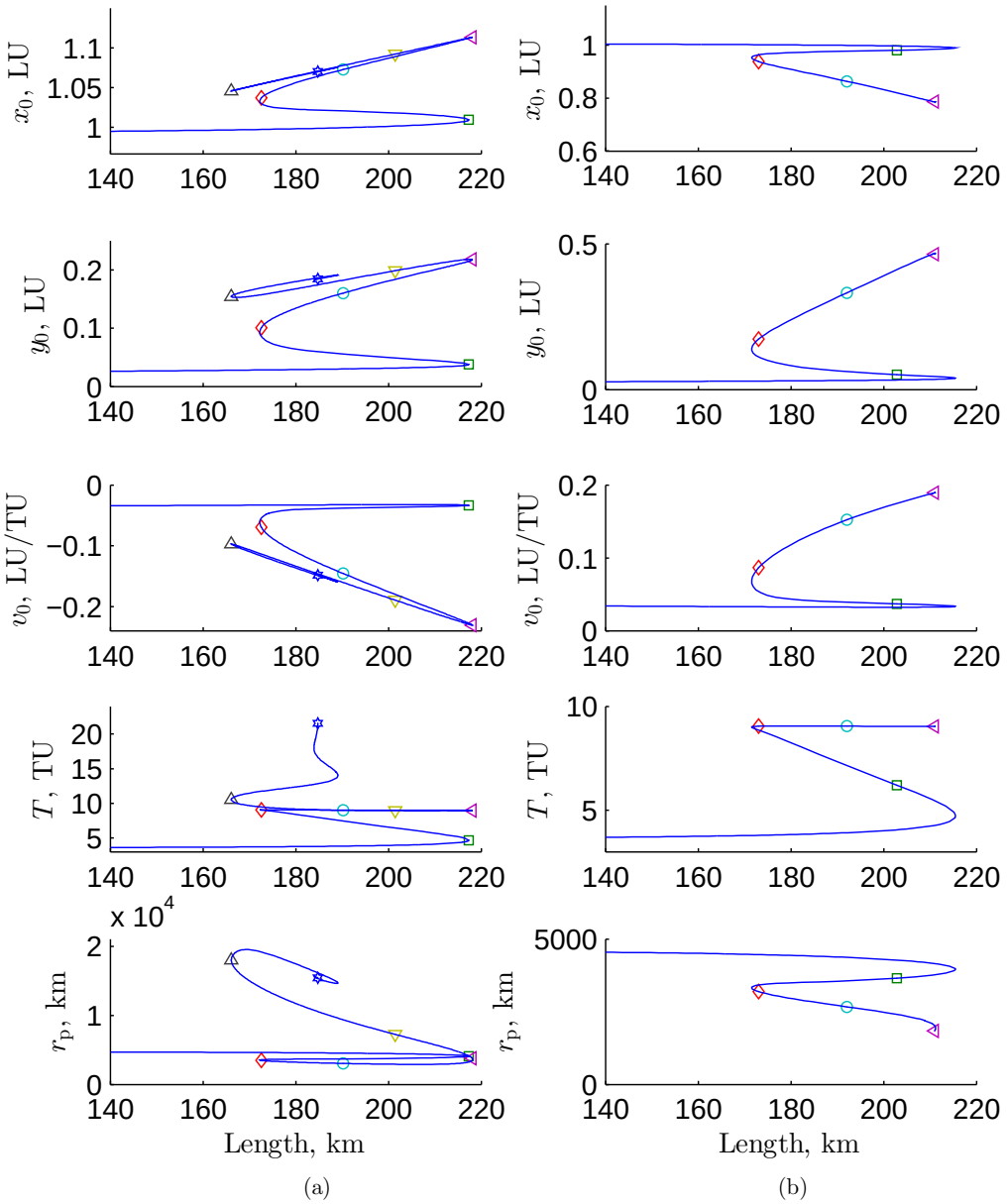

Figure 5.11: Characteristic curves at constant C for (a) L1 family (b) L2 family

Figure 5.8 plots a few of the orbits from the L2 family, including the initial unperturbed orbit and the final orbit before impact. Because of the choice of different energy levels between the L1 and L2 families, the L1 family does not impact Io and has a larger range of orbits. The L1 family is plotted in Figure 5.9 and Figure 5.10, where two plots are used for clarity. The plots labeled (a) show orbits until the family achieves its maximum distance from Io (set 1), while the orbits after this point (set 2) are shown in the (b) plots. Figure 5.11 gives the characteristic curves for both modified L1 and L2 families, with markers correlating to the orbits plotted in the trajectory figures. The curves show the nonzero initial states, the orbit period, and the orbit closest approach. Note that tether lengths below 150 km have minimal variation and have been excluded from the plot to clearly show regions of rapid change.

Starting with a qualitative analysis of the orbits for both the L1 and L2 families, it is seen that increasing tether length causes the orbits to shift forward and slightly rotate about Io. It is clear that the orbits are not symmetric about the x-axis as there is bulging on the leading side of the moon due to the positive y direction of the Lorentz force. For small orbits that remain within a few Io radii of the moon, the L1 and L2 families are near reflections about Io. With larger orbits, the trajectories of both families tend to follow the curve of Io's orbit about Jupiter, as they effectively depart from and re-encounter Io at non-resonant intervals. The last orbit found in the L1 family at a length of 185 km (denoted with hexagram markers) is of particular interest in that half of its orbit time ($\approx$88 h) is spent in a loop with a smaller inner loop near

its closest approach. This looping structure is clearly visible in plot (b) of Figure 5.10. The plus-shaped marker shows the L2* equilibrium point that leads Io when tether length is at 185 km. The proximity of the loop about this marker indicates that the slow looping is due to dynamics influenced by that equilibrium point. Distances from Io during this looping time range from 15,470 to 31,630 km.

Figure 5.11 shows the characteristic curves for the families, with markers correlating to the orbits in Figures 5.8 – 5.10. The characteristic curves show that the families are initially near-invariant to changes in tether length. It is only after lengths exceeding 100 km that notable differences occur; however, these changes are small relative to the variations that start after the first reflection at a 217 km tether length. The L2 curves go through a second reflection before impacting, while the L1 curves go through seven reflections before the corrector encounters convergence difficulties. Each reflection occurs at smaller changes in tether length, which can be seen clearest in the plot of the L1 orbital period. The change in tether length between the last two reflections is only 1 km. It is this shrinking reflection interval that leads to difficulty in converging to new periodic orbits as the step sizes to enable convergence become infeasibly small. While alternative algorithms such as pseudo-arc-length or multishooting methods could help mitigate the convergence issues, the orbit itself becomes effectively invariant to the continuation process, making the benefit of further continuation minimal.

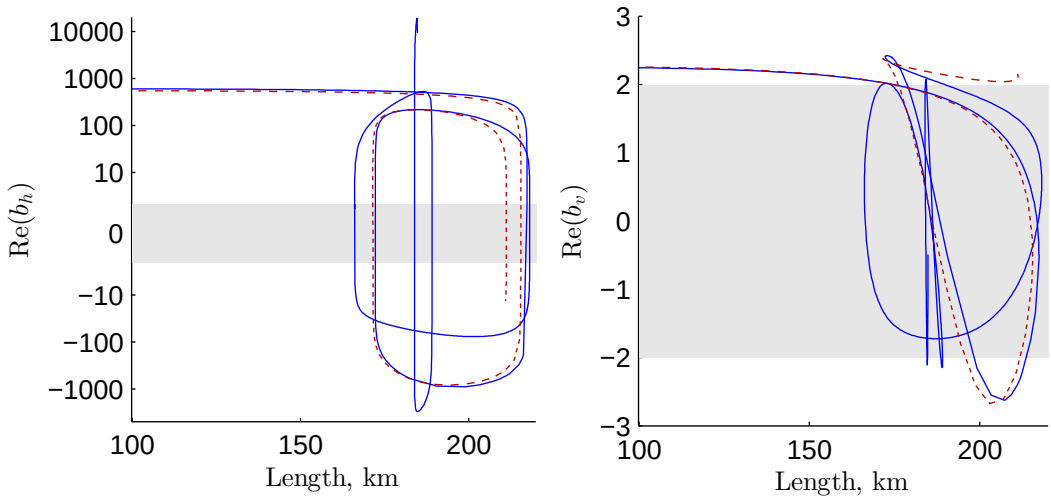

Figure 5.12: Horizontal and vertical stability indices for the constant C L1 (solid) and L2 (dashed) families

Consider the stability indices for the Lyapunov families at constant C given by Figure 5.12, where the indices have been separated by the horizontal (b_{h}) and vertical (b_{v}) grouping, and the gray region indicates stability. Similar to the characteristic curves, the tether length has little effect on the stability indices before 100 km; these values are ignored in favor of regions where rapid variation occurs. Both indices are typically real valued only, and instances in which imaginary components appear are therefore likely due to numerical error as the imaginary magnitudes are 10^{-14} or smaller. Comparing the two families, it is seen that both indices tend to follow the same general shape, although the qualitative differences increase through the family continuation process. The effect is most noticeable after the second reflection where the L2 vertical indices diverge from the L1 line as the L2 orbits approach and

ultimately impact Io.

With each successive reflection, the indices become increasingly sensitive to changes in tether length to the point that they appear to be vertical lines. The indices for out-of-plane perturbations consistently remain within or just beyond stability. Horizontal stability is atypical and usually occurs during a reflection where the indices are rapidly changing from positive to negative values. As mentioned, orbits with real-valued indices in which the magnitudes of both the vertical and horizontal indices are less than the critical value of 2 are dynamically stable. Because of the sensitivity of the indices to changes in tether length after several reflections, it becomes numerically difficult to precisely find stable orbits; however, they do exist. Examples of these elusive stable orbits that occur during the first reflection for both families can be seen in Figure 5.8 and Figure 5.9. These are the second smallest orbits plotted and are indicated by the square makers. The orbits occur with a tether length just above 200 km and loosely resemble distorted versions of the unperturbed Lyapunov orbits, with bulges on the leading side of Io. No other stable examples exist for the L2 family in the orbits generated here. The L1 family has a limited number of additional stable orbits. One such stable orbit is included in the right plot of Figure 5.9, marked with upward-pointing triangles. The orbit leads Io in a simple ellipse-like shape far from the Jovian moon with a closest approach of 18,000 km from the moon center. The stability of the discussed orbits is verified by propagating over 100 orbital periods with no notable departures.

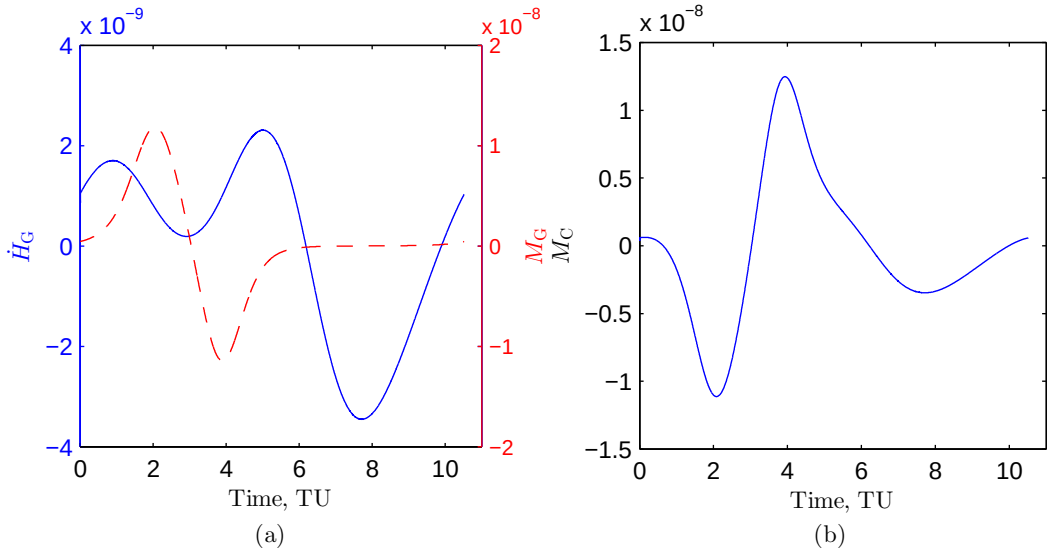

Figure 5.13: Normalized torques on the tether during a stable periodic orbit. (a) Required angular acceleration and experienced gravitational torque (b) Control torque to achieve $\dot{H}_{\mathrm{G}}$

As the scope of analyzing the attitude control of every orbit is infeasible, only one analysis is made as a demonstration. The orbit selected is the stable orbit denoted by the upward-pointing triangle markers in Figure 5.9, as the stability makes it an attractive option for mission design. The gravitational torque over the orbit period is calculated using Equations (5.6 – 5.9), along with $\ddot{\hat{\mathbf{u}}}$, where $\hat{\mathbf{u}}'$ and $\hat{\mathbf{u}}''$ are approximated using finite differencing on $\mathbf{u}$. The control torque $\mathbf{M}_{\mathrm{C}}$ required to maintain the orbit attitude is then calculated with Equation (5.10). In plot (a) of Figure 5.13, the total angular acceleration required to fly the periodic orbit (i.e., the left-hand side of Equation (5.10)) (solid) is compared to the gravitational torque (dash). The difference between these values gives the normalized control torque, shown in plot (b). It is

clear that the gravitational torque dominates the control, as it is an order of magnitude larger than the $\dot{H}_{\mathrm{G}}$ term. Converting to SI units for the 1000 kg spacecraft, there is a peak control torque of 3.75 kN·m.

5.3.3 Varying Lorentz-Perturbed Jacobi Integral of Motion

The Jacobi constant provides a second parameter for classifying the periodic orbits. To keep the scope manageable, an in-depth analysis is considered at only two constant tether lengths for both L1 and L2 families. The first case uses a 150 km tether, while the second is at 200 km. While families at smaller lengths were generated, they do not sufficiently differ from either the 150 km or unperturbed families to be dynamically interesting.

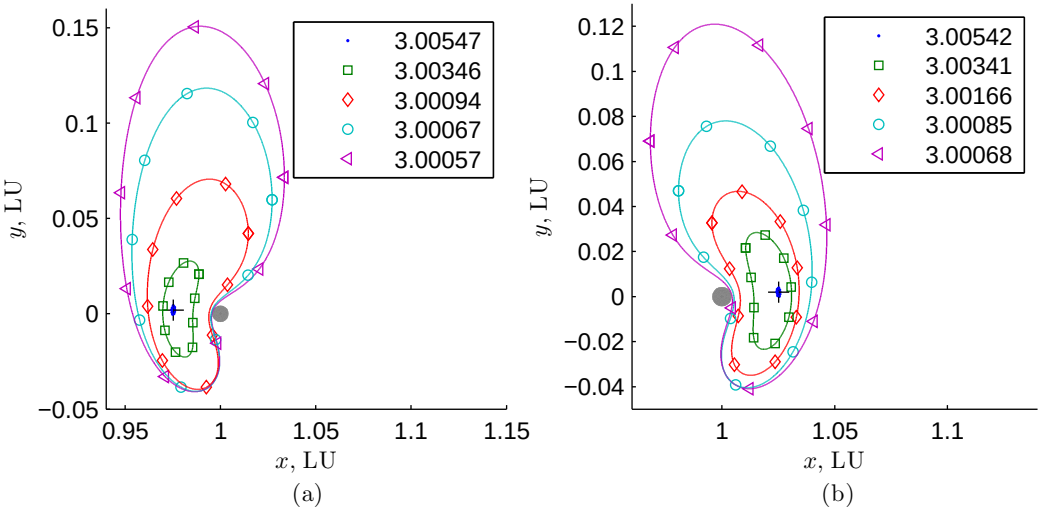

Figure 5.14: Lyapunov orbits at tether length of 150 km for (a) L1 family (b) L2 family

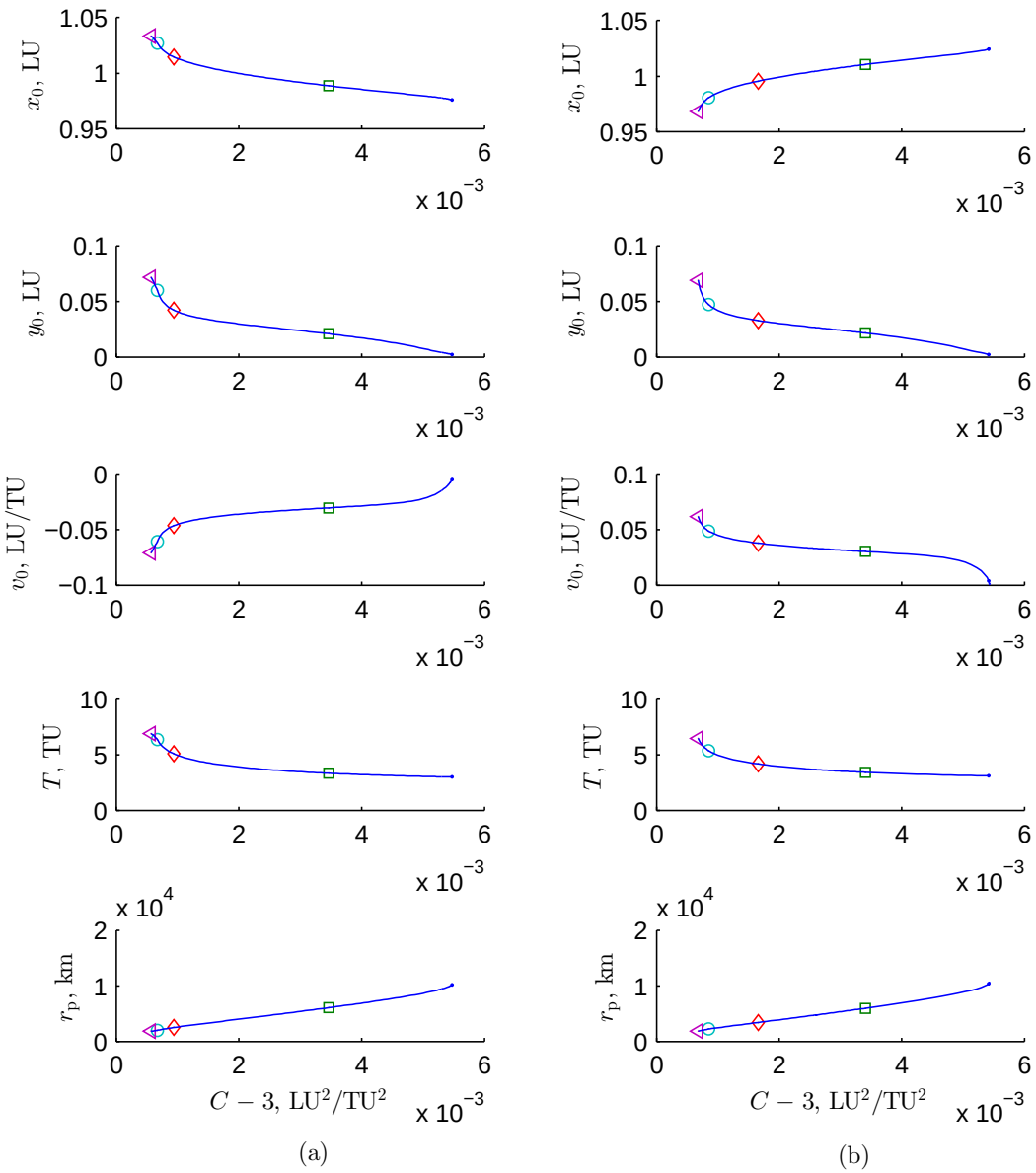

Figure 5.15: Characteristic curves at tether length 150 km for (a) L1 family (b) L2 family. Markers correspond to orbits in Figure 5.14

Several orbits from both the L1 and L2 families are given in Figure 5.14, where the legend shows C values, while Figure 5.15 plots the characteristic curves. As expected, the families start as small orbits about the perturbed equilibrium points (indicated by plus markers) that have been shifted toward the leading side of Io due to tether forces. These initial orbits are at the maximum C of 3.0054928 and 3.0054301 for L1 and L2, respectively. The orbit size increases as C is decreased, with initial orbits closely resembling typical Lyapunov orbits. At the end of the families, the orbits exhibit bulging on the leading side of Io. The sensitivities of the families to changes in C increase as the families are continued with most of the changes occurring over a small subinterval of the total range considered. While this sensitivity is indicative of an upcoming reflection, both families impact Io and are considered complete for the purposes of this work.

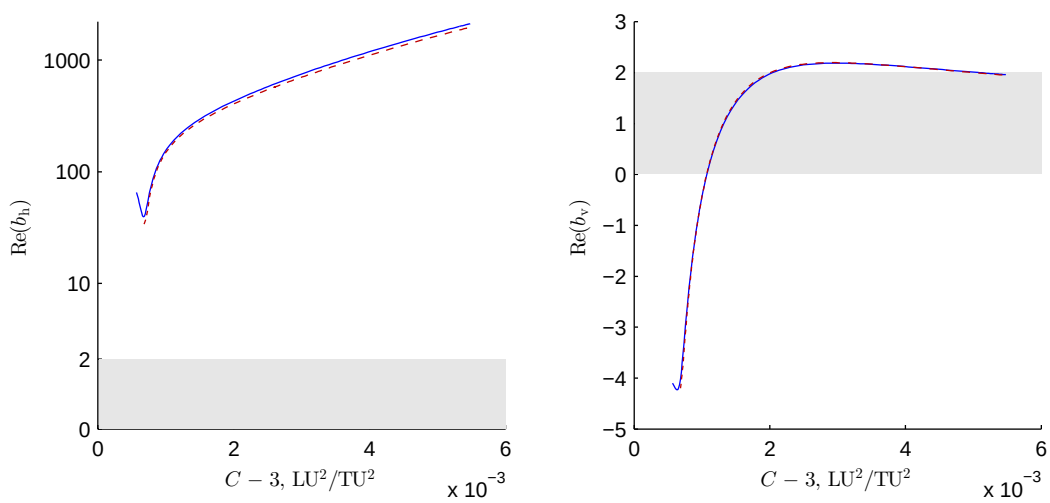

Figure 5.16: Horizontal and vertical stability for L1 (solid) and L2 (dash) families with 150 km tether length. Gray areas indicate stable regions

The stability indices of the families at a constant tether length of 150 km are shown in Figure 5.16. The imaginary components of the indices are again negligibly small and are ignored. Note that the curves for the vertical indices are nearly identical, making visual differentiation between the L1 and L2 families difficult. The horizontal indices have a minimum value of 34, well above the critical value, indicating that no orbits within the families are stable. Vertical stability alternates through the families with a total of three crossings of the critical value. These crossings indicate that there are at least two simple and one period-doubling bifurcations of the periodic orbit that can be followed to find additional periodic orbit families.

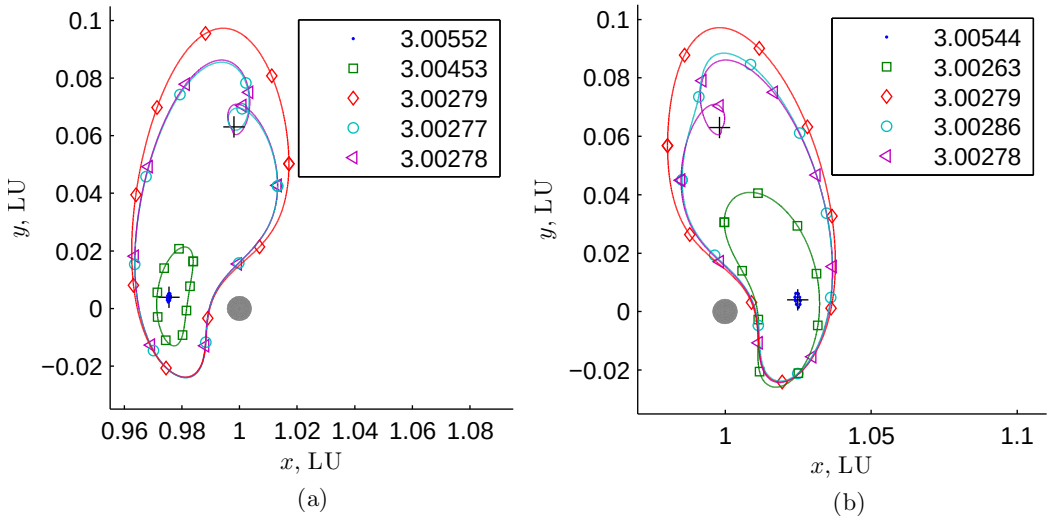

Figure 5.17: Periodic orbits with a 200 km tether length for the (a) L1 family (b) L2 family. Legend indicates C energy levels, the plus markers show equilibrium points for the 200 km tether

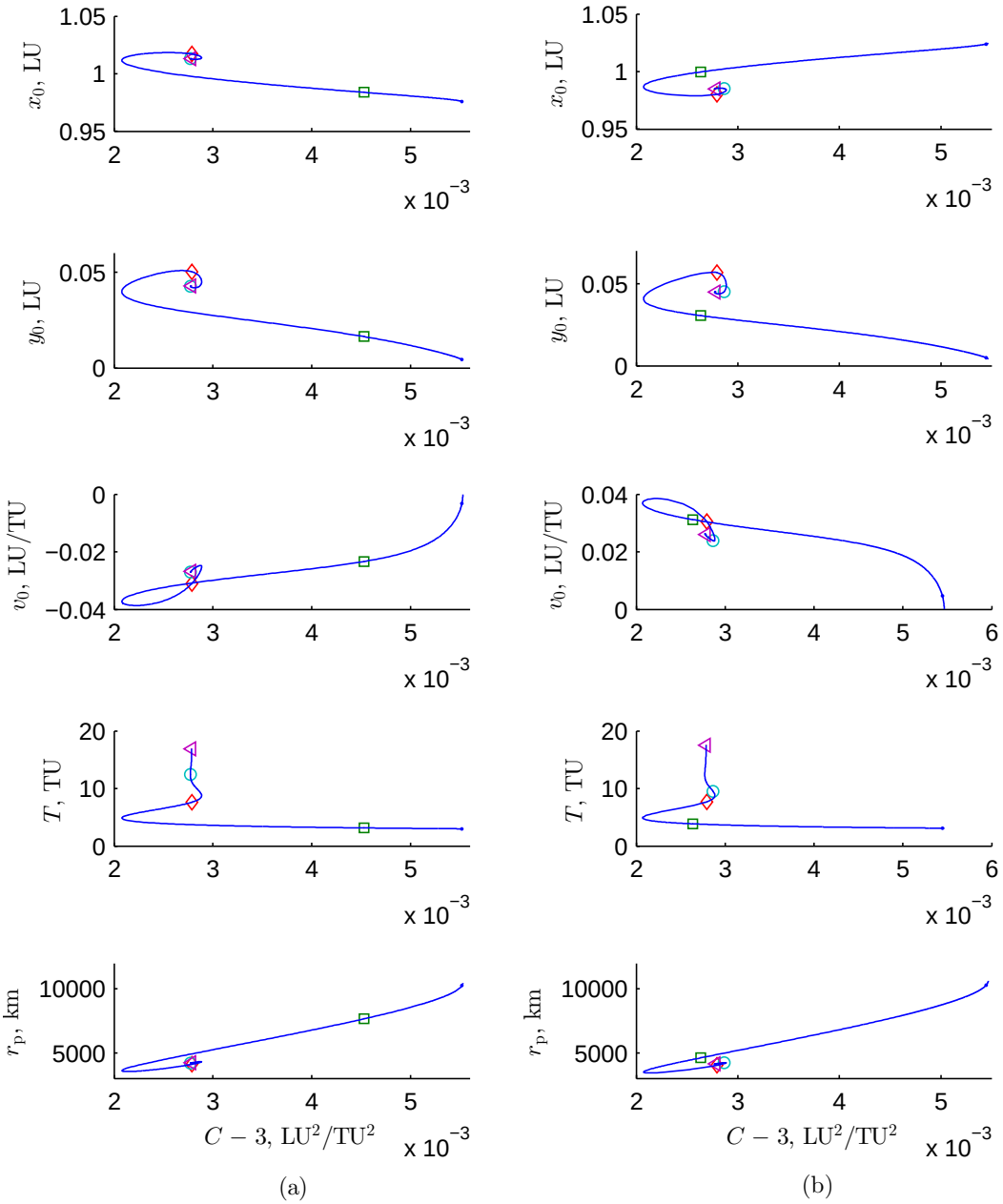

Figure 5.18: Characteristic curves at tether length 200 km for (a) L1 family (b) L2 family. Markers indicate trajectories from Figure 5.17

Orbits from the L1 and L2 families calculated using a constant 200 km length tether are given in Figure 5.17. Neither family experiences an impact with Io, resulting in the continuation process ending after a series of increasingly frequent reflections similar to the length-varying families. The orbits found before the first reflection are qualitatively similar to those found at the 150 km length. Beyond the first reflection, the orbits continue to grow up to a maximum size. As the families continue, the orbits reduce in size before developing fractal-like looping behavior similar to what was observed for the length-varying families. These loops again exhibit hovering-like motion near the Io-leading $L2^*$ equilibrium point. All the characteristic curves additionally have fractal-like spiraling over successive reflections with the exception of periodic time, which monotonically increases.

The orbits shown from the L1 family highlight the small orbit about the tether-modified equilibrium point, the orbit with maximum Io distance (diamond markers), the last orbit found in the family (triangles), and two stable orbits (squares and circles). As the L2 family is nearly identical to the L1 family, the plot does not include the stable orbits. Instead, an orbit with similarities to a rotated and shifted standard Lyapunov orbit (squares) is plotted. Two of the orbits (marked by circles and triangles) in the L2 family are shown specifically to highlight that changes to orbital shape become predominantly limited to the looping structure.

Figure 5.18 shows the evolution of the nonzero initial conditions along with the orbit periodic time and the orbits' closest approach values. The sta-

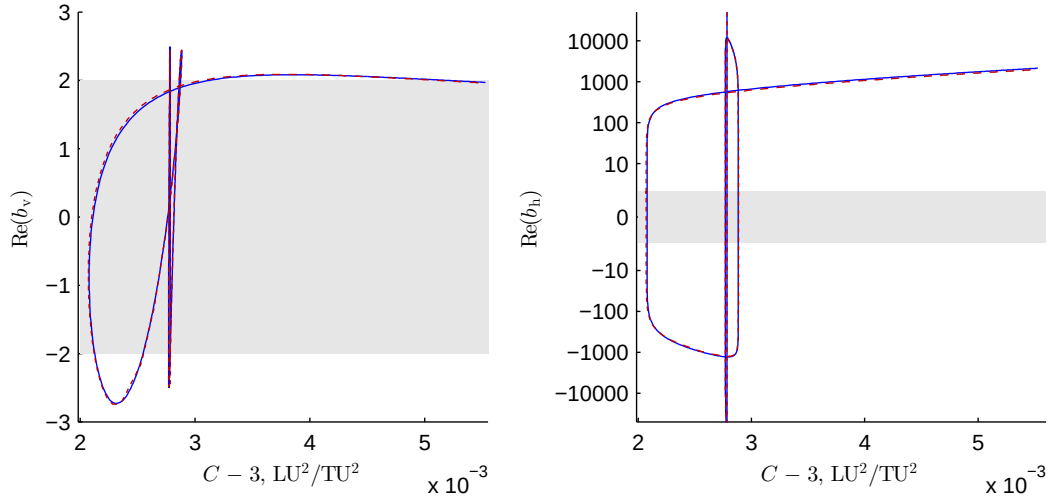

Figure 5.19: Horizontal and vertical stability indices for L1 (solid) and L2 (dashed) orbits with a constant tether length of 200 km. Gray indicates the stable region

bility indices are given in Figure 5.19, where again there are no significant imaginary components. Note that, for improved visibility, the horizontal indices plot has been cropped to exclude significant spikes of -92,000 and 376,000 that occur over the final two reflections of the families. It is clear that both vertical and horizontal indices go through the stable region, indicating the existence of stable orbits. As was seen for the variable length families, the horizontal indices are highly sensitive to changes to C during these stability transitions.

New orbits can be found directly from the perturbed equilibrium points in addition to the orbits found from unperturbed Lyapunov orbits. An additional orbital family is found to demonstrate the potential for this approach. The starting equilibrium point chosen is the perturbed L1* point with a tether

length of 500 km, at $(x, y) = (0.9993311, 0.0200962)$ LU. A perturbation of 1 km is made in the x direction from the equilibrium point, and trial and error for u_0 and v_0 leads to an initial near-periodic orbit. The differential corrector then drives the orbit to the periodic conditions. The continuation method generates a full family of orbits using the Jacobi constant as the generating parameter.

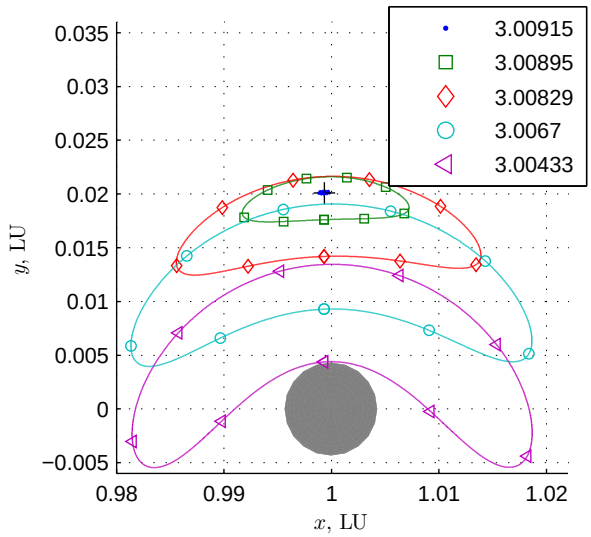

Figure 5.20: Orbital family at a constant tether length of 500 km. The legend indicates C values. The plus marker indicates the L1* equilibrium point leading Io for 500 km tether length

Example orbits from the family are given in Figure 5.20. A resemblance exists between this family and the unperturbed L1 and L2 Lyapunov orbits as all three families exhibit oval and kidney-like shapes. Because of the introduction of the Lorentz force, the new family is rotated nearly 90 deg from the unperturbed family, toward the leading edge of Io. Looking at individual

orbits, it can be seen that the smallest orbit shown is a narrow oval about the initiating equilibrium point. As Jacobi constant is decreased, the orbits grow in size and shift down toward Io, ending with an orbit that barely clears Io's mean radius.

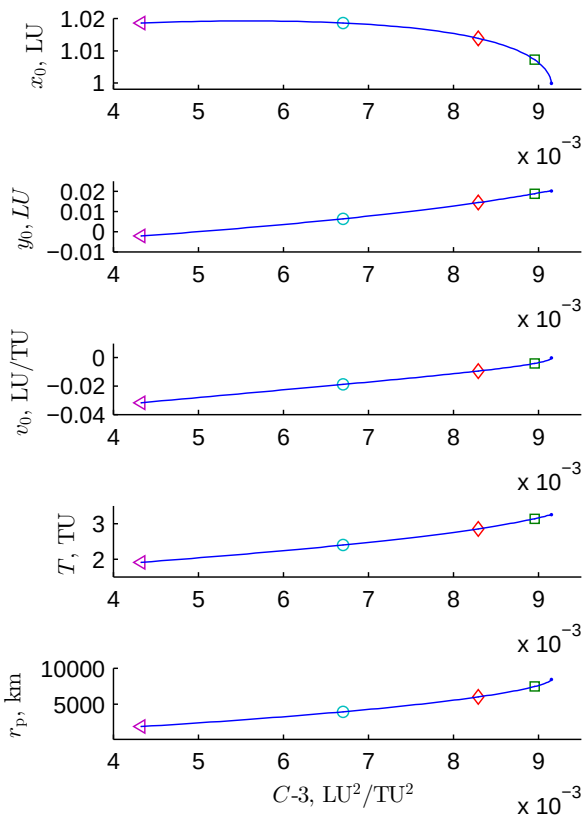

Figure 5.21: Characteristic curves for the L1 family at a tether length of 500 km. Markers correlate to orbits plotted in Figure 5.20

Figure 5.21 shows the characteristic curves for the orbit family, including markers for the orbits shown in Figure 5.20. All the curves show smooth, monotonic variation as the Jacobi constant is varied. In particular, larger or-

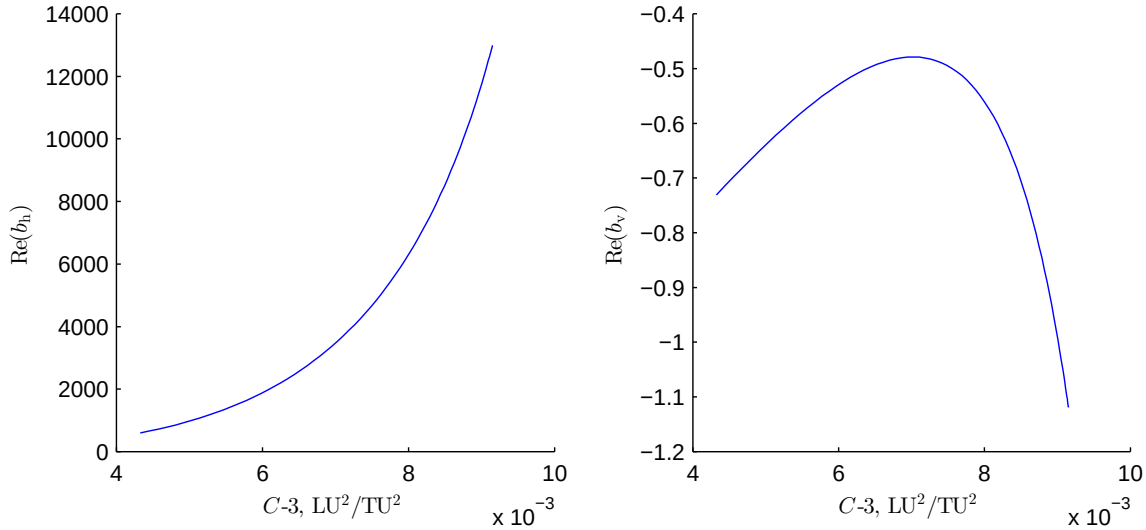

Figure 5.22: Horizontal and vertical stability indices for the L1 orbital family at 500 km tether length

bits lead to shorter periodic times and smaller close approaches. Figure 5.22 plots the stability indices for the family, where it is seen that all orbits in the family are unstable due to the high sensitivity to in-plane perturbations. However, all the orbits are within the stable region for the vertical index.

5.4 Conclusions

The introduction of electrodynamic tethers to the circular-restricted three-body problem leads to changes in both the equilibrium points and the periodic orbits of the model. The first main contribution of this work is the introduction of a conservative approximation to the tether force. By making a conservative force approximation, a modified Jacobi integral of motion is found and used to generate zero-velocity curves, which show that tether forces

can enable escape from the secondary. The conservative force also facilitates the generation of periodic orbit families in the three-body system, along with the associated stability analysis. While some error is introduced by the conservative approximation, the error is small in the expected regions of motion and is overshadowed by the multiple benefits of the integral of motion. Local equilibria near the secondary shift about the body as tether size is increased, with the perturbed L1 points ultimately descending to and impacting the surface while the L2 departs along the moon's orbit. A preliminary analysis of the gravitational torque shows that points close to the moon will require a counteracting control torque to maintain tether attitude.

The second contribution of this chapter is the generation of tether-perturbed Lyapunov families for both constant length and varying length. Several orbits with differing qualities are identified as stable, with verification from long-term numerical integration. Calculations on the tether attitude for one stable orbit quantify the expected peak control torque to fly the periodic orbit with a radially oriented tether. Again, the focus of this work is on the translational behavior of the tether, and so only a preliminary analysis of the attitude control is performed to quantify the expected range of the control torque. Attitude control for an actual flight may be prohibitively complex and merits further investigation.

A notably finding is that the tether-perturbed dynamics yield modified equilibrium points that provide opportunities for new mission designs. If there is interest in placing the spacecraft in an equilibrium point for constant

observation geometries of a moon, a tether provides mission designers with extra degrees of freedom for equilibrium locations. Assuming controllability in tether length, it would be possible to transfer across a range of equilibrium points for long-term constant observation. Selection criteria for these locations can include using the bodies as partial shielding from Jovian radiation. A more innovative concept is the use of a probe at the end of the tether to physically sample the moons while the Lorentz force holds the spacecraft in a steady location. Obviously, such a concept assumes highly precise control of the tether and may not be feasible in practice.

While the equilibrium points are generally unstable, an alternative to maintaining a highly constrained position is through the use of periodic orbits, some of which are stable for various ranges of tether length and energy levels. After generating multiple families of basic Lyapunov-like orbits from the unperturbed orbit families, it is found that stable orbits do exist for differing tether lengths and energy levels, including stable orbits in families that were originally only unstable. These new orbits exhibit dynamical behavior not seen in the unmodified families. In particular, the existence of multiple equilibrium points relatively close to each other results in new, slowly traversed loops leading Io. An additional simple orbit family found directly from the perturbed equilibrium points shows the potential for new and unexpected dynamical behavior. Investigations of broader classes of periodic orbits (via grid searches and bifurcations, extensions to three dimensions, etc.) will likely find more orbits of interest. From a mission design standpoint, these orbits can

be used as long-term parking orbits near a moon. Additionally, power can be generated over the course of the orbit without the need to maintain position as would be necessary at equilibrium points. Assuming the orbit is favorable for science data, such orbits are more propellant efficient to realize than typical low-altitude science orbits deep in the moon's gravity well.

Electrodynamic tethers are currently in a state of infancy, with only a few low-Earth-orbit proof-of-concept flights. The physical problem of safely and accurately controlling a tether tens of kilometers long is challenging and requires significant development in multiple fields of research. However, the addition of the Lorentz force leads to new and unique dynamics. With a few basic simplifications, the dynamics become relatively straightforward while retaining their core properties. The controllability of the Lorentz force as an essentially propellantless propulsion adds new variables to the design space, leading to potential new mission design applications not feasible otherwise.

Chapter 6

Conclusions

In this closing chapter, a summary overview of the developments made by this dissertation are presented. The key contributions and insights from the results are discussed in the broader context of low-energy mission design. Lastly, thoughts on avenues for further research building from this dissertation are explored.

6.1 Low-Energy Mission Design

The design of low-energy trajectories is a complex problem with a myriad of feasible approaches. Notably, the chaotic dynamics afford broad design space while simultaneously limiting analytical intuition on expected costs. As seen in Chapter 3, the derivation of a general analytical expression for the energetic cost enables rapid evaluation of any mission design option, whereas previous expressions were only accurate for low-altitude maneuvers. Further extension to the Hill's model allows the costs to be scaled to any three-body system of interest with minimal loss of accuracy. The equation provides an important benchmark for physical transfers by placing a lower bound on the cost. Earlier works were generally content to accept low-energy costs as a sig-

nificant improvement over two-body approaches, or optimized multiple feasible solutions to identify a best case. The knowledge of the energetic minimum enables a better approach to evaluate the capability of a technique to generate low-cost trajectories, as well as the means to determine whether an optimal solution might be a local or global minimum.

Finding good feasible transfer trajectories is a common challenge for low-energy missions. Intersections of invariant manifolds are frequently used as a starting point due to their effectively free cost, however they only exist for unstable orbits. In addition, locating any intersections (let alone efficient ones) is not guaranteed in three-dimensional space. Indeed, the author's initial attempts based on a global, time intensive, brute force method to search for all intersections of two trajectories typically resulted in extremely large maneuvers. Quickly generating good feasible transfers ultimately requires key assumptions on an ideal transfer to limit the design space and force the trajectories into favorable capture conditions. This insight lead to the development of grid searches to capture from L2 halo orbits in Chapter 3. For tight captures, targeting only the desired altitude and inclination eliminates the need to find intersections of a specific three-dimensional orbit, while allowing impulsive departures of the halo orbit provides a necessary additional degree of freedom in the search. The chaotic nature of loose captures effectively prevents straightforward orbital element targeting, and requires a different search method. Fortunately, simply matching energy levels is sufficient to generate some of the first known trajectories to loose capture orbits, and evaluating the

resultant orbits leads to a broad survey of interesting capture options. Comparing the energetic minimum to these trajectories shows that finding low-cost transfers is rare, even when utilizing searches based on an ideal trajectory.

The problem of generating good feasible transfers is revisited in Chapter 4, this time in the context of connecting resonant orbits to the optimized halo to capture transfers that are generated in Chapter 3. While another grid search approach is certainly feasible, the long timespan of resonant orbits creates a significantly larger search space than seen for the halo orbit departures. As previously discussed, efficiently targeting a specific halo orbit with only one constant of motion is an additional challenge. These difficulties are circumvented by instead generating a new periodic orbit that naturally transfers between resonant and halo phases. The search for the orbit proves to be straightforward, although it should be noted that targeting a specific resonance is left for future consideration. Continuation methods quickly generate one of the first known families of three-dimensional, resonant-halo orbits. The utility of this family is proven, as targeting techniques with simple heuristics are sufficient to generate good, feasible initial transfers to halo orbits. Importantly, there is no need to precisely match the timing of the halo capture maneuver with the halo departure, as the periodic orbit naturally handles phasing.

The resonant to halo transfer phase passes through a chaotic dynamic region, leading to extremely sensitive trajectories that are difficult to optimize. Several of the transfers constructed in this dissertation are among the most sensitive trajectories known to the author. While multi-shooting techniques

are already well-known for mitigating sensitivities, simply using single legs between each impulse are insufficient for the extreme transfers in this dissertation. The addition of minor segments to each leg proves to be critical for a robust optimization algorithm. By using the max norm of the STM to determine the locations of the minor segment nodes, an explicit limit is placed on the sensitivity that provides an intuitive tuning parameter compared to simply selecting some integer number of evenly spaced nodes. The selection criteria also reduces the size of the shooting algorithm by automatically creating fine resolutions of nodes only in chaotic regions, whereas stable trajectories are sparsely populated. A notable drawback from multi-shooting is that the cost is not truly a smooth, continuous function due to convergence tolerances in the shooting algorithm. The discontinuity is particularly problematic for extremely sensitive trajectories near the optimum. For these cases quadruple precision calculations prove to be crucial to refine solutions to a true analytical optimum.

Impulsive primer vector theory has historically been limited to initializing with two-impulse trajectories, with additional maneuvers determined iteratively such that all impulses are required for an optimal solution. However it is not uncommon to start with initial guess trajectories that have multiple maneuvers, as seen when patching trajectory phases together. Optimization drives unnecessary impulses towards zero, causing singularities in the derivatives. A common method to prevent this problem is to add a small, finite number to the impulse magnitude such that it is never exactly zero. In Chap-

ter 4, the derivation of new necessary conditions to remove maneuvers neatly eliminates the singularities without the need for artificial terms in the cost function. The equations are successfully used in this dissertation to remove patching maneuvers that are known to be initially necessary. For one transfer the conditions also determine that a miniscule impulse is in fact necessary for analytical optimality. Notably, this contribution also enables the use of primer vector theory on trajectories that start with any number of impulses, regardless of necessity. For example a mission designer could reasonably construct a transfer starting with miniscule maneuvers at every apse, then allow the extended primer vector theory to determine the optimal number of impulses.

Due to the improvements in both multi-shooting algorithms and primer vector theory (as well as several new predictor equations in Chapter 4 to improve optimizer convergence speed), this dissertation provides the first optimal, extreme sensitivity, three-dimensional transfers from resonant orbits to capture at Europa. A key observation from the results is that while the primer vector provides a useful visual tool for optimality, it does not generally indicate proximity to an optimum. It is also found that while the halo orbit serves as a convenient patching point, its use forces the transfer into a specific path that may not be globally optimal. Directly connecting the resonant orbit to capture may yield better results, assuming an efficient connection exists. Perhaps most importantly, the optimized resonant to loose capture transfers have costs that are an order of magnitude lower than a single tight capture maneuver. Combined with the existence of near-ballistic inter-moon transfers,

it is effectively demonstrated that a low-cost, single orbiter multi-moon tour is not only feasible, it can arguably be accomplished with less propellant than a tight capture orbiter dedicated to a single moon.

6.2 Electrodynamic Tethers

A natural (if advanced) extension to reducing the costs of planetary system exploration is the use of electrodynamic tethers, which have the potential to eliminate the need for propellant entirely. However, the addition of the velocity-dependent Lorentz force alters the dynamics such that they are no longer conservative. The dependence of the force direction on tether attitude introduces additional challenges, and ultimately necessitates some assumption on the tether direction to enable meaningful analytical analysis. While some periodic orbits might exist in the non-conservative tether dynamics (likely with active attitude control), initial attempts using standard techniques ultimately ended in failure. An approximation to the tether dynamics is derived in Chapter 5 that allows an integral of motion, enabling many of the powerful analytical techniques common to low-energy mission design. In particular, recall that the energetic minimum derived in Chapter 3 requires the Jacobi constant, as does the transfer grid search for loose captures.

As seen throughout this dissertation, periodic orbits frequently form the basis for low-energy mission designs. However, there are no prior works to find such orbits for electrodynamic tethers known to the author. Chapter 5 therefore provides the first survey of periodic orbits using electrodynamic

tethers. While the families are currently limited to the equivalent of Lyapunov orbits, several of them provide unique possibilities for mission designs, including trajectories that always lead or follow a planetary moon in its orbital path. Significant work remains to explore the new dynamics, however Chapter 5 shows that the conservative tether perturbed system can be investigated using essentially the same techniques as the unperturbed CRTBP. Presumably this similarity includes the methods developed to generate transfers in the previous chapters. Ideally, the inclusion of tether dynamics could be used to generate a fully ballistic capture trajectory, enabling true propellant-less exploration of the Jovian system.

6.3 Future Work

The work of this dissertation leads to numerous possibilities for further research, ranging from straightforward extensions of the current methods, to new investigations motivated by some of the interesting and unanticipated results. This section presents a non-exhaustive discussion of potential advancements that build upon this dissertation.

Perhaps the most compelling extension to the work is to construct a fully-optimized transfer between Ganymede and Europa. Critically, the assumption that the costs of the inter-moon transfer and the capture transfer remain relatively unchanged when patched together needs to be validated. In particular, the use of an inclined final resonant orbit in this dissertation could incur non-negligible cost when connected to the typically planar inter-moon

transfers. Ideally, constructing the end-to-end transfer would be a straightforward extension using the methods already developed in this dissertation, combined with the use of the patched CRTBP (similar to patched conics) to initially decouple the two moon phases. The Europa approach phase would be extended to the first resonant orbit and connected to the final state of a similar trajectory for Ganymede departure. With intelligent construction the two optimized phases are expected to patch together near-ballistically at negligible cost. A more complete approach would include optimizing the entire trajectory including this patching impulse, however this approach would likely be taken in an n-body model using accurate ephemerides. The long, multi-revolution transfers would be non-trivially perturbed by ephemeris dynamics, necessitating a methodology to maintain the trajectory when converting from the patched three-body model.

The transfers constructed in this dissertation use halo orbits to decouple the problem and patch together transfer phases. However, this method forces a specific trajectory solution that may end up stuck in a local minimum well. An investigation into alternative methods to connect orbits without halos, such as directly connecting manifold-like trajectories of the resonant and capture orbits, would enable different trajectory options that could lead to better initial guess transfers. Part of this work would include identifying efficient methods to target specific loose capture orbits, rather than treating them as an output of the transfer generation method. An interesting larger scale project would be to catalog and compare different construction methods according to their ease

of implementation, and likelihood of generating good initial guesses depending on the type of transfer.

A natural continuation of any trajectory design is to translate the problem to higher fidelity dynamics. Extension to higher order models will certainly perturb the trajectory, however the use of multi-shooting legs and segments is expected to sufficiently preserve the transfer such that the solution will quickly reconverge to a continuous trajectory. However, care must be taken as it is known that long trajectories with multiple flybys tend to not hold if the perturbations are sufficiently large [13]. Presumably the propulsive costs would remain relatively unchanged such that further optimization would not significantly improve the solution, although a significant increase would indicate the need for some refinement. A more comprehensive extension with optimization would include verification of the validity of impulsive primer vector theory in the increased complexity, nonautonamous models, along with derivation of the analytical derivatives if feasible.

While the resonant-halo periodic orbits provide a natural connection, the resulting transfers are extremely sensitive to small perturbations. These sensitivities warrant an investigation into the robustness of the transfer to the precision of practical impulsive maneuvers. This work would quantify the expected costs of trajectory correction maneuvers to account for stochastic perturbations to both the magnitude and direction of the impulses. Another useful result would be to identify patterns in the optimal timing of any correction maneuvers, likely by utilizing the established primer vector history

method for adding interior impulsive maneuvers. If the time between impulses is sufficiently short, the spacecraft would require on-board state estimation and correction maneuver evaluation, due to the long communication time between Earth and the Jovian system.

The loose captures found in this work are accepted as is, with only a cursory analysis on their stability over a typical science mission lifetime. Given the wide range of behaviors seen in these orbits, there is interest in further investigation into quantifying the utility of the captures for science observation. In the short term, it would be useful to evaluate the previously generated orbits in terms of scientific utility. For most science objectives, desirable orbit properties are global mapping coverage and repeat observations. A focused, larger scale project would attempt to identify if certain capture conditions lead to specific behaviors, providing a means to target a desired type of loose capture orbit.

The periodic orbits generated with an electrodynamic tether are limited to planar Lyapunov orbits about the L1 and L2 points. It is expected to be straightforward to expand the current results to other families using bifurcation methods. Initial emphasis would be on generating the equivalent of three-dimensional halo orbits, due to their utility for generating transfers as seen in this dissertation. However, the perturbed dynamics likely allow for a broad range of unique and unexpected periodic families, meriting a global search to find new orbits. Additionally, it would be interesting to see if the nonconservative tether dynamics allow periodic orbits. However, finding such

families is expected to require a significantly more complex investigation utilizing active control on the tether via some control law.

The ultimate goal of generating EDT periodic orbits is to provide the initial basis for constructing low-energy tether mission designs. It is expected that the typical method of finding intersections of unstable manifolds will remain useful for tether dynamics. However, a primary motivation of using the tether is to eliminate the need for impulses entirely. Finding near-ballistic intersections is expected to be particularly challenging, and would likely require active control of the tether to exactly target the full state at the intersection. This approach requires the development of a method to solve the tether-perturbed boundary value problem, including the derivation of feasible control laws on the tether attitude throughout the trajectory. While this leads to a fairly complex optimal control problem, finding purely ballistic trajectories would provide strong motivation to consider electrodynamic tethered spacecraft for Jovian system exploration.

Appendix

Appendix A

Optimization Algorithm

The optimization of highly-sensitive trajectories in Chapter 4 requires a specialized algorithm. A concise, high-level summary pseuodocode is provided here for clarity on the major steps used in the method. When available, specific calculations are followed by the relevant equation in parentheses for reference. Select subroutines that are modified to account for the sensitivity are also included in this appendix. Several steps are optional if the problem has been previously initialized, and are marked with * to note the associated data should be saved for reuse.

A.1 Main Program

1. Input vector of initial guess states and times, $\mathbf{k}_0$ (Eq. 4.10)
2. Set body system parameters, multi-shooting and optimizer convergence tolerances, and initial line search step size, $\Delta\alpha$
3. Create spline data for boundary orbits (See A.2)*
4. Run multi-shooting algorithm to evaluate Γ and all $\mathbf{\Phi}_i$ (Eq. 4.9)
   (a) Initialize times and nodes of minor segments if needed*

5. Evaluate primer vector history (Eq. 4.6 – 4.8)

6. Evaluate gradient (Eq. 4.11 – 4.15)

7. While optimality is not satisfied within tolerance: (Eq. 4.3 – 4.5)

   (a) Calculate search direction $\mathbf{s}$ using BFGS algorithm

   (b) Calculate predictor step direction for $\mathbf{v}_{i+}$ (Eq. 4.20 – 4.22)

   (c) Find α^* that minimizes $\Gamma(\mathbf{k} + \alpha\mathbf{s})$ via line search (See A.3)

   (d) If line search fails to find improvement ($\alpha^* = 0$): restart algorithm using quadruple precision for at least several iterations

   (e) If an impulse is near-zero: check for removal. If impulse node is removed: reinitialize algorithm at Step 4 (Eq. 4.26 – 4.27)

   (f) Update $\mathbf{k} = \mathbf{k} + \alpha^*\mathbf{s}$, $\Delta\alpha = 2\alpha^*$

   (g) Evaluate primer vector history and gradient

   (h) If norm of the gradient is zero within tolerance:

      i. If $||\mathbf{p}(t)|| > 1$: add new node to $\mathbf{k}$ at time of peak primer magnitude and return to step 7c with special search direction on that node only (Eq. 4.24)

8. Output $\mathbf{k}$ and Γ of optimal solution

A.2 Boundary Orbit Interpolation via Cubic Splines

The boundary value constraints on the initial and final states of the transfer are satisfied by explicitly setting the states to be within the corresponding orbit as a function of time. Piecewise polynomial splines interpolate the state to reduce calculation time and ensure that the same time results in the same state. Given two points in the trajectory, $\mathbf{x}_j$ and $\mathbf{x}_{j+1}$, the spline is defined as $\mathbf{x}(t) \approx \mathbf{p}_j(\tau) = \mathbf{a}_j\tau^3 + \mathbf{b}_j\tau^2 + \mathbf{c}_j\tau + \mathbf{d}_j$, where $\tau = [0, 1]$ is the normalized, shifted time for $t = [t_j, t_{j+1}]$ [99].

The points of the trajectory used in the spline are spaced using time steps scaled to the local acceleration, similar to a true anomaly Sundman transformation in the two-body problem [99]. The exact number and spacing of points in the spline is controlled by a tuning parameter, χ. While this variable requires some manual iteration to get the desired spacing, the scaling automatically creates finer resolutions when the trajectory is rapidly changing.

A.2.1 Spline Generation

1. Input initial state and time of boundary orbit

2. Define desired timespan of spline, $t = [t_-, t_+]$ and point spacing tuning parameter, χ

3. Initialize by integrating state to $\mathbf{x}_0$ at time $t_0 = t_-$, and set integer counter $j = 0$

4. While $t_j < t_+$:

(a) Evaluate step size $\Delta t = \chi / ||\ddot{\mathbf{r}}_j||$

(b) Evaluate $t_{j+1} = t_j + \Delta t$

(c) If $t_{j+1} > t_+$: set $t_{j+1} = t_+$, $\Delta t = t_{j+1} - t_j$

(d) Integrate $\mathbf{x}_j$ to $\mathbf{x}_{j+1}$

(e) $\mathbf{d}_j = \mathbf{x}_j$

(f) $\mathbf{c}_j = \dot{\mathbf{x}}_j \Delta t$

(g) $\mathbf{b}_j = -3\mathbf{x}_j - 2\dot{\mathbf{x}}_j \Delta t + 3\mathbf{x}_{j+1} - \dot{\mathbf{x}}_{j+1} \Delta t$

(h) $\mathbf{a}_j = 2\mathbf{x}_j + \dot{\mathbf{x}}_j \Delta t - 2\mathbf{x}_{j+1} + \dot{\mathbf{x}}_{j+1} \Delta t$

(i) Store coefficients and associated time t_j

(j) Update $j = j + 1$

5. Write out stored coefficients and times to data file

A.2.2 Spline Evaluation

1. Input time t, initialize counter $j = 0$

2. Read in spline coefficients and times

3. If t is outside bounds of spline: generate new spline data centered at t

4. While $t_{j+1} < t : j = j + 1$

5. Evaluate $\tau = (t - t_j) / (t_{j+1} - t_j)$

6. $\mathbf{x}(t) = \mathbf{a}_j \tau^3 + \mathbf{b}_j \tau^2 + \mathbf{c}_j \tau + \mathbf{d}_j$

A.3 Line Search

A line search method is used to find the values α^* and $\mathbf{k}^* = \mathbf{k} + \alpha^* \mathbf{s}$ that result in the minimum value $\Gamma^* = \Gamma(\mathbf{k}^*)$. The line search algorithm is based on the golden ratio ($\varphi = (1 + \sqrt{5})/2$) method [100]. However, the sensitivity of the trajectories frequently prevent the full step sizes commonly used to bracket the minimum. Several modifications are added to automatically scale the search step size $\Delta\alpha$ while maintaining convergence of the multi-shooting algorithm. The history of the three previous solutions are saved as $\mathbf{k}_j$ and Γ_j, along with the associated α_j. These histories are used to quadratically extrapolate/interpolate $\mathbf{k}$ (and segment node velocities $\mathbf{v}_{i+}$) as a function of α to improve convergence of the multi-shooting algorithm, as well as to identify when the minimum is bracketed.

1. Input initial $\mathbf{k}$, Γ, $\mathbf{s}$, $\Delta\alpha$, and minimum allowed α, ϵ_α
2. Initialize $\mathbf{k}_0 = \mathbf{k}$, $\Gamma_0 = \Gamma$, $\alpha_0 = 0$
3. Set $\alpha = \Delta\alpha$, update $\mathbf{k} = \mathbf{k}_0 + \alpha\mathbf{s}$, and all $\mathbf{v}_{i+} + \Delta\mathbf{v}_{i+}$ from BVP predictor (Eq. 4.20 – 4.22)
4. Evaluate $\Gamma(\mathbf{k})$ via multi-shooting algorithm
5. If multi-shooter does not converge:
   (a) If $\alpha > \epsilon_\alpha$: $\Delta\alpha = \Delta\alpha/3$ and go to Step 3
   (b) Else: exit search with $\alpha^* = 0$

6. If $\Gamma > \Gamma_0$:

   (a) Save histories: $\mathbf{k}_1 = \mathbf{k}$, $\Gamma_1 = \Gamma$, $\alpha_1 = \alpha$

   (b) While $\Gamma > \Gamma_0$:

      i. Set $\alpha = \varphi\alpha_1$

      ii. If $\alpha < \epsilon_\alpha$: exit search with $\alpha* = 0$

      iii. Interpolate $\mathbf{k}$ (and $\mathbf{v}_{i+}$): $\mathbf{k} = \varphi\mathbf{k}_1 + (1-\varphi)\mathbf{k}_0$

      iv. Evaluate $\Gamma(\mathbf{k})$ via multi-shooting algorithm

      v. Save histories: $\mathbf{k}_2 = \mathbf{k}_1$, $\Gamma_2 = \Gamma_1$, $\alpha_2 = \alpha_1$, $\mathbf{k}_1 = \mathbf{k}$, $\Gamma_1 = \Gamma$, $\alpha_1 = \alpha$

7. If $\Gamma < \Gamma_0$:

   (a) Save histories: $\mathbf{k}_2 = \mathbf{k}$, $\Gamma_2 = \Gamma$, $\alpha_2 = \alpha$, $\mathbf{k}_1 = \mathbf{k}_0$, $\Gamma_1 = \Gamma_0$, $\alpha_1 = \alpha_0$

   (b) While $\Gamma < \Gamma_1$:

      i. Set $\alpha = \alpha_2 + \Delta\alpha$

      ii. From histories, extrapolate $\mathbf{k}$ (and $\mathbf{v}_{i+}$) as function of α

      iii. Evaluate $\Gamma(\mathbf{k})$ via multi-shooting algorithm

      iv. If multi-shooter does not converge: $\Delta\alpha = \Delta\alpha/2$, restart loop

      v. Resize $\Delta\alpha$ based on number of multi-shoot iterations (i.e. decrease if convergence takes a long time, increase if converges immediately)

vi. Save histories: $\mathbf{k}_0 = \mathbf{k}_1$, $\alpha_0 = \alpha_1$, $\Gamma_0 = \Gamma_1$, $\mathbf{k}_1 = \mathbf{k}_2$, $\alpha_1 = \alpha_2$, $\Gamma_1 = \Gamma_2$, $\mathbf{k}_2 = \mathbf{k}$, $\alpha_2 = \alpha$, $\Gamma_2 = \Gamma$

8. With minimum bracketed between α_0 and α_2, find α^*, $\mathbf{k}^*$, and Γ^* using golden ratio method

9. Output α^*, $\mathbf{k}^*$ and Γ^*, as well as all $\mathbf{\Phi}_i$ of the minimum trajectory

Bibliography

[1] Europa Study Team, Europa Study 2012 Report: Europa Multiple Flybys Mission. NASA, May 1, 2012, JPL D-71990.

[2] JPL HORIZONS Solar System Data and Ephemeris Computation Service. Solar System Dynamics. NASA, Jet Propulsion Laboratory. Retrieved 10 August 2007.

[3] E. L. Allgower and K. Georg. *Introduction to Numerical Continuation Methods*. Philadelphia, PA: Society for Industrial and Applied Mathematics, 2003. ISBN: 0-89871-544-X (pbk.)

[4] R. L. Anderson. "Approaching Moons from Resonance via Invariant Manifolds". *Journal of Guidance, Control, and Dynamics* 38.6 (June 2015), pp. 1097–1109. DOI: 10.2514/1.G000286.

[5] R. L. Anderson, S. Campagnola, and G. Lantoine. "Broad Search for Unstable Resonant Orbits in the Planar Circular Restricted Three-Body Problem". *Celestial Mechanics and Dynamical Astronomy* 124 (Feb. 2016), pp. 429–450. DOI: 10.1007/s10569-015-9659-7.

[6] R. L. Anderson and M. W. Lo. "Flyby Design using Heteroclinic and Homoclinic Connections of Unstable Resonant Orbits". 21st AAS/AIAA Space Flight Mechanics Meeting, AAS 11-125. New Orleans, LA, Feb. 2011.

[7] H. Baoyin and C. R. McInnes. "Trajectories to and from the Lagrange Points and the Primary Body Surfaces". *Journal of Guidance, Control, and Dynamics* 29.4 (2006), pp. 998–1003. DOI: 10.2514/1.17757.

[8] T. Bayer et al. "Europa Clipper Mission: the Habitability of an Icy Moon". Aerospace Conference, IEEE. Big Sky, MT, Mar. 2015.

[9] K. A. Bokelmann and R. P. Russell. "Halo Orbit to Science Orbit Captures at Planetary Moons". *Acta Astronautica* 134 (May 2017), pp. 141–151. DOI: 10.1016/j.actaastro.2017.01.035.

[10] C. Bombardelli, E. C. Lorenzini, and J. R. Sanmartín. "Jupiter Power Generation with Electrodynamic Tethers at Constant Orbital Energy". *Journal of Propulsion and Power* 25.2 (2009), pp. 415–423. DOI: 10.2514/1.38764.

[11] C. Bombardelli and J. Peláez. "On the Stability of Artificial Equilibrium Points in the Circular Restricted Three-Body Problem". *Celestial Mechanics and Dynamical Astronomy* 109.1 (2011), pp. 13–26. DOI: 10.1007/s10569-010-9317-z.

[12] C. Bombardelli et al. "Io Exploration with Electrodynamic Tethers". AIAA/American Astronautical Society Astrodynamics Specialist Conference and Exhibit. Honolul, HI, Aug. 2008.

[13] N. Bradley and R.P. Russell. "A Continuation Method For Converting Trajectories From Patched Conics To Full Gravity Models". *The Journal of the Astronautical Sciences* 61.3 (Sept. 2014), pp. 227–254. DOI: 10.1007/s40295-014-0017-x.

[14] R. Broucke. "Stability of Periodic Orbits in the Elliptic, Restricted Three-Body Problem". *AIAA Journal* 7.6 (1969), pp. 1003–1009. DOI: 10.2514/3.5267.

[15] J.O. Burns et al. "A Lunar L2-far Side Exploration and Science Mission Concept with the Orion Multi-Purpose Crew Vehicle and a Teleoperated Lander/Rover". *Advances in Space Research* 52.2 (July 2013), pp. 306–320. DOI: 10.1016/j.asr.2012.11.016.

[16] J.O. Burns et al. "Science on the Lunar Surface Facilitated by Low Latency Telerobotics from a Lunar Orbital Platform - Gateway". *Acta Astronautica* (Apr. 2018), pp. –. DOI: 10.1016/j.actaastro.2018.04.031.

[17] J. Burt and B. Smith. "Deep Space Climate Observatory: The DSCOVR Mission". Aerospace Conference, IEEE. Big Sky, MT, Mar. 2012. DOI: 10.1109/AERO.2012.6187025.

[18] S. Campagnola and R. P. Russell. "Endgame Problem Part 1: V_∞-Leveraging Technique and the Leveraging Graph". *Journal of Guidance, Control, and Dynamics* 33 (Mar. 2010), pp. 463–475. DOI: 10.2514/1.44258.

[19] S. Campagnola and R. P. Russell. "Endgame Problem Part 2: Multibody Technique and the Tisserand-Poincaré Graph". *Journal of Guidance, Control, and Dynamics* 33.2 (2010), pp. 476–486. DOI: 10.2514/1.44290.

[20] S. Campagnola et al. "Tisserand-Leveraging Transfers". *Journal of Guidance, Control, and Dynamics* 37 (July 2014), pp. 1202–1210. DOI: 10.2514/1.62369.

[21] M. J. Chung et al. "Trans-Lunar Cruise Trajectory Design of GRAIL (Gravity Recovery and Interior Laboratory) Mission". AIAA 2010-8384. AAS/AIAA Astrodynamics Specialist Conference. Toronto, Ontario Canada, Aug. 2010. DOI: 10.2514/6.2010-8384.

[22] K. Clark et al. *Jupiter Europa Orbiter Mission Study 2008: Final Report*. Tech. rep. JPL Report D-48279, 2009.

[23] C. C. Conley. "Low Energy Transit Orbits in the Restricted Three-Body Problem". *SIAM Journal on Applied Mathematics* 16.4 (July 1968), pp. 732–746. DOI: 10.1137/0116060.

[24] Bruce Conway, ed. *Spacecraft Trajectory Optimization*. Cambridge, NY: Cambridge University Press, 2010.

[25] D. C. Davis and K. C. Howell. "Characterization of Trajectories Near the Smaller Primary in Restricted Problem for Applications". *Journal of Guidance, Control, and Dynamics* 35 (Jan. 2012), pp. 116–128. DOI: 10.2514/1.53871.

[26] K. E. Davis. "Locally Optimal Transfer Trajectories Between Libration Point Orbits Using Invariant Manifolds". PhD thesis. Department of Aerospace Engineering Sciences, The University of Colorado at Boulder, 2009.

[27] K. E. Davis et al. "Optimal Transfers between Unstable Periodic Orbits using Invariant Manifolds". *Celestial Mechanics and Dynamical Astronomy* 109 (Mar. 2011), pp. 241–264. DOI: 10.1007/s10569-010-9327-x.

[28] K. E. Davis et al. "The Use of Invariant Manifolds for Transfers between Unstable Periodic Orbits of Different Energies". *Celestial Mechanics and Dynamical Astronomy* 107.4 (2010), pp. 471–485. DOI: 10.1007/s10569-010-9285-3.

[29] N. Divine and H. B. Garrett. "Charged Particle Distributions in Jupiter's Magnetosphere". *Journal of Geophysical Research* 88.A9 (1983), pp. 6889–6903. DOI: 10.1029/JA088iA09p06889.

[30] E. Fabacher et al. "Multiple Sun-Earth Saddle Point Flybys for LISA Pathfinder". *Advances in Space Research* 52 (July 2013), pp. 105–116. DOI: 10.1016/j.asr.2013.02.005.

[31] E. Fantino and R. Castelli. "Efficient Design of Direct Low-Energy Transfers in Multi-Moon Systems". *Celestial Mechanics and Dynamical Astronomy* 127 (Apr. 2017), pp. 429–450. DOI: 10.1007/s10569-016-9733-9.

[32] S. B. Gabriel, R. M. Jones, and H. B. Garrett. "Space Tethers for science in the Space Station Era". *Proceedings of the Second International Conference, edited by Guerriero, L. and Bekey, I.* Societá Italiana di Fisica. Bologna, Italy, Oct. 1988, pp. 217–229.

[33] "Continuation Methods". *Implicit Curves and Surfaces: Mathematics, Data Structures and Algorithms*. Ed. by A. J. P. Gomes et al. London: Springer, 2009. Chap. 6, pp. 145–186. DOI: doi.org/10.1007/978-1-84882-406-5.

[34] P. R. Griesemer, C. Ocampo, and D. S. Cooley. "Optimal Ballistically Captured Earth–Moon Transfers". *Acta Astronautica* 76 (July 2006), pp. 1–12. DOI: 10.1016/j.actaastro.2012.01.001.

[35] P. Grover and S. Ross. "Designing Trajectories in a Planet-Moon Environment using the Controlled Keplerian Map". *Journal of Guidance, Control, and Dynamics* 32.2 (2009), pp. 437–444. DOI: 10.2514/1.38320.

[36] M. Hénon. "A Family of Periodic Solutions of the Planar Three-Body Problem, and Their Stability". *Celestial Mechanics* 13.3 (1976), pp. 267–285. DOI: 10.1007/BF01228647.

[37] M. Hénon. "Numerical Exploration of the Restricted Problem. VI. Hill's Case: Non-periodic orbits". *Astronomy and Astrophysics* 9 (Nov. 1970), pp. 24–36.

[38] M. Hénon. "Vertical Stability of Periodic Orbits in the Restricted Problem I: Equal Masses". *Astronomy and Astrophysics* 28 (1973), pp. 415–426.

[39] M. Hénon. "Vertical Stability of Periodic Orbits in the Restricted Problem II: Hill's Case". *Astronomy and Astrophysics* 30.2 (1974), pp. 317–321.

[40] W. N. Hess, T. J. Birmingham, and G. D. Mead. "Absorption of Trapped Particles by Jupiter's Moons". *Journal of Geophysical Research* 79.19 (1974), pp. 2877–2880. DOI: 10.1029/JA079i019p02877.

[41] L. A. Hiday. "Optimal Transfers between Libration Point in the Elliptic Restricted Three-Body Problem". PhD thesis. Purdue University, 1992.

[42] K. C. Howell. "Three-dimensional, periodic, 'halo' orbits". *Celestial Mechanics* 32 (Jan. 1984), pp. 53–71. DOI: 10.1007/BF01358403.

[43] D. J. Jezewski and H. L. Rozendaal. "An Efficient Method for Calculating Optimal Free-Space N-Impulse Trajectories". *AIAA Journal* 6.11 (1968), pp. 2160–2165. DOI: 10.2514/3.4949.

[44] P. G. Kazantzis and C. L. Goudas. "A Grid Search for Three-Dimensional Motions and Three New Types of Such Motions". *Astrophysics and Space Science* 32 (Jan. 1975), pp. 95–113. DOI: 10.1007/BF00646219.

[45] W. S. Koon et al. *Dynamical Systems, The Three-Body Problem and Space Mission Design*. Marsden Books. ISBN 978-0-615-24095-4, 2008.

[46] W. S. Koon et al. "Heteroclinic Connections between Periodic Orbits and Resonance Transitions in Celestial Mechanics". *Chaos* 10 (June 2000), pp. 427–469. DOI: 10.1063/1.166509.

[47] Jet Propulsion Laboratory. *Cassini Legacy: 1997 - 2017: Quick Facts*. Aug. 29, 2017. URL: https://saturn.jpl.nasa.gov/mission/grand-finale/cassini-quick-facts/ (visited on 05/14/2018).

[48] T. Lam and G. J. Whiffen. "Exploration of Distant Retrograde Orbits Around Europa". 15th American Astronautical Society/AIAA Space Flight Mechanics Meeting. Copper Mountain, CO, Jan. 2005.

[49] D. Landau. "Efficient Maneuver Placement for Automated Trajectory Design". *Journal of Guidance, Control, and Dynamics* (Apr. 2018). DOI: 10.2514/1.G003172.

[50] G. Lantione and R. P. Russell. "A Hybrid Differential Dynamic Programming Algorithm for Constrained Optimal Control Problems, Part 1: Theory". *Journal of Optimization Theory and Applications* 154 (Aug. 2012), pp. 382–417. DOI: 10.1007/s10957-012-0039-0.

[51] G. Lantione and R. P. Russell. "A Hybrid Differential Dynamic Programming Algorithm for Constrained Optimal Control Problems, Part 2: Application". *Journal of Optimization Theory and Applications* 154 (Aug. 2012), pp. 418–442. DOI: 10.1007/s10957-012-0038-1.

[52] G. Lantione et al. "MAGNETOUR: Surfing Planetary Systems on Electromagnetic and Multi-Body Gravity Fields". *Acta Astronautica* 138 (Sept. 2017), pp. 543–558. DOI: 10.1016/j.actaastro.2016.12.014.

[53] G. Lantoine and R. P. Russell. "Near Ballistic Halo-to-Halo Transfers Between Planetary Moons". *Journal of Astronautical Sciences* 58.3 (2011), pp. 335–363. DOI: 10.1007/BF03321174.

[54] G. Lantoine, R. P. Russell, and S. Campagnola. "Optimization of Low-energy Resonant Hopping Transfers between Planetary Moons". *Acta Astronautica* 68.7–8 (2011), pp. 1361–1378. DOI: 10.1016/j.actaastro.2010.09.021.

[55] M. Lara and R. P. Russell. "Computation of a Science Orbit at Europa". *Journal of Guidance, Control, and Dynamics* 30.1 (2007), pp. 259–263. DOI: 10.2514/1.22493.

[56] M. Lara and R. P. Russell. "Computiation of a Science Orbit about Europa". *Journal of Guidance, Control, and Dynamics* 30.1 (Jan. 2007), pp. 259–263. DOI: 10.2514/1.22493.

[57] M. Lara and R. P. Russell. "Concerning the Family g of the Restricted Three-Body Problem". IX Jornadas de Trabajo en Mecanica Celeste. Huesca, Spain, June 2006.

[58] M. Lara, R. Russell, and B. Villac. "Classification of Distant Stability Regions at Europa". *Journal of Guidance, Control, and Dynamics* 30.2 (2007), pp. 409–418. DOI: 10.2514/1.22372.

[59] M. Lara and R.P. Russell. "Classification of the Distant Stability Regions at Europa". *Journal of Guidance, Control, and Dynamics* 30.2 (2007), pp. 409–418. DOI: 10.2514/1.22372.

[60] D. F. Lawden. *Optimal Trajectories for Space Navigation.* London: Butterworths, 1963.

[61] P. M. Lion and M. Handelsman. "Primer Vector on Fixed-Time Impulsive Trajectories". *AIAA Journal* 6.1 (1968), pp. 127–132. DOI: 10.2514/3.4452.

[62] Z. F. Luo et al. "Constructing Ballistic Capture Orbits in the Real Solar System Model". *Celestial Mechanics and Dynamical Astronomy* 120.4 (2014), pp. 433–450. DOI: 10.1007/s10569-014-9580-5.

[63] V. V. Markellos. "Bifurcations of Planar to Three-Dimensional Periodic Orbits in the General Three-Body Problem". *Celestial Mechanics* 25 (Sept. 1981), pp. 3–31. DOI: 10.1007/BF01301803.

[64] J. R. R. A. Martins, P. Sturdza, and J. J. Alonso. "The Complex-Step Derivative Approximation". *ACM Transactions on Mathematical Software* 29.3 (2003), pp. 245–262. DOI: 10.1145/838250.838251.

[65] G. Mengali and A. A. Quarta. "Optimization of Biimpulsive Trajectories in the Earth-Moon Restricted Three-Body System". *Journal of Guidance, Control, and Dynamics* 28.2 (2005), pp. 209–216. DOI: 10.2514/1.7702.

[66] M. Michalodimitrakis. "On the Continuation of Periodic Orbits from the Planar to the Three-Dimensional General Three-Body Problem". *Celestial Mechanics* 19 (Apr. 1979), pp. 263–277. DOI: 10.1007/BF01230218.

[67] M. Nakamiya et al. "Analysis of Capture Trajectories into Periodic Orbits about Libration Points". *Journal of Guidance, Control, and Dynamics* 31.5 (2008), pp. 1344–1351. DOI: 10.2514/1.33796.

[68] R Nybakken. "The Juno Mission to Jupiter, a Pre-Launch Update". Aerospace Conference, IEEE. Big Sky, MT, Mar. 2011.

[69] D. Ottesen and R. P. Russell. "Space Trajectory Optimization using Embedded Boundary Value Problems". AAS 17-837. AAS/AIAA Astrodynamics Specialist Conference. Stevenson, WA, Aug. 2017.

[70] J. S. Parker and G. H. Born. "Modeling a Low-Energy Ballistic Lunar Transfer using Dynamical Systems Theory". *Journal of Spacecraft and Rockets* 45.6 (2008), pp. 1269–1281. DOI: 10.2514/1.35262.

[71] J. S. Parker, K. E. Davis, and G. H. Born. "Chaining Periodic Three-Body Orbits in the Earth-Moon System". *Acta Astronautica* 67 (Sept. 2010), pp. 623–638. DOI: 10.1016/j.actaastro.2010.04.003.

[72] M. E. Paskowitz and D. J. Scheeres. "Design of Science Orbits about Planetary Satellites: Application to Europa". *Journal of Guidance, Control, and Dynamics* 29.5 (2006), pp. 1147–1158. DOI: 10.2514/1.19464.

[73] J. Peláez and Y. N. Andrés. "Dynamic Stability of Electrodynamic Tethers in Inclined Elliptical Orbits". *Journal of Guidance, Control, and Dynamics* 28.4 (2005), pp. 611–622. DOI: 10.2514/1.6685.

[74] J. Peláez, C. Bombardelli, and D.J. Scheeres. "Dynamics of a Tethered Observatory at Jupiter". *Journal of Guidance, Control, and Dynamics* 35.1 (2012), pp. 195–207. DOI: 10.2514/1.53383.

[75] J. Peláez and M. Lara. "Dynamics of Fast-Rotating Tethered Satellites". *Monografías de la Real Academia de Ciencias Exactas, Físicas, Químicas y Naturales de Zaragoza* 32 (2009), pp. 75–83.

[76] J. Peláez and M. Lara. "Periodic Solutions in Electrodynamic Tethers on Inclined Orbits". *Journal of Guidance, Control, and Dynamics* 26.3 (2003), pp. 395–406. DOI: 10.2514/2.5077.

[77] Committee on the Planetary Science Decadal Survey. *Vision and Voyages for Planetary Science in the Decade 2013-2022*. Washington, D.C.: National Research Council of the National Academies, National Academy Press, 2011. DOI: 10.17226/13117.

[78] H. Poincaré. *The Three-body Problem and the Equations of Dynamics*. English. Trans. French by B. D. Popp. Springer, [1890] 2017. DOI: 10.1007/978-3-319-52899-1.

[79] John E. Prussing. "Primer Vector Theory and Applications". *Spacecraft Trajectory Optimization*. Ed. by Bruce A. Conway. Cambridge Aerospace Series. Cambridge University Press, 2010, pp. 16–36. DOI: 10.1017/CBO9780511778025.003.

[80] R. Restrepo and R. P. Russell. "A Database of Planar Axi-Symmetric Periodic Orbits for the Solar System". AAS 17-694. AAS/AIAA Astrodynamics Specialist Conference. Stevenson, WA, Aug. 2017.

[81] R. Restrepo and R. P. Russell. "Patched Periodic Orbits: A Systematic Strategy for Low Energy Transfer Design". AAS 17-695. AAS/AIAA Astrodynamics Specialist Conference. Stevenson, WA, Aug. 2017.

[82] I. A. Robin and V. V. Markellos. "Numerical Determination of Three-Dimensional Periodic Orbits Generated from Vertical Self-Resonant Orbits". *Celestial Mechanics* 21.4 (1980), pp. 395–434. DOI: 10.1007/BF01231276.

[83] W. J Robinson. "The Restricted Problem of Three Bodies with Rigid Dumb-Bell Satellite". *Celestial Mechanics* 8.2 (1973), pp. 323–330. DOI: 10.1007/BF01231434.

[84] S. D. Ross and D. J. Scheeres. "Multiple Gravity Assists, Capture, and Escape in the Restricted Three-Body Problem". *SIAM Journal on Applied Dynamical Systems* 6.3 (2007), pp. 576–596. DOI: 10.1137/060663374.

[85] R. P. Russell. "Global Search for Planar and Three-Dimensional Periodic Orbits near Europa". *The Journal of the Astronautical Sciences* 54.2 (2006), pp. 199–226. DOI: 10.1007/BF03256483.

[86] R. P. Russell and A. T. Brinckerhoff. "Circulating Eccentric Orbits around Planetary Moons". *Journal of Guidance, Control, and Dynamics* 32.2 (2009), pp. 423–435. DOI: 10.2514/1.38593.

[87] R. P. Russell and T. Lam. "Designing Ephemeris Capture Trajectories at Europa using Unstable Periodic Orbits". *Journal of Guidance, Control, and Dynamics* 30.2 (2007), pp. 482–491. DOI: 10.2514/1.22985.

[88] R. P. Russell and M. Lara. "Long-Lifetime Lunar Repeat Ground Track Orbits". *Journal of Guidance, Control, and Dynamics* 30.4 (2007), pp. 982–993. DOI: 10.2514/1.27104.

[89] R I. Samanta Roy, D E. Hastings, and E. Ahedo. "Systems Analysis of Electrodynamic Tethers". *Journal of Spacecraft and Rockets* 29.3 (1992), pp. 415–424. DOI: 10.2514/3.26366.

[90] J. R. Sanmartín and E. C. Lorenzini. "Exploration of Outer Planets Using Tethers for Power and Propulsion". *Journal of Propulsion and Power* 21.3 (2005), pp. 573–576. DOI: 10.2514/1.10772.

[91] J. R. Sanmartín, M. Martínez-Sánchez, and E. Ahedo. "Bare Wire Anodes for Electrodynamic Tethers". *Journal of Propulsion and Power* 9.3 (1993), pp. 353–360. DOI: 10.2514/3.23629.

[92] J. R. Sanmartín et al. "Efficiency of Electrodynamic Tether Thrusters". *Journal of Spacecraft and Rockets* 43.3 (2006), pp. 659–666. DOI: 10.2514/1.16174.

[93] J. R. Sanmartín et al. "Electrodynamic Tether at Jupiter-I: Capture Operations and Constraints". *IEEE Transactions on Plasma Science* 36.5 (2008), pp. 2450–2458. DOI: 10.1109/TPS.2008.2002580.

[94] J. R. Sanmartín et al. "Electrodynamic Tether at Jupiter-II: Fast Moon Tour After Capture". *IEEE Transactions on Plasma Science* 37.4 (2009), pp. 620–626. DOI: 10.1109/TPS.2009.2013955.

[95] K.P. Seidelmann. *Explanatory Supplement of the Astronomical Almanac*. Mill Valley, CA: University Science Books, 1992, pp. 708–711.

[96] T. H. Sweetser. "Estimate of the Global Minimum DV Needed for Earth-Moon Transfer". AAS/AIAA Spaceflight Mechanics Meeting, AAS 91-101. Houston, TX, Feb. 1991.

[97] V. Szebehely. *Theory of Orbits: The Restricted Problem of Three Bodies*. New York: Academic Press, 1967.

[98] S. G. Tragesser and H. San. "Orbital Maneuvering with Electrodynamic Tethers". *Journal of Guidance, Control, and Dynamics* 26.5 (2003), pp. 805–810. DOI: 10.2514/2.5115.

[99] David A. Vallado. *Fundamentals of Astrodynamics and Apllications*. Space Technology Library, 2007. ISBN: 978-1-881883-14-2.

[100] G. N. Vanderplaats. *Multidiscipline Design Optimization*. Colorado Springs, CO: Vanderplaats Research and Development, 2007.

[101] M. Vaquero and K. C. Howell. "Design of Transfer Trajectories between Resonant Orbits in the Earth-Moon Restricted Problem". *Acta Astronautica* 94 (Jan. 2014), pp. 302–317. DOI: 10.1016/j.actaastro.2013.05.006.

[102] B.F. Villac and D. J. Scheeres. "Escaping Trajectories in the Hill Three-Body Problem and Applications". *Journal of Guidance, Control, and Dynamics* 26.2 (2003), pp. 224–232. DOI: 10.2514/2.5062.

[103] K. E. Williams. "Overcoming Genesis Mission Design Challenges". *Acta Astronautica* 52 (Jan. 2003), pp. 281–287. DOI: 10.1016/S0094-5765(02)00167-4.

[104] D. Zanutto, D. Curreli, and E.C. Lorenzini. "Stability of Electrodynamic Tethers in a Three-Body System". *Journal of Guidance, Control, and Dynamics* 34.5 (2011), pp. 1441–1456. DOI: 10.2514/1.52755.

Vita

Kevin Bokelmann was born in Reno, Nevada. He obtained his Bachelors and Masters Degrees in Aerospace Engineering from the Georgia Institute of Technology. While there, he participated in several design competitions that led to his passion for interplanetary spacecraft missions. Kevin's research interests are on analytical and numerical techniques that enable advanced mission designs, with a focus on low-energy dynamics.

Permanent address: 7200 Easy Wind Dr, 1041
Austin, Texas 78752
kbokelmann@utexas.edu

This dissertation was typeset with LaTeX[†] by the author.

[†]LaTeX is a document preparation system developed by Leslie Lamport as a special version of Donald Knuth's TeX Program.